THESIS FOR THE DEGREE OF DOCTOR OF PHILOSOPHY

Powder bed fusion processing of Ni-base superalloys

Defect formation and its mitigation

HANS GRUBER

CHALMERS

Department of Industrial and Materials Science

CHALMERS UNIVERSITY OF TECHNOLOGY

Gothenburg, Sweden 2020

Powder bed fusion processing of Ni-base superalloys

Defect formation and its mitigation

Hans Gruber

ISBN 978-91-7905-357-4

Doctoral thesis at Chalmers University of Technology

New serial no: 4824

ISSN 0346-718X

Department of Industrial and Materials Science

Chalmers University of Technology

SE-412 96 Gothenburg

Sweden

Telephone + 46 (0)31-772 1000

URL: www.chalmers.se

Printed by Chalmers digitaltryck

Gothenburg, Sweden 2020

Powder bed fusion processing of Ni-base superalloys

Defect formation and its mitigation

Hans Gruber
Department of Industrial and Materials Science
Chalmers University of Technology

Abstract

Powder bed fusion of Ni- and Ni-Fe-base superalloys is actively considered a promising manufacturing technology for critical components for the aerospace and industrial gas turbine industries. Such components often operate under harsh conditions, and hence, high demands are placed on both process and feedstock material to meet the strict safety and long-term reliability requirements. The aim of this thesis is to provide knowledge regarding the formation of damage-relevant defects in Ni- and Ni-Fe-base superalloys fabricated by powder bed fusion as well as how they can be mitigated.

The first part of the thesis presents the connection between the surface oxidation of Alloy 718 powder for EBM, as a consequence of powder re-use, and the presence of oxide-related defects in the EBM fabricated material. The results indicate a clear connection between powder re-use and surface oxidation of the powder. Surface analysis of the progressively re-used powder by means of SEM, XPS and AES reveals significant growth of Al-rich oxide, which occurs via selective oxidation of Al due to the environment in the build chamber. Furthermore, the increased amount of oxide on the surface of the re-used powder results in an increased amount of oxide inclusions and lack of fusion defects in the EBM fabricated material. The morphology of the defects reveals that they originate from Al-rich oxide particulates on the surface of the re-used powder.

The second part of the thesis presents a study on the cracking of IN-738LC fabricated by means of LPBF. Implementation of custom designed powder grades with varying content of B and Zr indicates that both elements have a strong negative effect on the susceptibility to grain boundary microcracking of the alloy during LPBF. The XPS, AES and APT analyses show the enrichment of B and Zr at the cracked grain boundaries. Moreover, a significant portion of both elements are found to be connected to oxide. Hence, it is suggested that the increased microcracking susceptibility of IN-738LC is connected to the embrittlement of high-angle grain boundaries due to the formation of B- and Zr-containing oxide. In addition, post-LPBF hot isostatic pressing (HIP) is evaluated as a concept for microcrack healing. A HIP strategy that suppresses formation of macrocracks during the HIP treatment is developed by tailoring the temperature and pressure profiles during the heating stage. However, when applying the developed HIP strategy to the material grade with high levels of B and Zr, brittleness-inducing secondary phase particles at the grain boundaries appear after HIP at 1210°C, leading to a significant reduction of the impact toughness. Formation of the secondary phase is suppressed by lowering the HIP temperature to 1120°C. Results from microscopy and Charpy impact testing suggest that significant healing of the microcracks is accomplished when applying the developed HIP strategy.

Keywords: additive manufacturing, laser powder bed fusion, Ni-base superalloys, Alloy 718, IN-738LC, powder re-use, defect formation, non-metallic inclusions, cracking, hot isostatic pressing

Preface

This doctoral thesis is based on the work performed at the Department of Industrial and Materials Science at Chalmers University of Technology, Gothenburg, Sweden, between June 2016 and June 2020. The project has been conducted under the supervision of Professors Eduard Hryha and Lars Nyborg.

List of appended papers

I. **Effect of Powder Recycling in Electron Beam Melting on the Surface Chemistry of Alloy 718 Powder**
H. Gruber, M. Henriksson, E. Hryha, L. Nyborg
Metallurgical and Materials Transactions A, Vol. 50, 2019

II. **Effect of Powder Recycling on the Fracture Behavior of Electron Beam Melted Alloy 718**
H. Gruber, P. Karimi, E. Hryha, L. Nyborg
Powder Metallurgy Progress, Vol. 18, 2018

III. **Effect of Powder Recycling on Defect Formation in Electron Beam Melted Alloy 718**
H. Gruber, C. Luchian, E. Hryha, L. Nyborg
Metallurgical and Materials Transactions A, Vol. 51A, 2020

IV. **The Effect of Boron and Zirconium on the Microcracking Susceptibility of IN-738LC Derivatives in Laser Powder Bed Fusion**
H. Gruber, K. Lindgren, Y. Cao, M. Rashidi, E. Hryha, L. Nyborg
Submitted for journal publication

V. **Hot Isostatic Pressing of IN-738LC Fabricated by Laser Powder Bed Fusion**
H. Gruber, J. Xu, E. Hallberg, E. Hryha, L. Nyborg
In manuscript

Contributions to the appended papers

I. The author planned and executed the majority of the experimental work and the analysis of the results. The author assisted in the AES analysis. The author wrote the paper in cooperation with the co-authors.

II. The author planned and executed the majority of the experimental work and the analysis of the results. The author wrote the paper in cooperation with the co-authors.

III. The author planned and executed the majority of the experimental work and the analysis of the results. The author wrote the paper in cooperation with the co-authors.

IV. The author planned the study and performed the majority of the experimental work. The author assisted in EBSD and APT. The author wrote the paper in cooperation with the co-authors.

V. The author planned the study and performed the majority of the experimental work. The author assisted in EBSD. The author wrote the paper in cooperation with the co-authors.

Papers not appended in this thesis

A. **Surface Oxide State on Metal Powder and its Changes during Additive Manufacturing: an Overview**
E. Hryha, R. Shvab, H. Gruber, A. Leicht, L. Nyborg
Proceeding of Euro PM 2017 Congress & Exhibition, Milan, Italy 2017

B. **Influence of build layout and orientation on microstructural characteristics of electron beam melted Alloy 718**
P. Karimi, E. Sagedhi, D. Deng, H. Gruber, J. Andersson, P. Nylen
International Journal of Advanced Manufacturing Technology, Vol. 99, 2018

C. **Short-term creep behavior of an additive manufactured non-weldable Nickel-base superalloy evaluated by slow strain rate testing**
J. Xu, H. Gruber, D. Deng, R. L. Peng, J. Moverare
Acta Materialia, Vol. 179, 2019

D. **On the strengthening and embrittlement mechanism of an additively manufactured Nickel-base superalloy**
J. Xu, H. Gruber, R. Boyd, S. Jiang, R.L. Peng, J. Moverare
Materialia, Vol. 10, 2020

Contents

List of abbreviations

AES	Auger electron spectroscopy
BJ	Binder jetting
BSE	Backscatter electrons
CVN	Charpy V-notch
DDC	Ductility dip cracking
DED	Direct energy deposition
EBCHR	Electron beam cold hearth re-melting
EBM	Electron beam melting
EB-PBF	Electron beam powder bed fusion
EBSD	Electron backscatter diffraction
EDS	Energy dispersive X-ray spectroscopy
EIGA	Electrode inert gas atomization
ESR	Electroslag re-melting
GA	Gas atomization
HAZ	Heat affected zone
HIP	Hot isostatic pressing
ICP-OES	Induction coupled plasma optical emission spectroscopy
IGF	Inert gas fusion
LB-PBF	Laser based powder bed fusion
LOFD	Lack of fusion defect
LOM	Light optical microscopy
NBS	Nickel-base superalloy
NMI	Non-metallic inclusion
PA	Plasma atomization
PBF	Powder bed fusion
PMZ	Partially melted zone
pO_2	Oxygen partial pressure
PREP	Plasma rotating electrode process
PWHT	Post-weld heat treatment
SAGBO	Stress assisted grain boundary oxidation
SE	Secondary electrons
SEM	Scanning electron microscopy
TiN	Titanium nitride
VIGA	Vacuum induction gas atomization
VIM	Vacuum induction melting
VAR	Vacuum arc re-melting
XPS	X-ray photoelectron spectroscopy

1. Introduction

Additive manufacturing (AM) is a near-net-shape manufacturing method that offers many opportunities in product development and production. Commonly mentioned benefits include increased design freedom, reduced need for tooling, reduced assembly through part consolidation, reduced lead times, reduced number of manufacturing steps as well as reduced material consumption [1]. Within AM, powder bed fusion (PBF) is a process in which a laser or an electron beam is used to build parts by selectively melting thin layers in a metal powder bed, according to the geometry from a CAD-file. Especially, PBF is a promising method for limited production quantities of customized products using high-value materials that are difficult and inefficient to process using traditional manufacturing methods, as is often the case with Ni- and Ni-Fe-base superalloys for aerospace and power generation applications [1], [2].

As superalloys are often used in critical safety applications such as rotating parts in aerospace engines, careful control of raw material and process is essential to reach a low amount of damage-relevant defects. Non-metallic inclusions (NMIs) are brittle phases traditionally known to be a frequent cause of fatigue crack initiation, which in turn is the common cause for failure in rotating parts of aerospace engines [3], [4]. Cracks are another type of critical defect that are highly unwanted as they have a detrimental effect on mechanical properties, especially fatigue strength [5]. Currently both of these defects are present in many PBF fabricated superalloys, thus limiting their use for critical components.

The NMIs in Ni-base superalloys are mainly connected to Al-oxide and Ti-nitride inclusions formed in the process or introduced via the raw material. The latter is an important factor in PBF as the feedstock powder is sensitive to surface oxidation during fabrication and subsequent handling. Furthermore, powder oxidation may be exaggerated by re-use of the non-consumed powder in the powder bed, which is a requisite for reaching a high material efficiency in PBF. Powder oxidation is especially critical for electron beam melting (EBM) due to the elevated temperature in the build chamber. Knowledge regarding the effect of powder re-use and the extent to which it can be permitted before risking loss in part performance is therefore a key issue for EBM as a viable manufacturing process.

Microcracking of Ni-base superalloys (NBSs) during LPBF is strongly influenced by the concentration of trace elements such as S, P, Si, Mn and O as well as minor alloying elements such as B, Zr and C. In general, the reported scenario for the age-hardenable alloys such as IN-738LC is solidification cracking due to the formation of low melting point films during terminal solidification. Segregation of B and Zr to grain boundaries has in several cases been identified as the reason for the increased cracking susceptibility [6], [7]. However, many details regarding the mechanisms behind the cracking phenomena, including the nature and chemical state of the embrittling grain boundary compounds, are still not in place.

Previous research has suggested that microcracks in NBSs can be healed by applying a post-AM hot isostatic pressing (HIP) treatment[8], [9]. However, many details regarding the mechanical performance of the as-HIP material, as well as the HIP parameters required for obtaining a defect free material, are limited. Furthermore, macrocracks formed during HIP treatment of LPBF fabricated precipitation-strengthened NBSs are another obstacle that must be overcome to implement these alloys in the industry.

1.1 Research objectives

The overall aim of this thesis study is to deepen the knowledge regarding defects in PBF fabricated Ni-base superalloys and how their formation can be circumvented. This work is divided into two parts that each have specific aims and research questions.

Part 1: Powder re-use and its effect on defect formation in EBM fabricated Alloy 718

The particular focus of this part is the evaluation of the extent and mechanism of feedstock powder surface oxidation at the high temperature conditions in the EBM process chamber, as this may considerably change the performance of the powder during EBM processing as well as the process stability. Furthermore, a quantitative correlation between powder re-use, in terms of oxygen pick-up during EBM processing, and the quality of EBM processed samples is investigated. The latter is evaluated in terms of the amount and distribution of defects in samples built from virgin and re-used powder, respectively. Finally, the defect population in samples built from progressively re-used powder is carefully characterized to determine the formation mechanisms. From this topic, two main research questions (RQs) have been formulated:

- RQ 1: What is the effect of EBM processing on re-use of Alloy 718 powder?
- RQ 2: What is the effect of powder re-use on the amount and distribution of defects in EBM processed Alloy 718?

RQ 1 is addressed in paper **I**. RQ 2 is addressed in papers **II** and **III**.

Part 2: Cracking of LPBF fabricated IN-738LC

The first objective of this part is to investigate the effect of trace elements and minor alloying elements, with a special focus on boron and zirconium, on the microcracking susceptibility of IN-738LC processed by means of LPBF. Furthermore, the mechanism behind the cracking phenomena is investigated. The crack density is evaluated through LPBF specimens fabricated from custom designed powder grades with varying B and Zr levels. The surface sensitive analysis techniques X-ray photoelectron spectroscopy (XPS) and Auger electron spectroscopy (AES) are used to determine the extent of segregation on the microcrack surfaces by fracture surface analysis. The analyzed surfaces are produced and analyzed under high vacuum conditions to avoid contamination and oxidation during fracture in air.

The second objective of this part is to evaluate the potential of hot isostatic pressing (HIP) as a method for healing of microcracks in IN-738LC processed by means of LPBF. First, the aim is to investigate the reason for macrocracking during post-LPBF HIP treatment and how it can be avoided. Second, HIP is evaluated in terms of healing of microcracks in heavily cracked specimens alloyed with B and Zr. The formation of unwanted phases during HIP is also investigated. From this topic, three main research questions (RQs) have been formulated:

RQ 3: What is the effect of B and Zr on the microcracking susceptibility of LPBF processed IN-738LC?

- RQ 4: What is the cause of macrocracking during HIP treatment of LPBF processed IN-738LC, and how can it be mitigated?
- RQ 5: What is the effect of HIP treatment on microcrack healing of LPBF processed IN-738LC?

RQ 3 is addressed in paper **IV**. RQs 4 and 5 are addressed in paper **V**.

2. Superalloys

Superalloys are a group of materials developed for elevated temperature service wherein an adverse set of high mechanical, thermal and chemical loads may be encountered. Superalloys retain their properties to higher homologous temperatures than any other widely used commercial alloy system [4]. Therefore, they are the typical materials for use in high temperature engineering components, such as in the hot sections of aircraft jet engines and other gas turbines. However, due to their excellent properties superalloys are also applied in a wide range of other industrial application areas, such as rocket motors, power plants, automotive engines, hot work tools and dies as well as in the chemical industry. Based on their matrix and major alloying elements, superalloys are commonly divided into nickel-, cobalt-, iron-, and nickel-iron-base superalloys [4].

2.1 Ni- and Ni-Fe-base superalloys

Ni-base superalloys are divided into solid solution strengthened and precipitation strengthened alloys. The first are mainly used when strength is not of primary importance, but instead, other properties are required, such as corrosion resistance. Precipitation hardened superalloys, on the other hand, retain high strength at elevated temperatures owing to the precipitation of the strengthening phases γ' and γ".

Alloy 718 (also known as Inconel® 718 or IN718) is a well-known precipitation strengthened Ni-Fe-base superalloy. Since the development of the alloy in the late 1950s, it has been the workhorse for hot structural turbine engine components at working temperatures up to approximately 650°C [10], [11]. It is the material of choice for many gas turbine disc and rear frame applications, and has also earned success in the automotive, nuclear, oil and gas industries [4]. It remains the predominant superalloy of the world and constitutes one-third of the total weight of some aero engines [11].

The chemical composition of Alloy 718 is listed in Table 1. In contrast to many other superalloys, Alloy 718 has been developed to maximize strength at low to intermediate temperatures [4]. This is achieved by adding Nb, which promotes precipitation of the intermetallic phase γ" (Ni_3Nb). The γ" phase develops effective coherency strains relative to the matrix, from which Alloy 718 owes the main part of its high strength [4]. However, this also limits its strength to temperatures of around 650°C, above which a rapid loss in strength may occur due to particle coarsening [4]. This is also the lower temperature for formation of the δ phase, which is the thermodynamically stable form of γ". Furthermore, the sluggishness of the γ" precipitation gives Alloy 718 a high resistance to strain age cracking (SAC), which is a problem for many superalloys [4].

Table 1. Alloy 718 chemical composition in wt.% according to AMS 5662 [12]

Element	Ni	Cr	Fe	Nb	Mo	Ti	Al
Min	50.0	17.0	Bal.	4.75	2.8	0.65	0.2
Max	55.0	21.0	Bal.	5.5	3.3	1.15	0.8
Element	**C**	**Ta**	**Co**	**Mn**	**B**	**Si**	
Min	-	-	-	-	-	-	
Max	0.08	0.05	1.0	0.35	0.006	0.35	

Due to small additions of Al and Ti (0.5 and 1.0 wt.%, respectively), a smaller amount of the matrix-coherent γ' ($Ni_3(Al, Ti)$) also contributes to precipitation strengthening. However, the amount of γ' is only around 5 vol.%, which is much lower than that of many other superalloys [10]. As compared to many Ni-base superalloys, which contain a few percent of Al to improve their oxidation resistance by formation of an Al_2O_3 scale, the corrosion and oxidation resistance of Alloy

718 relies on the addition of Cr. The phases present in Alloy 718 and their roles are described in [10].

Inconel 738 (IN-738) is a γ' precipitation hardened Ni-base superalloy invented in the 1960s [4]. With an Al + Ti content of approximately 7 wt.%, IN-738 achieves a γ' volume fraction of about 40 vol.% after aging. This results in a high creep rupture strength up to around 980°C [13], [14]. Therefore, IN-738 is commonly used for hot gas path components such as blades and vanes in aero and industrial gas turbine engines [15], [16]. The relatively high Cr content (~16 wt.%) gives it a high hot corrosion resistance [14], [15]. Due to its high amount of γ', the temperature between the incipient melting temperature and the γ' solvus temperature is too narrow to allow for hot working, and thus, it is traditionally manufactured in the form of castings [17]. Due to the relatively high level of reactive elements (Al, Ti), it is traditionally melted and cast under vacuum conditions. In general, IN-738 is vacuum-melted and investment cast, but also occurs as ingot-castings using the VIM+EBCHR practice (see Section 4.1) [18]. Cast IN-738 is produced in a high carbon version (IN-738C, 0.17 wt.% C) and a low carbon version (IN-738LC, 0.11 wt.% C), which has improved castability. For the same reason, IN-738LC also has lower Zr content [14]. Like many γ' precipitation hardened Ni-base superalloys, IN-738 is not considered weldable in the normal sense [14]. The chemical composition of IN-738LC is provided in Table 2.

A small amount of carbon is often added in superalloys to form grain boundary carbides that strengthen the grain boundaries for improved creep life [4], [19]. In Alloy 718, the predominant carbide is the MC carbide NbC. IN-738 contains higher amounts of other MC carbides, such as TiC, TaC, but W and Mo may also be present in MC carbide [4]. In Ni- and Ni-Fe-base superalloys, MC typically decomposes during service and heat treatment, which releases C for the formation of lower carbides such as M_6C and $M_{23}C_6$, which are usually rich in Cr, Mo and W [20]. Carbon is also added for deoxidation purpose [4], as described in Section 4.

It has been shown that minute amounts, usually on ppm level, of B and Zr have significant positive effects on creep and rupture strength. However, the exact mechanisms behind this phenomenon remains unclear. Due to their odd size compared to the Ni matrix, it is known that both elements tend to segregate to the grain boundaries. In the case of B, it is believed that elemental B at the grain boundaries retards grain boundary cracking, owing to filling of vacancies, which reduces grain boundary diffusion. Cr-Mo-containing M_5B_3 and M_2B borides are commonly observed after heat treatment of NBSs [21], [22]. It is believed that borides in some systems act as supply for elemental B [4]. Moreover, it is believed that Zr has a gettering effect, i.e. acts as e.g. sulphide former, and thereby reduces elemental sulfur at the grain boundaries [4].

Careful control must also be taken to limit the amount of so-called tramp elements such as O, N, P, Pb, Se, Bi, Th, Te and Cu, which may have a detrimental influence on alloy performance. It is thus essential that their presence is carefully controlled in the melting process [4].

Table 2. Chemical composition of IN738LC in wt.%, according to Ref. [14]

Element	**Ni**	**Cr**	**Fe**	**Nb**	**Mo**	**Ti**	**Al**	**C**
Min	*50.0*	15.7	-	0.6	1.5	3.2	3.2	0.09
Max	*55.0*	16.3	0.05	1.1	2.0	3.7	3.7	0.13
Element	**Ta**	**Co**	**Mn**	**B**	**Si**	**W**	**Zr**	**S**
Min	1.5	3.0	-	0.007	-	2.4	0.03	-
Max	2.0	9.0	0.02	0.012	0.30	2.8	0.08	0.015

3. Metal additive manufacturing

Additive manufacturing (AM), also known as 3D-printing, is a family of manufacturing technologies in which parts are fabricated by adding material in thin successive 2D slices, derived from the geometry of a CAD model [23]. More specifically, AM involves several techniques for various materials and applications, among which the largest for fabrication of metal components are powder bed fusion (PBF), directed energy deposition (DED) and binder jetting (BJ).

PBF can be used for near-net-shape production of geometrically complex parts without the need for moulds and tooling. Thus, PBF may offer a reduction in cost, lead time and resources compared to many other metal working processes [7], [24], [25]. Its high degree of design freedom makes it well suited for smaller production series of high-value, complex shaped components where lightweight or integrated functionality is desired [26]. This has been identified by different industries, including the aerospace sector, especially for processing expensive materials with poor fabricability. This is generally the case for Ni-base and Ni-Fe-base superalloys [3], [7], [25], [27], [28], which due to their high strength at elevated temperatures, are known as some of the most "difficult-to-machine materials" [29]. In addition, high material costs and increasing demands on sustainable production routes further incentivize minimum machining and improved buy-to-fly ratio [30], [31].

3.1 Powder bed fusion

In PBF, parts are built by successively melting layers in a metal powder bed using a focused energy source [24], [32]. Divided into two subgroups, PBF includes laser based powder bed fusion (LB-PBF, commonly known as laser powder bed fusion, LPBF) and electron beam powder bed fusion (EB-PBF, commonly known as electron beam melting, EBM) [24], [33]. As implied by their names, one important difference between these two techniques is their use of thermal sources for melting the powder – a laser beam in LPBF and an electron beam in EBM. As described later, this implies further characteristic distinctions between them. The basic working principles of the EBM and LPBF processes are illustrated in Figures 1 and 2, respectively.

3.1.1 The PBF build cycle

In general, the PBF build cycle starts with distribution of powder in a thin layer across a build platform, onto which the parts are built. The powder layer is selectively melted according to the build geometry in the current layer. The build platform is then lowered by a distance equal to one layer thickness (typically between 20–50 μm for LPBF and 50–100 μm for EBM), and a new layer is spread and melted on top of the previous one. The adjacent layers are re-melted to avoid bonding defects between layers. This sequence is repeated until the parts have been successfully built. When the build cycle is completed, the non-consumed powder, which often constitutes a large portion of the powder bed, is evacuated from the chamber. The parts are separated from the start plate in a separate process.

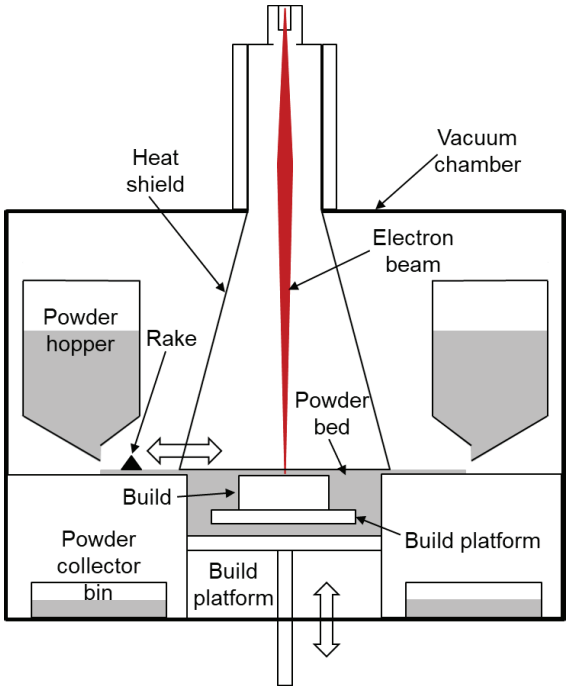

Figure 1. Schematic of the EBM machine interior; the gray areas constitute metal powder (redrawn from [34]*).*

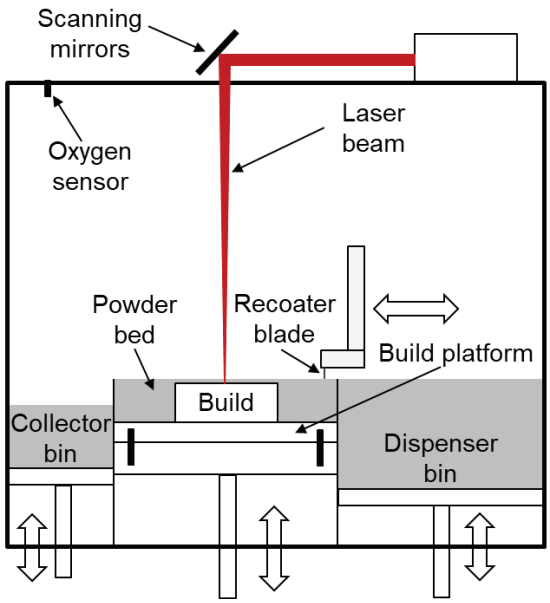

Figure 2. Schematic of the LPBF machine interior; gray areas constitute metal powder.

3.1.2 The scanning strategy

During melting, the beam moves according to a pre-defined scan pattern. Together with the process parameters (beam power, scan speed, layer thickness, etc.), the scan pattern forms the scanning strategy, which has a strong influence on several important features such as porosity, microstructure, surface roughness and residual stresses [24]. Consequently, different scan strategies have been identified as suitable for different technique and material combinations.

In EBM, the scan strategy has been chosen to improve the surface finish by lowering the part temperature when creating its surface. This occurs by applying one or several high energy spot melting passes, or multi-spots, at the edges, an area commonly referred to as the contour region,

before scanning the part core, as illustrated in Figure 3 [32]. Overlapping between the hatch and contour is done to improve the density at the interface. In LPBF, where the build temperature is lower, the scan pattern at the edges is usually continuous and is done after the hatch exposure [32]. The EBM core pattern, often referred to as the hatch pattern, is usually uni-directional or bi-directional, as depicted in Figure 3, and is rotated approximately 72 degrees between each layer [32]. The corresponding value in LPBF usually nears 67 degrees [35].

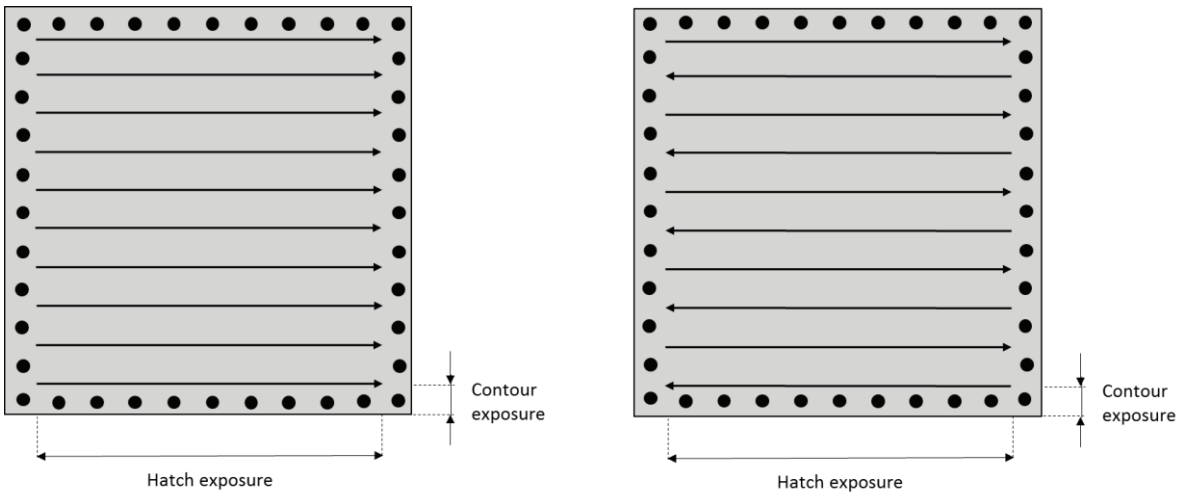

Figure 3. Uni-directional and bi-directional scanning patterns in EBM (redrawn from [34]*).*

3.1.3 Powder for PBF

The most common fabrication method for commercial pre-alloyed powders for PBF is gas atomization (GA), wherein the powder is atomized by a stream of inert gas. In inert gas atomization, the raw material is melted in an inert gas atmosphere. It is mostly used to produce less reactive materials such as Fe-base alloys [36], for which the atomizing gas can be nitrogen. For materials alloyed with reactive elements, such as Al and Ti in many Ni-base superalloys, reactions with oxygen and nitrogen during atomization are limited by melting the raw material in a controlled vacuum prior to atomization in argon, such as in the vacuum induction gas atomization (VIGA). According to specifications from powder producers [37], the oxygen and nitrogen levels in VIGA produced superalloy powder are commonly below 300 ppm. One major source of contamination, and the limitation for cleanliness and performance of this kind of powder, is interaction with the refractory system in contact with the melt during melting and molten metal transfer [4]. This has led to the development of the so-called ceramic-less powder atomizing techniques, in which the powder is produced by direct atomization of a wire or rod precursor material such that the molten metal does not come into contact with refractories [4]. Some examples of the ceramic-less atomization techniques are electrode induction gas atomization (EIGA), plasma rotating electrode process (PREP) as well as plasma atomization (PA, also referred to as advanced plasma atomization, APA™, developed by AP&C, Canada, which is a subsidiary of GE Additive). In PA, a high velocity argon plasma is used to atomize the wire precursor material at a very high temperature. The PA enables production of highly spherical powder (see Figure 4) with higher purity than the gas-atomized powder [38]. It should be noted, however, that the purity of EIGA and PA manufactured powder grades is largely dependent on the quality of the precursor material.

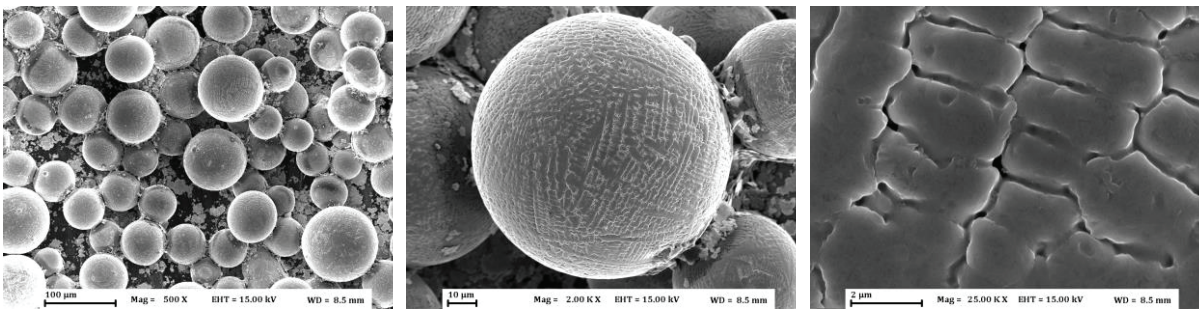

Figure 4. AP&C's Alloy 718 powder, produced by advanced plasma atomization and used in this work (author's experimental result).

3.1.4 The process environment

As previously mentioned, the difference in energy source implies characteristic differences between LPBF and EBM. Both processes occur in protective environments to prevent the hot metal surfaces from oxidation or other interactions with reactive atmospheric gases. The inert atmosphere in the LPBF is usually obtained by purging the process chamber with an inert gas, such as argon or nitrogen, to an oxygen concentration of approximately 1000 ppm or below [39], [40]. An oxygen sensor placed in the LPBF process chamber monitors the oxygen level during the process, as shown in Figure 2. The EBM process, on the other hand, requires a low vacuum to prevent collision of the electrons with gas molecules, which would deflect the beam and thereby lower its efficiency [32], [41]. The vacuum in the EBM chamber is created by first lowering the pressure inside the process chamber to below 1 x 10^{-8} bar. From an oxidation point of view, the vacuum should be as low as possible since the oxygen level stands in direct relation to the total pressure in the chamber. However, the system size and complexity, as well as the sublimation of volatile alloying elements, set practical limits to the achievable vacuum level. Sublimation is reduced by creating a partial pressure of inert gas during the process [4]. This is done by injecting a small amount of grade 5 purity helium (<2 ppm O_2), which raises the pressure in the build chamber to around 2 x 10^{-6} bar. From these values, an oxygen partial pressure in the order of 10^{-9} bar inside the build chamber can be estimated. The pressure, but not the oxygen level, is continuously measured and logged.

Another important characteristic of the EBM process is the fact that the powder bed is held at an elevated temperature throughout the build process. One reason for this is that the powder bed must have sufficient conductivity and mechanical stability to avoid so-called powder smoking. This originates in the electrical negative charge induced to the metal particles from the incoming electrons in the electron beam and can result in repulsion of the powder if the electrical forces become larger than those holding them in place [23]. Therefore, each powder layer is heated with the electron beam to create slight bonding between the metal particles [7], [10]. The elevated temperature also increases the stability of the melting process and varies between 600–1100°C depending on the processed material. For Alloy 718, a temperature of 975±25°C has been noted as optimal to reach a stable process [32], [34]. Below 950°C, increased powder smoking and spatter from the melt pool have been observed [32].

Powder smoking is further prevented by the presence of helium in the build chamber, as He tends to dissipate electrical charge build-up on the powder when ionized by the electron beam [32]. Moreover, the addition of He can be used for faster cooling of the build volume after completing the build.

The temperature in the EBM process chamber is maintained by using a rapidly scanned, diffuse electron beam. The temperature is initially established by heating the build platform and the adjacent powder before spreading the first powder layer. A thermocouple attached under the build platform registers when the temperature is reached. Thereafter, in each layer iteration, the area over the build platform is heated, before and after melting. The build platform temperature is logged throughout the process but cannot be used for feedback to control the temperature in the build volume or the energy input. Instead, a complex energy balance function that calculates the current and speed of the electron beam, based on the build geometry, is used to maintain the desired temperature [32].

Due to the high temperature in the build volume, parts fabricated by EBM typically have lower residual stresses compared to LPBF [24]. The temperature of the LPBF build platform can in some cases be heated to above 1000°C, but the preheating capabilities are normally lower [42]. In general, owing to the lower amount of residual stress, EBM is more suitable for processing of materials that are prone to cracking, including precipitation hardened superalloys and intermetallics such as TiAl [7], [41]. For the same reason, thick build platforms screwed to the machine feeding mechanism are required in LPBF to avoid plate warping due to the high residual stresses that occur in the parts, while the EBM build platform can be held in place simply by sintering the powder that surrounds it (see Figure 1). Furthermore, unlike LPBF, the sintered powder bed in EBM acts as a natural support for the parts, which can be stacked on top of each other in the build volume.

The risk of powder smoking in EBM can be further reduced by using coarser powder (~50–100 μm compared to ~10–60 μm for LPBF) and a less focused electron beam. This results in thicker layers and larger melt pools, respectively, which in turn increases productivity. However, this negatively affects the surface roughness and geometrical precision, which are generally better for LPBF [23], [24]. The productivity can be further increased as the electron beam is operated by electromagnetic lenses that allow for higher scan speeds compared to LPBF, in which mechanically moved mirrors are used for movement of the laser beam, as illustrated in Figure 2 [24], [32].

3.2 Powder re-use

Even though additive manufacturing has been subjected to extensive research during the last decade, there is still lacking knowledge in many aspects. One such area is the effect of the powder feedstock material on the process stability or quality of fabricated parts [43]. While several physical and chemical powder characteristics have been considered critical for maintaining a reliable process [44], [45], few indications regarding the importance of these characteristics have been established.

In addition, a relatively unexplored branch within additive manufacturing research is the possible degradation of the powder as a consequence of recycling, i.e. re-use of the non-consumed powder in subsequent build cycles. In the case of powder bed fusion, the non-consumed powder can constitute a large portion of the build volume after each completed build cycle. Powder re-use is therefore essential from a resource and economic perspective, especially since powder is generally more expensive than more commonly used material feedstock, such as plate, bar or tubing.

The non-consumed powder is re-circulated according to procedures specified by the machine producers. In LPBF, powder re-use involves sieving the powder that remains in the powder bed and the collector bin (see Figure 2) to remove any agglomerates that appear after the process. In the EBM process, due to powder sintering, the non-consumed powder in the powder bed, especially in the volume above and beneath the build platform, is in the shape of a cake of sintered powder, as depicted in Figure 5. Thus, in addition to the procedure in LPBF, the separation of

sintered powder particles occurs by grit blasting. As the temperature in the hoppers is lower than in the build chamber, this powder is less affected and can be sieved without grit blasting. To compensate for the powder consumed in the previous cycle, the re-used powder is commonly mixed with an amount of fresh powder before it is returned to the powder hoppers.

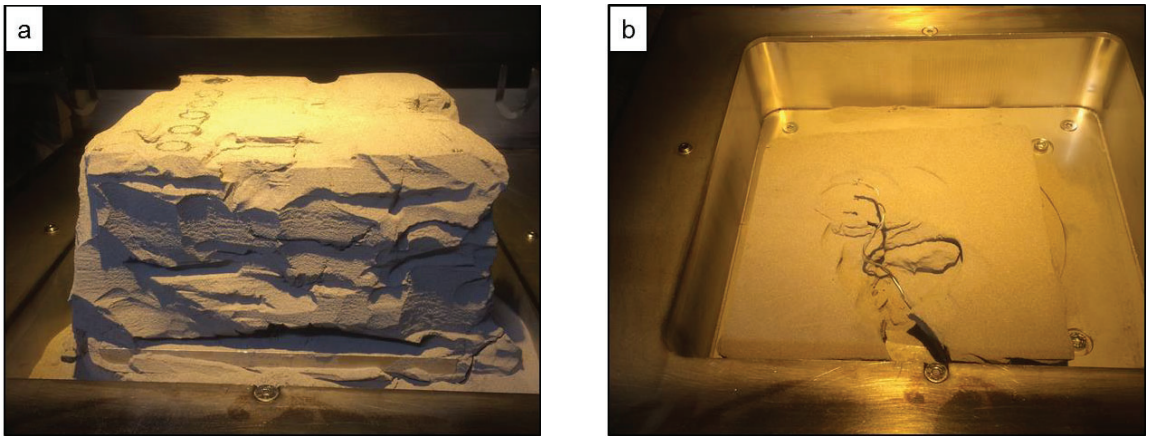

Figure 5. Cake of sintered Alloy 718 powder (a) above and (b) below the build platform in an Arcam A2X EBM machine.

Powder re-use in AM, in general, is known to influence physical and chemical powder properties [24]. Regarding physical properties, powder size, shape and surface morphology, for example, are known to change during re-use. However, in terms of resulting changes in part performance, no clear correlations have been established [24]. For powder chemistry, increasing powder oxygen levels as a consequence of powder re-use have been noted for metal additive manufacturing in general [46], [47], [48], [49], [50], [51]. Furthermore, the high specific surface area of the AM powder makes it susceptible to surface reactions such as oxidation [52]. It can be expected that the oxide on the powder surfaces may lead to reduced bonding between adjacent layers during melting, which may result in increased porosity and reduced mechanical performance [46], [53]. Hence, powder oxidation has been suggested to be the limiting factor for powder re-use [47] and will therefore be treated in detail in the following section. Oxidation, however, is a complex process, especially for highly alloyed superalloys. Thus, some general aspects of oxidation are presented below, before considering powder oxidation in Section 3.2.2.

3.2.1 High temperature oxidation

The thermodynamic equilibrium conditions for a given metallic element and its oxide are defined by oxygen partial pressure (pO_2) and temperature. Figure 6 illustrates this relationship for the oxides that may occur in Alloy 718. At conditions above each curve, it is thermodynamically favorable for the element to exist in oxide state, while at conditions below the curve, it is more likely to be in metallic state. As indicated in the figure, high temperature or low oxygen levels are required to prevent the metal from oxidizing. Although the data in Figure 6 are based on the oxidation of pure metals, it is still applicable for assessing the relative stability of oxides in an alloying system on a metal/gas interface. The dotted lines in Figure 6 represent the estimated conditions in the EBM process chamber discussed in Section 3.2.2.

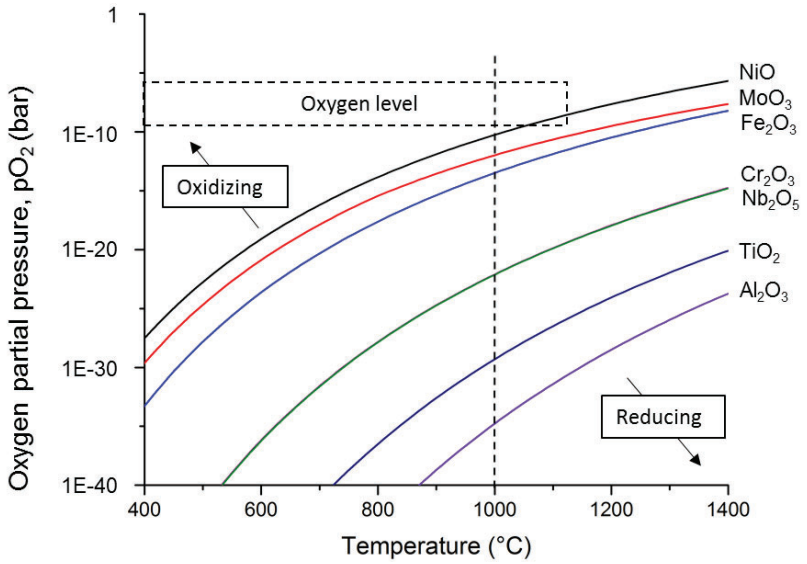

Figure 6. Metal and metal oxide equilibria diagram plotted using data from the software HSC Chemistry version 8.0; note the overlap of Cr_2O_3 and Nb_2O_5 in the indicated temperature range; the dotted lines indicate the estimated conditions in the EBM process chamber.

As Figure 6 reveals, there is a large difference in thermodynamic stability between the oxides. While nickel oxide is relatively unstable, others, such as alumina and Ti-oxide, require high temperatures and low oxygen levels for reduction. From a thermodynamic point of view, due to their high affinity for oxygen, elements like Al and Ti are selectively oxidized compared to elements that form less stable oxides [4], [54].

Furthermore, the extent of oxidation and the type of oxides found in the system depend on the kinetics, i.e. the mobility of elements through solid state diffusion. Even though aluminum forms the most stable oxide, its low bulk concentration in Alloy 718 (~0.5 wt. %) limits the amount that can react with oxygen at the surface. Instead, the vast amount of the bulk elements Ni, Cr and Fe render them as kinetically favorable oxide formers, among which Cr is the strongest oxide former, as shown in Figure 6. Therefore, a more or less continuous chromia scale is expected for Alloy 718 at the relatively low application temperature at which it is used [34], [55].

However, as indicated above, the many alloying elements in superalloys make their oxidation behavior complex, and other oxide types such as multi-layered Ni-, Fe-rich oxides [56], [57] and spinel oxides are sometimes observed in conjunction with the chromia-scale [55], [58]. With increasing diffusion rates at higher temperatures, external and internal oxidation of minor reactive elements, such as Al and Ti, may occur [58], [59].

3.2.2 Powder oxidation

Powder, in comparison to bulky materials, is more prone to oxidation due to its high specific surface area, which makes reactions with the atmosphere more effective. In this case, the difference in oxygen potential between the surface and the bulk of the powder creates a strong driving force for mass transport of elements with high oxygen affinity toward the powder surface. Furthermore, its small dimensions shortens the maximum diffusion distance, which equals part of the powder radius, thus further speeding up reactions at elevated temperatures [52].

As the hot metal is exposed to trace amounts of oxygen during atomization, some amount of oxide on the powder surface is expected already in the as-atomized state [60]. Figure 7 provides an example of two forms of surface oxide on the plasma atomized Alloy 718 powder used in this study. The oxide depicted in Figure 7 (a) consists of a bulk element oxide layer, which typically forms at lower temperatures during handling after atomization. The limited diffusion at these temperatures typically results in thin homogeneous surface layers. It is important to note that the oxide layers formed at room temperature is generally representing the surface alloy composition and will therefore be based on the major alloying element/s, i.e. nickel oxide in case of Ni-base superalloys [61]. Small amounts of strong oxide formers, such as Al and Ti, often result in heterogeneously distributed stable oxides, as shown in Figure 7 (b), which may form at higher temperatures during the atomization process [62], [63].

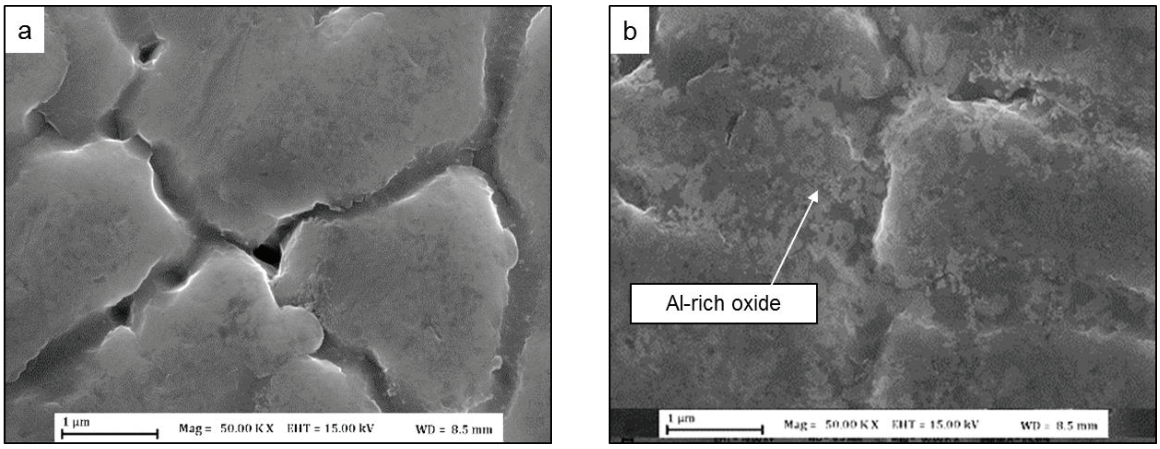

Figure 7. Oxide products on virgin Alloy 718 powder produced by plasma atomization (author's experimental result).

Typically, gas-atomized powder is exposed to air at room temperature for a short time during powder sieving and packing after atomization, resulting in formation of thin oxide layers, even if the surface was previously free from oxide. This applies for powder handling in general, including sieving and grit blasting for EBM in between the build cycles as well as during storage, when the powder is exposed to ambient air. Formation of hydroxides or uptake of chemisorbed and physiosorbed water may occur as well [64]. Passivation of the powder can also occur as a part of the manufacturing process to create a thin, homogeneous oxide layer that makes it more resistant to handling in open air [65].

Powder oxidation in LPBF

In LPBF, the main part of the powder bed is too cold for significant oxidation to occur. Hence, oxidation of the non-consumed powder in LPBF is limited to the volume close to that at which melting occurs (i.e. close to the fabricated parts) and to the so-called process emissions, including spatter, entrained powder and condensate, which are emitted due to interaction between the powder and the laser beam [66]. Among these emissions, the small sized condensate shows the highest extent of oxidation [65]. For example, Figure 8 illustrates differently affected Hastelloy X metal particles sampled at various positions in the process chamber shown in Figure 8 (a).

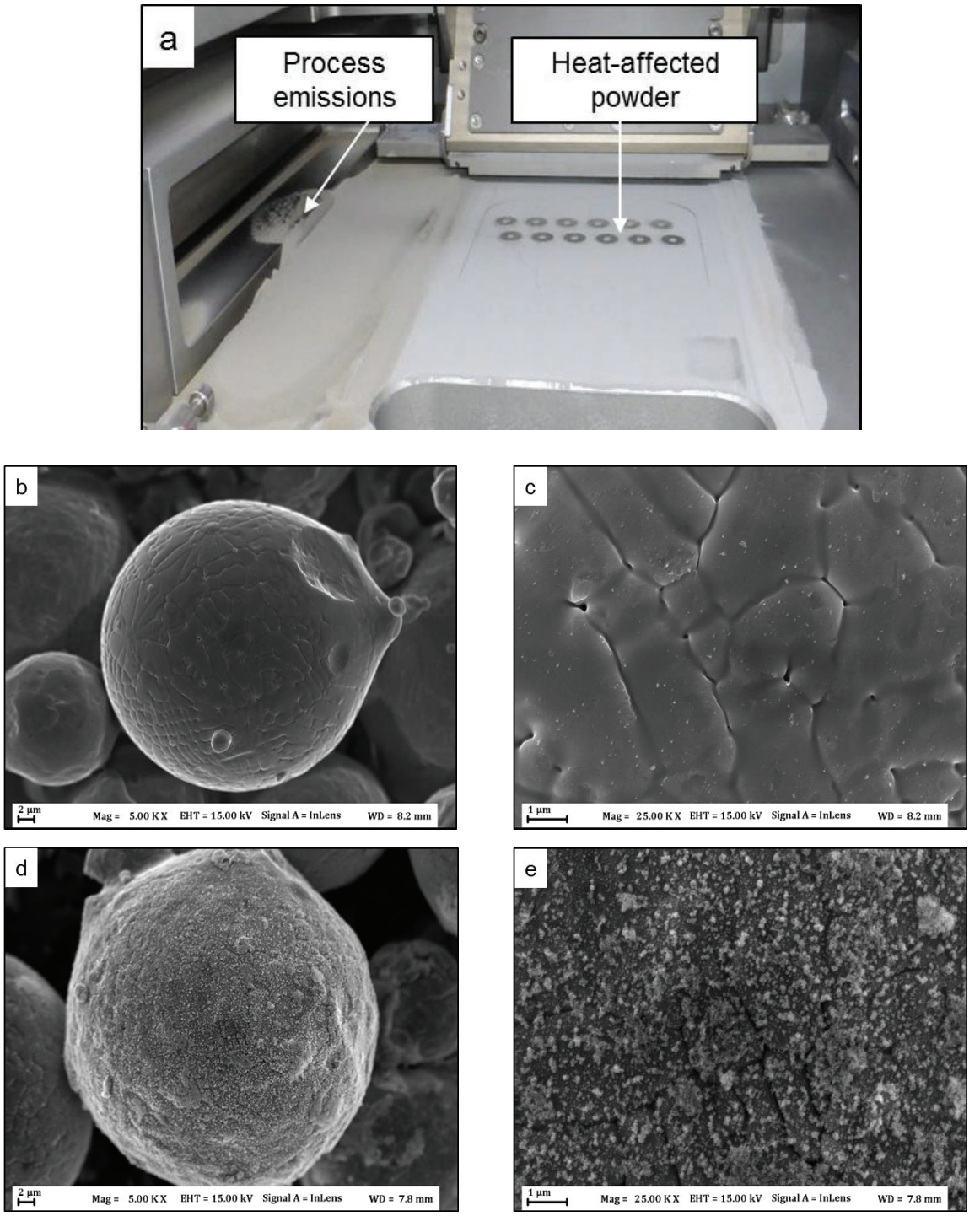

Figure 8. (a) LPBF process chamber with process emissions at the extraction nozzle (left side) and heat-affected powder in between the fabricated parts; (b, c) heat-affected particle sampled in between the parts in (a); (d, e) larger particle sampled close to the extraction nozzle (author's experimental result).

As Figure 8 (a) indicates, process emissions in LPBF follow the flow of the inert gas toward the extraction nozzle and partly leave the chamber this way. However, the emissions that do not reach the extraction nozzle will end up in the powder bed, which will over time increase its overall oxygen level [65].

Figure 8 (b, c) shows metal particles sampled from the volume close to the build parts, on which small oxide particulates have formed as a result of the increased temperature close to the molten

metal. Figure 8 (d, e) presents an emitted Hastelloy X particle exhibiting significant oxidation (Cr-oxide) sampled from the extraction nozzle.

As mentioned above, significantly increased oxygen levels have in some cases been reported for re-used LPBF powder. Resulting effects on porosity and ductility have also been noted but are usually reported to be limited [47], [67].

Powder oxidation in EBM

For EBM, increased oxygen levels have also been measured for the re-used powder [43]. Although the resulting effect on the part performance has not been studied in detail, it is often stated that the excess powder can sustain a large number of cycles without any appreciable influence on its chemical properties [68] and that re-use of Alloy 718 powder during EBM processing is solely limited by the physical powder characteristics such as flowability [43].

Given that the EBM process occurs under vacuum conditions, it is often marketed as a suitable alternative for processing materials with high oxygen affinity [41]. Indeed, the oxygen level in the EBM build chamber is several orders of magnitude lower than in LPBF and, hence, from this perspective, oxidation of the feedstock powder material should be lower.

However, for powder re-use, the extent of powder oxidation in EBM differs from LPBF as the entire powder bed is held at a high temperature (~1000°C). This is critical from the perspective of powder oxidation as the temperature is high enough for substantial diffusion to occur, while at the same time, it is too low for efficient reduction of most oxides at practical pO_2 levels [52]. This is illustrated in the metal/metal oxide equilibria diagram in Figure 6, which visualizes the estimated conditions in the EBM process chamber. It can be seen that all of the potential oxides apart from NiO and Fe_2O_3 are highly stable at these conditions. Hence, the presence of one or several of these oxides is likely at these conditions [69].

Powder bed fusion is associated with long process times, wherein one single cycle can last several days. As the build volume often contains large amounts of non-consumed powder, it is likely that a large portion of the powder may experience several re-use cycles. Therefore, it can be assumed that the accumulated exposure time at high temperature is sufficient for substantial oxidation to take place. The time and temperature required for a certain increase in oxygen level can be estimated using diffusion calculations.

Furthermore, prolonged high temperature exposure may result in the re-distribution of oxygen between oxides with different stability when the conditions are reducing for less stable compounds and oxidizing with respect to more stable ones [54]. Thus, oxygen existing as bulk oxide/hydroxide formed during powder atomization or powder handling (applies to virgin as well as re-used powder in between build cycles) may be released during the heating and melting of the powder in the process chamber. Consequently, as indicated in Figure 6, the actual oxygen partial pressure in the vicinity of the powder surface can be higher than the theoretical value and can locally rise to values in the order of 10^{-7} bar [34]. It should be noted, however, that these values are only valid assuming the system is air-tight, as leakage of air into the chamber may dilute the He-containing atmosphere and thereby increase the oxygen concentration without necessarily changing the pressure.

In any case, instead of being evacuated from the process chamber, the released oxygen may act as another source (in addition to the residual air in the vacuum atmosphere) that is consumed by strong oxide formers such as Al, present at the powder surface, for which these conditions are strongly oxidizing [54]. In such a case, transformation from less stable to more stable oxides results

in an initial distribution of co-existing bulk element oxides and more stable oxides. Since the stable oxides will also persist at high temperatures or low oxygen partial pressures, the amount of stable oxide on the powder surface will increase over the re-use cycles. This means that the chemistry and thereby the quality of the powder may be considerably changed. This situation is illustrated for Alloy 718 powder in Figure 9, wherein the powder surface coverage by stable Al-rich oxide particulates increases with progressive re-use. With reference to the virgin powder in Figure 4, it can be observed from Figure 9 (a-c) that oxidation starts already during the first build cycle, after which it progresses with increasing powder re-use, as shown in Figure 9 (d-i). Formation and growth of oxides during powder re-use is associated with an increase in oxygen level in the re-used powder, as depicted in Figure 27 in Section 6. Similar oxygen levels in re-used powder have been reported in earlier studies [43].

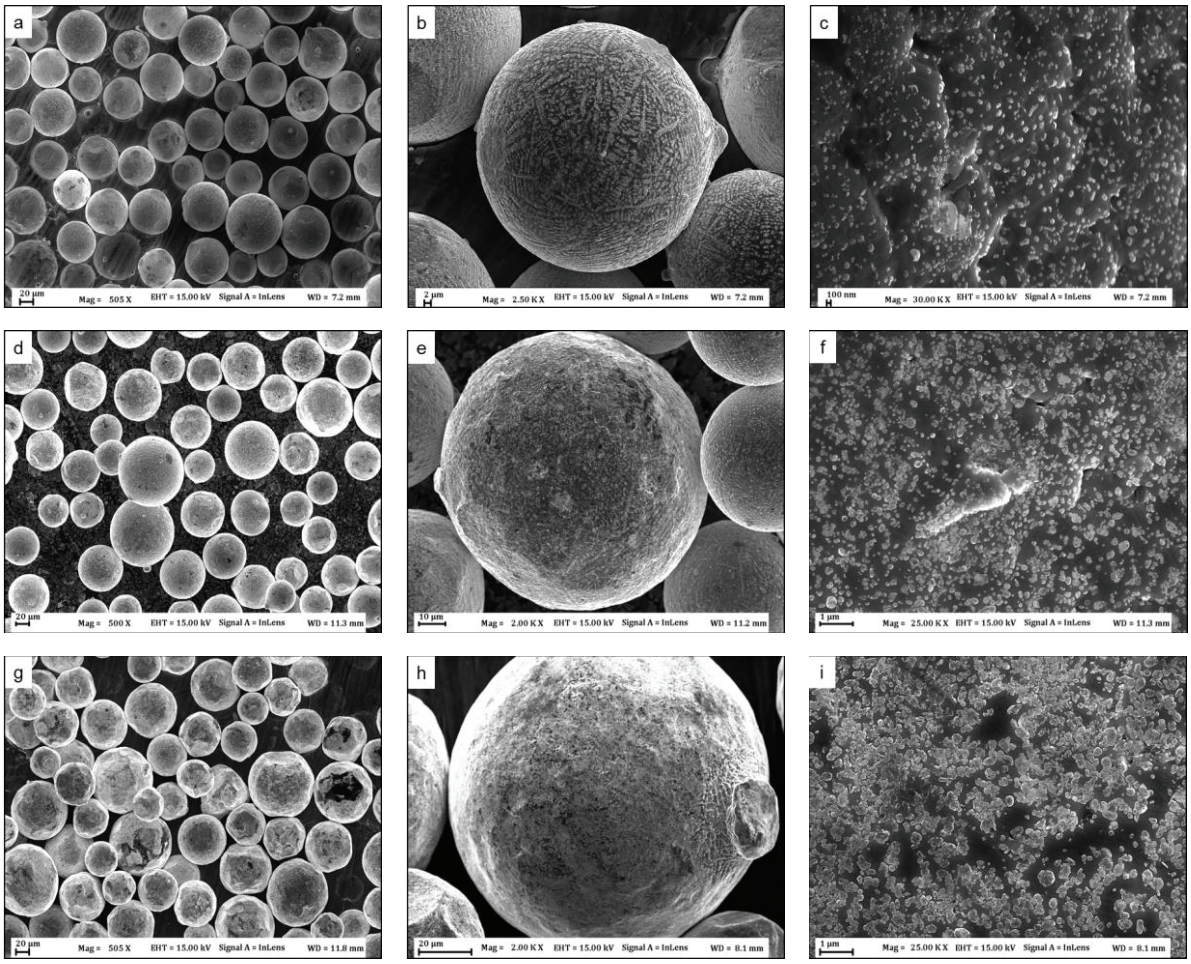

Figure 9. Progressively re-used Alloy 718 EBM powder sampled from the cake of sintered powder after (a-c) 1 cycle; (d-f) 5 cycles; (g-i) 30 cycles [70].

Furthermore, as shown in Figure 10, due to the long-term exposure at elevated temperatures in the EBM process chamber, the powder microstructure changes from a dendritic solidification structure in the virgin powder, as in Figure 10 (a), to a microcrystalline structure in the re-used condition, as in Figure 10 (b). In addition, as evidenced by the EDS maps in Figure 10 (c), the needle-shaped δ-phase (Ni_3Nb) forms as a consequence of the enhanced diffusion at the elevated temperature and is therefore often present in the re-used powder.

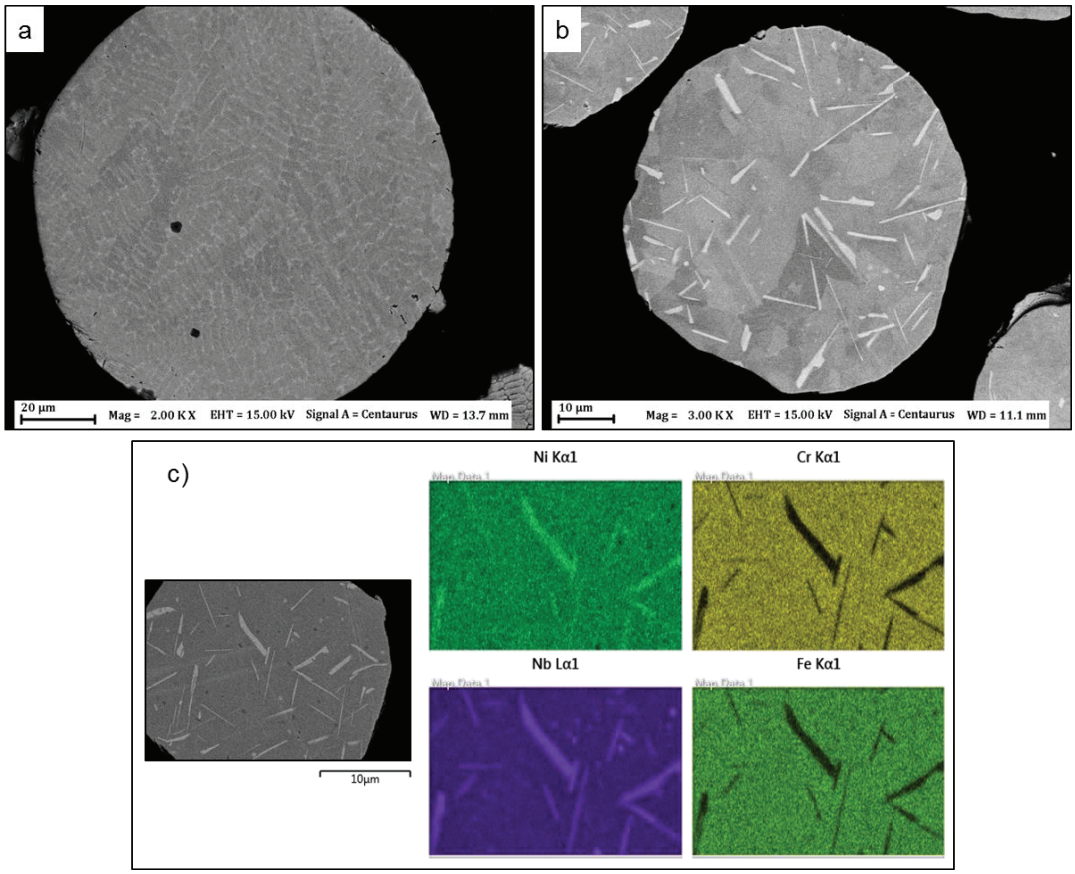

Figure 10. Microstructure of Alloy 718 EBM powder in (a) virgin condition; (b) after 14 re-use cycles; (c) EDS map showing delta phase in a powder after 14 re-use cycles (author's experimental result).

4. Defects in additively manufactured superalloys

Porosity, microcracks and detrimental phases, such as non-metallic inclusions (NMIs) and unwanted secondary phases, are all defects commonly encountered in PBF fabricated parts [25]. Depending on their size, shape and distribution, they may act as potential failure initiation sites and may therefore have a negative influence on the performance of AM parts. It should be noted, however, that relative densities in the order of 99.9% [26] are commonly reached for many materials with today's PBF technology and that mechanical properties are often reported to be equal to, or in some cases, in excess of those for conventionally processed counterparts [8], [26].

Porosity has different origins and is divided into different groups such as gas porosity, shrinkage porosity, keyhole porosity and lack of fusion defects (LOFDs) [71]. Gas porosity, as presented in Figure 11 (a), consists of small, near-spherical pores containing gas that is trapped in the metal during solidification of the melt pool, often arising from gas entrapped inside the powder during gas atomization [25], [71], [72]. Shrinkage porosity forms when the flow of metal is not sufficient to compensate for the shrinkage during solidification [32]. Keyhole porosity is connected to the application of high energy densities during the AM process and occurs as a consequence of the entrapment of vapor bubbles inside the melt pool [73]. Finally, the LOFDs, as presented in Figure 11 (b), are to a large extent connected to the volumetric energy input and form in un-melted zones in the powder bed [7].

Non-metallic inclusions and unwanted secondary phases, as illustrated in Figure 11 (d) and (e), respectively, are to a large extent connected to the alloy chemistry and form due to extensive segregation of certain alloying elements or due to reactions between reactive alloying elements (e.g. Al, Ti) and trace elements, such as oxygen and nitrogen [25]. The NMIs and LOFDs in EBM fabricated Alloy 718 are connected to powder re-use and are thus explained in more detail in Sections 4.1 and 4.2, respectively.

In LPBF processed IN-738LC, on the other hand, the most critical defects are microcracks, as depicted in Figure 11 (c). Microcracks are generally connected to metallurgical reactions and are therefore an alloy-specific problem mainly present in difficult-to-weld materials [7]. A more detailed description of this defect type is presented in Section 4.3.

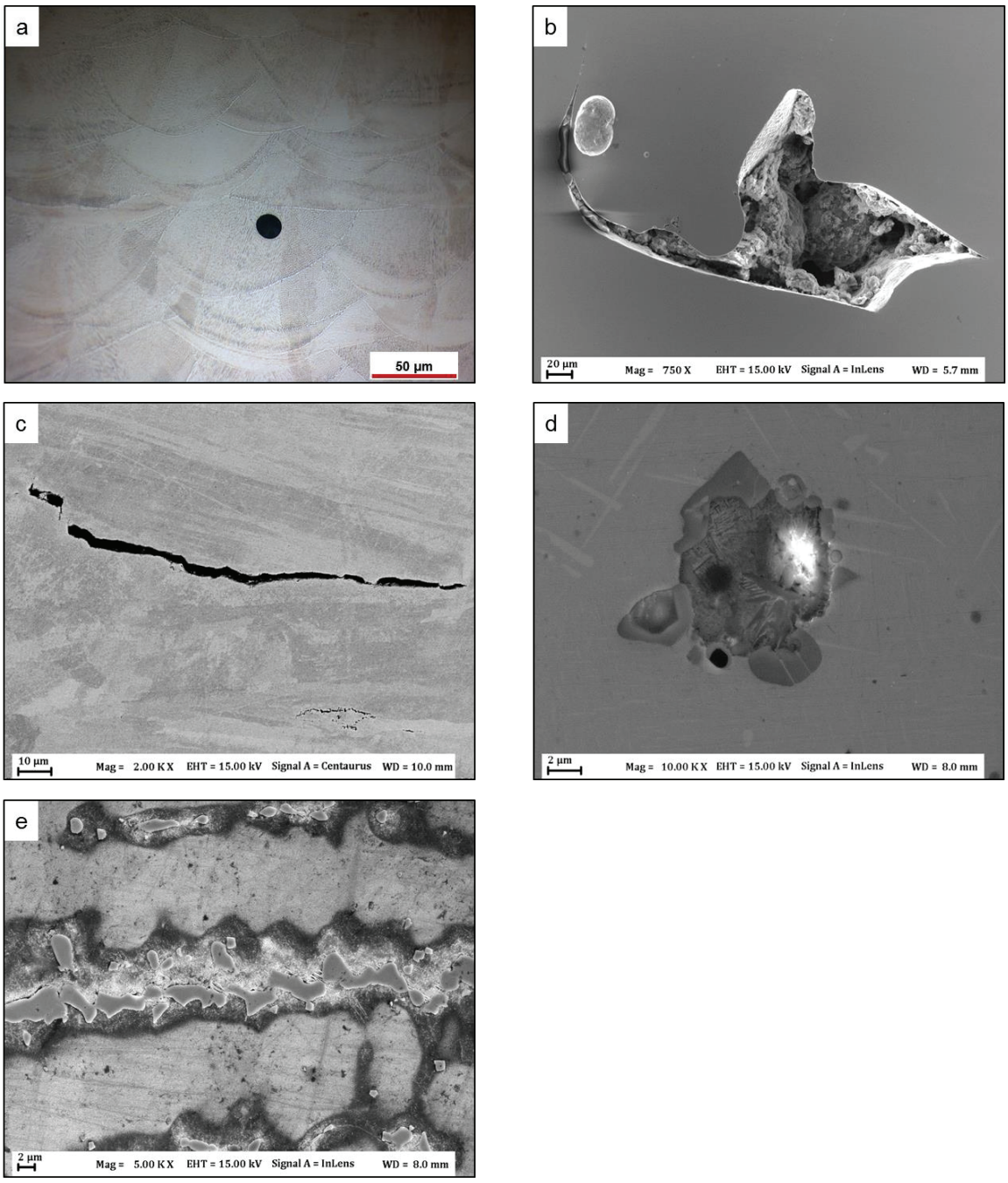

Figure 11. Defects commonly observed in AM parts: (a) gas porosity in 316L fabricated by LPBF; (b) lack of fusion defect in EBM fabricated Alloy 718; (c) micro-crack in IN-738LC fabricated by LPBF; (d) non-metallic inclusion (Al-oxide/Ti-nitride) in EBM fabricated Alloy 718; (e) laves phase in Alloy 718 fabricated by wire DED (author's experimental result).

4.1 Non-metallic inclusions

Non-metallic inclusions (NMIs) are compounds of metallic and non-metallic elements (usually O, S, N) present in the metal matrix [74]. For cast, forged and welded products, as well as AM and PM materials, NMIs may have a detrimental effect on mechanical performance of various alloys, especially on the reliability of rotating parts [60], [75]. For example, it has been shown that component life in wrought and cast parts is often limited by fatigue failures initiated at oxide inclusions, which is a common NMI in NBSs [4]. NMIs are also a major cause for rejection of

rotating part forgings [76]. Furthermore, the size of damage-relevant inclusions is too small to rely on non-destructive testing alone, which can only detect relatively large inclusions [3].

In traditional superalloy metallurgy, the presence of large NMIs in critical parts has been limited by careful selection of the raw material and by applying a series of vacuum melting and refining steps, wherein the impurity level is reduced to acceptable levels. Thus, modern casting and forging industries have managed to reduce oxygen to low levels (10-20 ppm) [60].

In general, the small volume of material in liquid state and the high solidification rate in AM limits the size of NMIs that can form. Therefore, in this sense, AM is a potential candidate for the production of clean materials [3]. However, the source of oxygen is usually larger in AM and PM compared to conventional steelmaking due to the oxidation of the powder surface during powder production or handling (as described in Section 3.2.2), which may lead to a reduced mechanical performance. In Ref. [60] for example, it was shown that a LPBF fabricated 316L steel with an oxygen level of 384 ppm (corresponding to 0.23 vol.% oxide phase) had a considerably lower impact toughness, 130–150 J, compared to the wrought counterpart with an oxygen level of 23 ppm, which had an impact toughness of 200–350 J. The reason reported for the reduced toughness was the presence of Si- and Mn-rich brittle oxide inclusions with a size of 50 nm–1μm, which acted as early initiation sites for micro-void formation [60].

Formation and stability

Based on their origin, NMIs are often divided into exogenous and endogenous inclusions. Exogenous inclusions originate from external sources such as fragments of refractories and entrapped slag, while endogenous inclusions occur due to chemical reactions between elements in the molten metal. Although mainly studied in casting, the latter is an intrinsic problem during the melting of alloys that contain reactive elements and may therefore occur in any other liquid metal process, such as powder atomization, welding or AM. Endogenous NMIs form as a consequence of the strong tendency of reactive elements, such as Al and Ti, to form chemical compounds with non-metallic elements, such as oxygen, nitrogen and sulphur. This makes the solubility of these elements (i.e. the solubility product of the compound) extremely small in the metal matrix [77]. The solubility product is temperature dependent, and therefore, NMIs precipitate upon cooling of the melt when the concentrations exceed the solubility product of the compound [78].

Presence of NMIs in precipitation strengthened superalloys fabricated by EBM and LPBF has been reported in literature [3], [25], [34], [79]. They largely occur as small, evenly distributed oxide and nitride inclusions [79]. In addition, in the EBM fabricated Alloy 718, the amount and morphology of NMI stand in close relation to the powder oxygen level, which increases with progressive powder re-use and requires a more careful description.

There are two major types of NMIs in Alloy 718: titanium nitride (TiN) and aluminum oxide (Al_2O_3) [80]. The primary carbide NbC also precipitates in the melt but is usually considered as part of the alloy microstructure [80]. As noted in Table 3, O and N have very low solubilities, which means that extremely low levels are required to avoid formation of NMIs. The oxygen level in particular must be reduced to extremely low levels to avoid formation of oxide inclusions [76]. Furthermore, also for very low O and N levels, precipitation is expected above the solidus temperature. Thus, the population of NMIs can only be modified during the melting process while it is more or less unaffected by subsequent heat treatments.

Table 3. Solubility limits of O and N in Alloy 718 at the liquidus and solidus temperature [34]

Element	Solubility limit at T_L (ppm)	Solubility limit at T_S (ppm)
N	37	5
O	5	2

The size of NMI defects, however, can be reduced by lowering the O and N levels to avoid precipitation until late in the solidification process. For cast and wrought superalloys, this is achieved first by primary melting in vacuum (VIM), in which the levels are lowered primarily through interaction with carbon to form CO (carbon boil), which is then desorbed by the vacuum. In this way, oxygen levels in the 20 ppm range are achievable [4]. Further reduction is made possible by applying one or several re-melting steps, including electroslag re-melting (ESR), vacuum arc re-melting (VAR) or electron beam cold hearth re-melting (EBCHR). The latter, which relies on dissociation and desorption (vacuum refining) and physical separation of inclusions that float to the melt surface, has been identified as an effective method for the removal of impurities and inclusions [18], [75], [76]. In this manner, single ppm oxygen levels have been attainable in ingot-castings and in re-melt stock for investment casting [18], [76].

NMIs in the powder production and PBF

The O and N levels commonly observed in the Alloy 718 atomization precursor wire, EBM powder (virgin and re-used) and EBM fabricated solid samples investigated in this thesis study are listed in Table 4. For all material conditions, the oxygen and nitrogen levels are well above the solubility limits in Table 3, and therefore, some amount of Al_2O_3 and TiN is expected. However, while many studies have addressed the microstructural characterization, those dedicated to non-metallic inclusions, such as that of Polonsky et al. [25], are scarce. Due to the high temperature under the electron beam, which has been reported to be around 3000°C [34], it is suggested that the dissolution of NMIs occurs during EBM. Similar effects have been suggested to occur during plasma atomization, which also takes place at high temperatures. Yet, it is known that stable non-metallic phases may persist through powder production [4] and electron beam melting [3].

Table 4. Oxygen and nitrogen levels in the Alloy 718 wire, powder and solid samples investigated in this study

Material	O (ppm)	N (ppm)	C (ppm)
Wire	~75	~150	~440
Powder – virgin	~150	~150	~370
Powder – re-used*	~300	~150	~370
Solid – virgin	~75	~150	~300
Solid – re-used**	~150	~150	~300

** Powder after approximately 30 re-use cycles, corresponding to a total process time of approximately 1000 hours. ** Solid material built from the re-used powder* [81].

Furthermore, the solvus temperature is composition dependent and increases with analytical content of the elements in the compound. Following this concept, the calculated solvus temperatures for Al_2O_3, TiN and NbC based on an average composition of re-used Alloy 718 powder (Table 4) are provided in Table 5. Among these phases, Al_2O_3 is present at the highest temperature, followed by TiN and finally NbC, which precipitates just above the matrix solidus temperature. These values are all lower than the peak temperature reported for EBM. However, it

should be noted that even though the temperature in these processes may be high enough for dissolution to occur, the high solidification rate in EBM limits the residence time at the high temperature necessary for dissolution [4], [82].

Table 5. Solvus and melting temperatures for NbC, TiN and Al_2O_3 in Alloy 718; the solvus temperatures are calculated with JMatPro based on the C, N and O levels in the re-used powder in Table 3 (250 ppm of oxygen, 150 ppm of nitrogen, 370 ppm of carbon); the full composition of the as-received Alloy 718 powder is shown in Table 6; the melting temperatures are calculated with HSC Chemistry 9.7.1.0.

Phase	Solvus temperature (°C)	Melting temperature (°C)
NbC	1260	3490
TiN	1640	2930
Al_2O_3	2050	2072

The nitrogen level in Table 4 is stable at around 150 ppm for all material conditions, which indicates that the amount of TiN is stable during powder production, powder re-use and electron beam melting. In addition, all three material conditions contain similar TiN particles, with sizes varying from sub-micron up to approximately 10 μm. In many cases, they consist of an Al_2O_3 core and an outer TiN rim, as presented in Figures 12 and 13. Both powder atomization and EBM are associated with rapid solidification rates, and therefore, there is limited time for particle growth. In turn, the morphology of the TiN and Al_2O_3 particles, which is similar for all material conditions, suggests that at least the larger inclusion sizes of the population of TiN particles are likely inherited from the atomization precursor material, i.e. from the wire.

The wire also contains large primary NbC carbides, as in Figure 12. In some cases, they are nucleated on the TiN particles. Such structures are not seen in the powder or in the solid samples. This indicates that the temperature during atomization is high enough to dissolve NbC, which is the least stable phase according to Table 5. The continuously decreasing carbon level along the process chain, from wire to powder and finally EBM fabricated material, suggests that some amount of carbon is removed during atomization and EBM processing, while the remainder re-precipitates upon cooling [77].

It should be noted that the observed oxide-nitride-carbide particles are known to exist in various metal systems. The structure corresponds to the sequence of nucleation of these phases in the melt, which, according to the solvus temperatures in Table 4, starting with Al_2O_3, followed by TiN and lastly NbC [34].

As a consequence of oxygen pick-up during powder production, the powder oxygen level is higher than in the wire. Moreover, the amount of oxide increases significantly during powder re-use, as described in Section 3.2.2. The oxygen level in the solid samples is around half compared to the powder from which it was built, which suggests that some amount of oxide refining occurs during the EBM process.

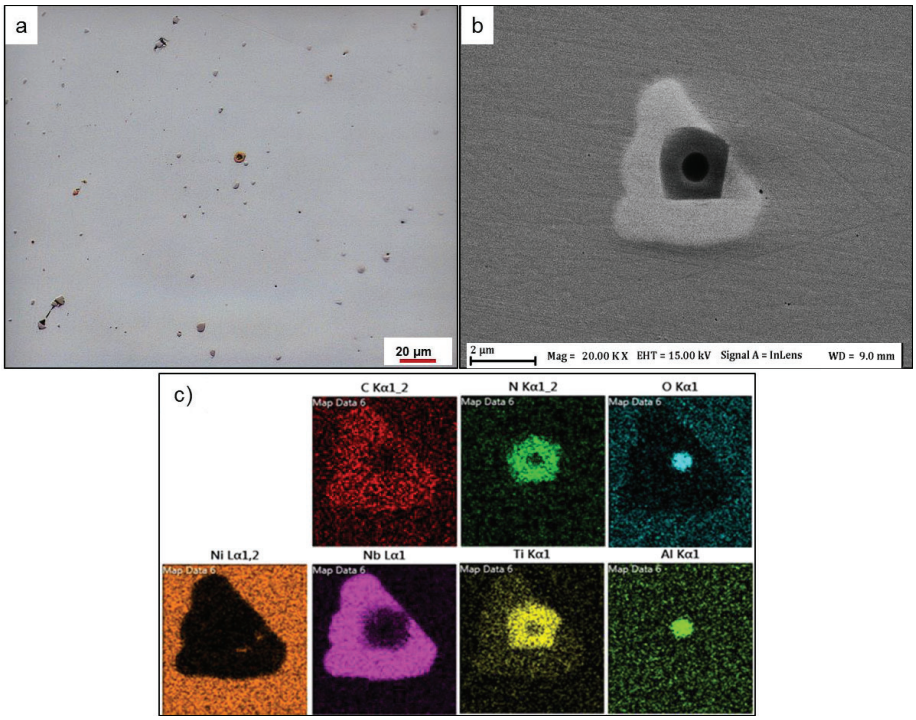

Figure 12. (a, b) NbC/TiN/Al_2O_3 inclusion in the Alloy 718 wire (atomization precursor material) with corresponding EDS map in (c); (author's experimental result).

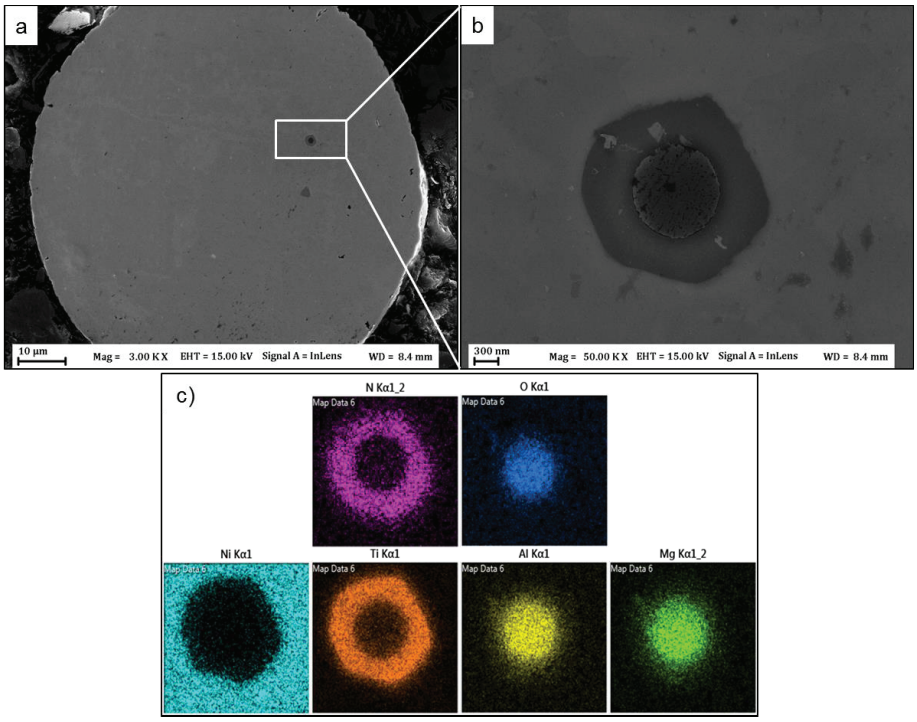

Figure 13. (a, b) TiN/ Al_2O_3 inclusion in a plasma atomized Alloy 718 virgin powder with corresponding EDS map in (c) [81].

In the EBM fabricated samples, oxide exists as particulates and as continuous films or flakes, as shown in Figure 14. As is described below, the tendency of the oxide to agglomerate in the melt results in the formation of large NMIs. Presence of large NMIs is especially the case in samples fabricated from re-used powder, whereby the increased amount of oxide is the major source for NMIs.

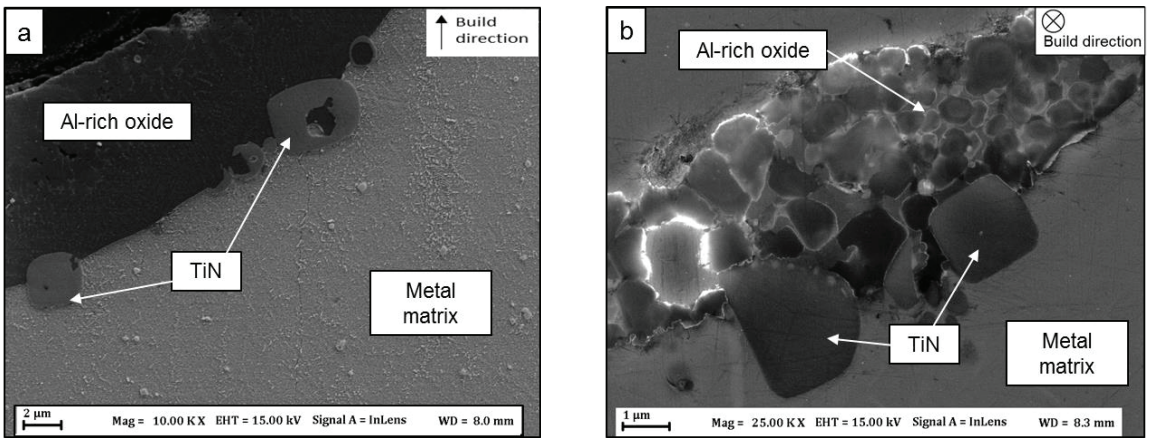

Figure 14. EBM processed Alloy 718: (a) TiN inclusions in an oxide flake in a sample built from 30 times re-used powder; (b) clustered TiN and oxide inclusions in a sample built from 14 times re-used powder (author's experimental results).

Agglomeration of non-metallic phases

The agglomeration of NMIs in the liquid melt is a phenomenon well-known in the casting industry [83]. In the case of sub-micron inclusions, it is reported to be a result of collision of the inclusions which is mainly governed by the turbulence present in the melt [84]. The collision and agglomeration of single alumina particulates is promoted by long-range attraction forces [83]. When inclusions collide, they tend to coalescence or agglomerate if the interfacial tension between particle and melt is high [85]. In EBM processed Alloy 718, oxide particulate clusters with the size of several tens of µm are frequently present in samples produced from re-used powder, as illustrated in Figure 15. The individual oxide particulates have sizes and shapes similar to those observed on the surface of the re-used powder, as in Figure 9. This suggests that they persist through the melting process and cluster in the molten metal. No such clusters were observed in samples produced from virgin powder [86].

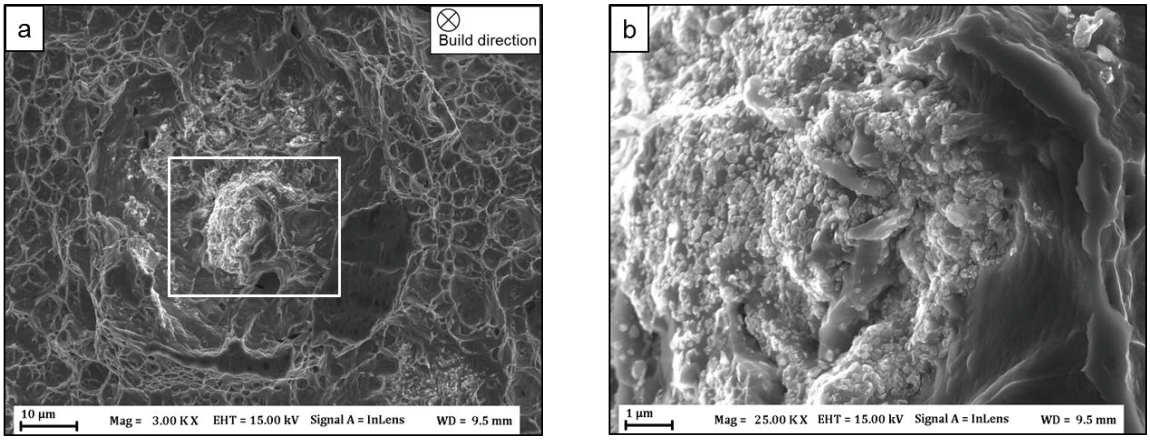

Figure 15. Cluster of Al-rich oxide inclusions in an EBM Alloy 718 sample fabricated from 30 times re-used powder [81].

Similar phenomena are apparent in LPBF, as illustrated Figure 16, for which equally sized TiN inclusions are present in the atomized Alloy 718 powder in Figure 16 (a) and in the fabricated solid sample in Figure 16 (b). In this case, the melting of the raw material as well as the atomization were done in a nitrogen atmosphere that enables TiN formation through reaction of N with Ti in the

melt before atomization. Also in this case the inclusions are found as agglomerates in the AM fabricated material, indicating that particulate agglomeration occurs in the melt, as reported in earlier studies [3], [25], [87]. As mentioned in Section 3.1.3, similar phases can also originate from entrapped refractory material from the crucible or nozzle in the atomizer [88].

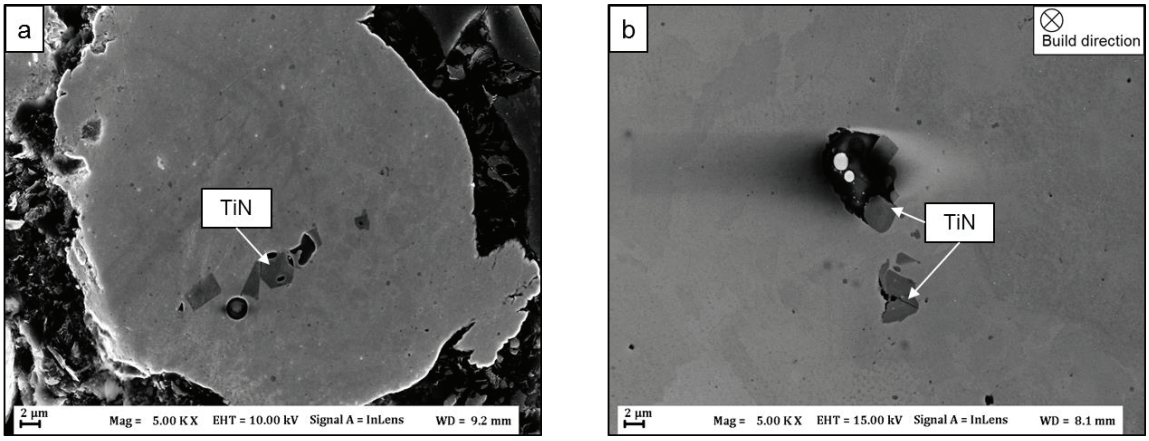

Figure 16. TiN particles in (a) gas atomized Alloy 718 powder; (b) the solid sample fabricated by LPBF (author's experimental result).

Large inclusions composed of agglomerates mainly form as a consequence of the macroscopic melt flow, a process that is more effective when the phases are in liquid state [84]. As the melting temperature of Al_2O_3 (2072°C) can be reached in EBM, this may result in the formation of large continuous oxide films or flakes, as shown in Figure 17. The oxide often incorporates nitride particles that form large, brittle defects together with the oxide. This effect is especially evident in samples produced from re-used powder wherein the number density and size of NMIs is considerable. Similar oxide inclusions have previously been observed in EBM processed Alloy 718 [34]. In contrary, oxide inclusions present in LPBF and DED fabricated material are usually reported to form mainly due to pick-up of oxygen from the processing atmosphere [89], [90].

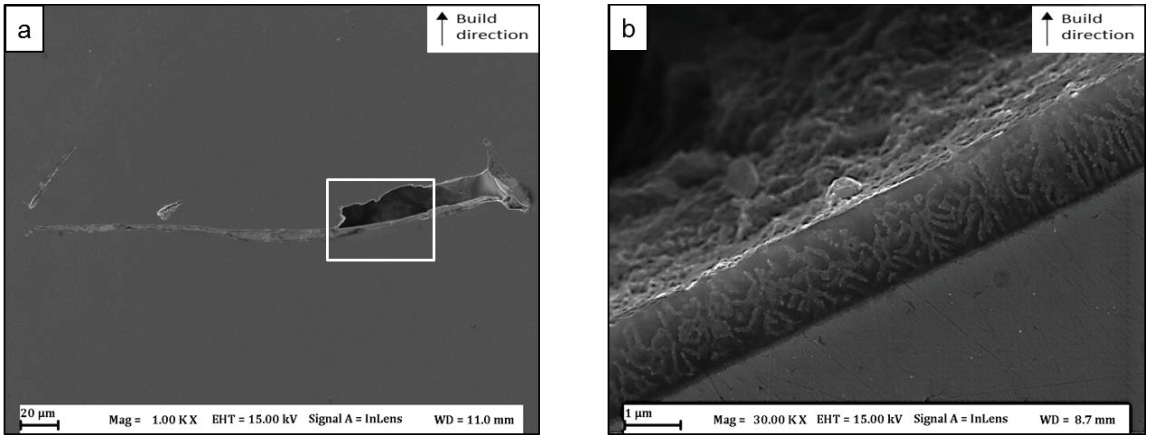

Figure 17. Large oxide flake in EBM processed Alloy 718 sample built from 30 times re-used powder [81].

Floatation of non-metallic phases

Flotation of many NMIs is a natural occurrence through buoyance effects since the density is often lower than that of molten metal (3.95 g/cm^3 for alumina and 5.4 g/cm^3 for TiN in comparison to 8.22 g/cm^3 for Alloy 718). In casting, this process is reported to be more efficient for larger particles and is limited to inclusions above 30 µm [83]. For EBM, however, it has been suggested that the

solidification rates are too high for effective buoyancy forces to occur. Instead, thermocapillary (Marangoni) forces, as illustrated in Figure 18, are assumed to be the major mechanism for flotation of non-metallic phases in EBM [25].

The Marangoni flow is driven by large thermal gradients and consequently large surface tension gradients across the melt pool surface. When the level of surface active elements such as O or S exceeds around 10 ppm, the surface tension temperature dependence changes from positive to negative, as presented in Figure 18. This has the effect of the particle trajectory being directed radially inwards toward the hotter region at the top center of the melt pool. Hence, as a consequence of layer re-melting, NMIs may be transported from layer to layer along the building direction toward the top surface.

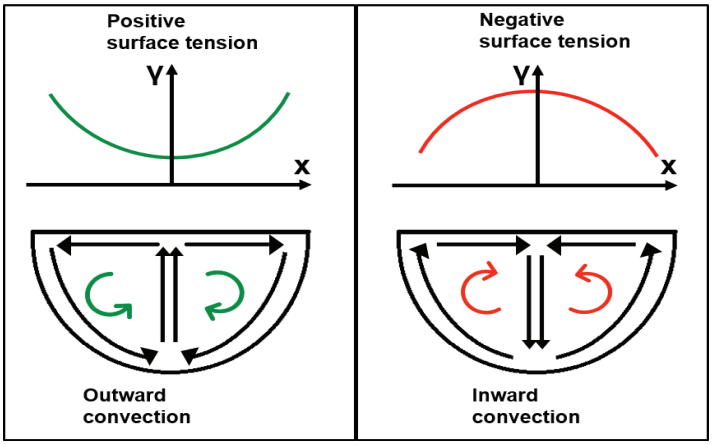

Figure 18. Illustration of the Marangoni effect on the trajectory of particles in a melt pool (redrawn from [91]*).*

A large amount of oxide on the top surfaces of EBM fabricated Alloy 718 built from re-used powder, as shown in Figure 19 (a-c), confirms that this is the case. The large amount of oxide on the top surfaces also indicates that some amount of refining of the bulk material takes place during the melting process, which is one reason for the lower oxygen level in the bulk solid sample compared to the powder from which it was built. However, the oxide may also become entrapped in the melt due to the turbulence, forming defects as illustrated in Figure 19 (c). Similar inclusions, so-called oxide bi-films, are also formed due to turbulence during casting of Ni-base superalloys [92]. The lower amount of oxide in the samples produced from virgin powder is confirmed by an almost complete absence of oxide on their top surfaces, as depicted in Figure 19 (d).

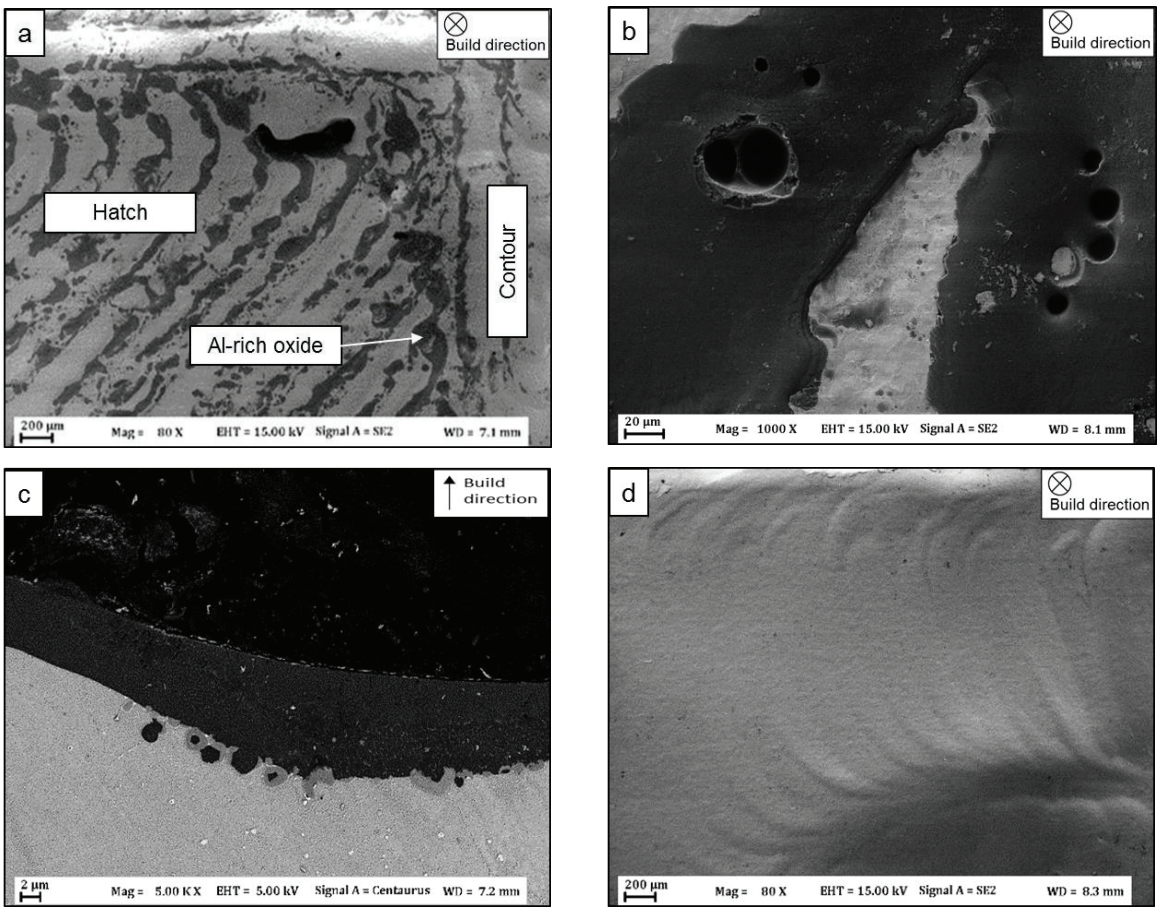

Figure 19. (a-c) Top surface of EBM processed Alloy 718 built from 30 times re-used powder; (a, b) top view; (c) cross section; (d) top view of sample built from virgin powder [81].

4.2 Lack of fusion defects

Lack of fusion defects (LOFDs) occur when the overlap between adjacent melt pools is insufficient. In general, the presence of LOFDs is process dependent and typically occurs when using non-optimized process parameters or due to anomalies in the process such as a temporary decrease in beam power or irregularities in the thickness of the powder layer [25]. Therefore, LOFDs is a problem found in most alloying systems [93]. In a study on the fatigue properties of Alloy 718 fabricated by EBM and LPBF, it was reported that the EBM fabricated variant contains a higher number of large LOFDs [87]. These large LOFDs are especially located at the interface between the hatch and contour regions, as shown in Figure 20, for which the reason is twofold.

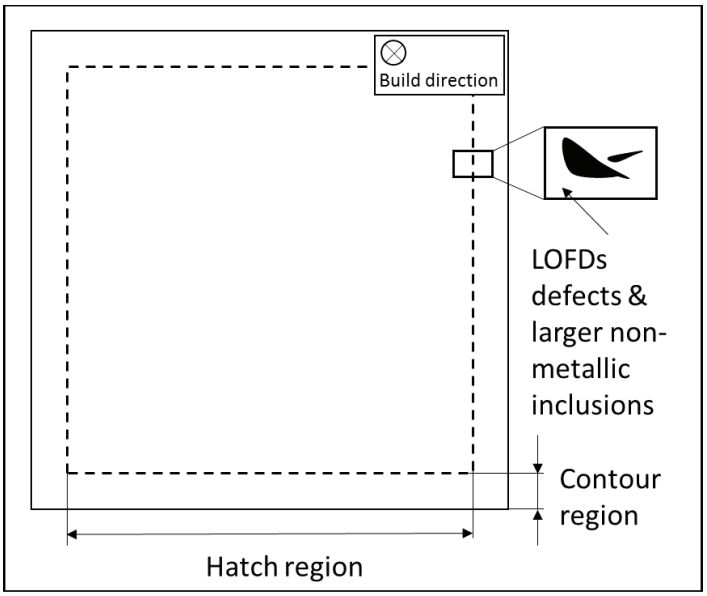

Figure 20. Predominant position of LOFDs at the interface between the hatch and contour regions in EBM processed Alloy 718 (author's illustration).

First, as the electron beam follows the hatch scan pattern, as in Figure 3 excessive melting may occur at the turning points, resulting in the formation of a crater in this particular area. In this case, the successive powder layer may locally be too thick to reach full consolidation. Hence, the stacking of LOFDs along the build direction may occur in this particular region, as shown in Figure 21 (a).

Second, as is seen on the top surface of the samples built from re-used powder in Figure 19 (a), a large amount of oxide may accumulate at the electron beam turning points. As oxide is known to negatively affect the wetting process, this leads to a further increased risk of LOFD formation [89]. An increased number of LOFDs in samples produced from re-used powder, together with large amounts of oxide inside the LOFDs, as shown in Figure 21 (b-d), confirm this theory. Similar observations have been noted in other studies [87].

In addition, the oxidized surface of the re-used powder could lead to reduced energy absorption or powder bed conductivity. This may have a negative effect on the sintering behavior and therefore the ejection of powder (powder smoking), with the formation of LOFDs in the subsequent layer as a result [25].

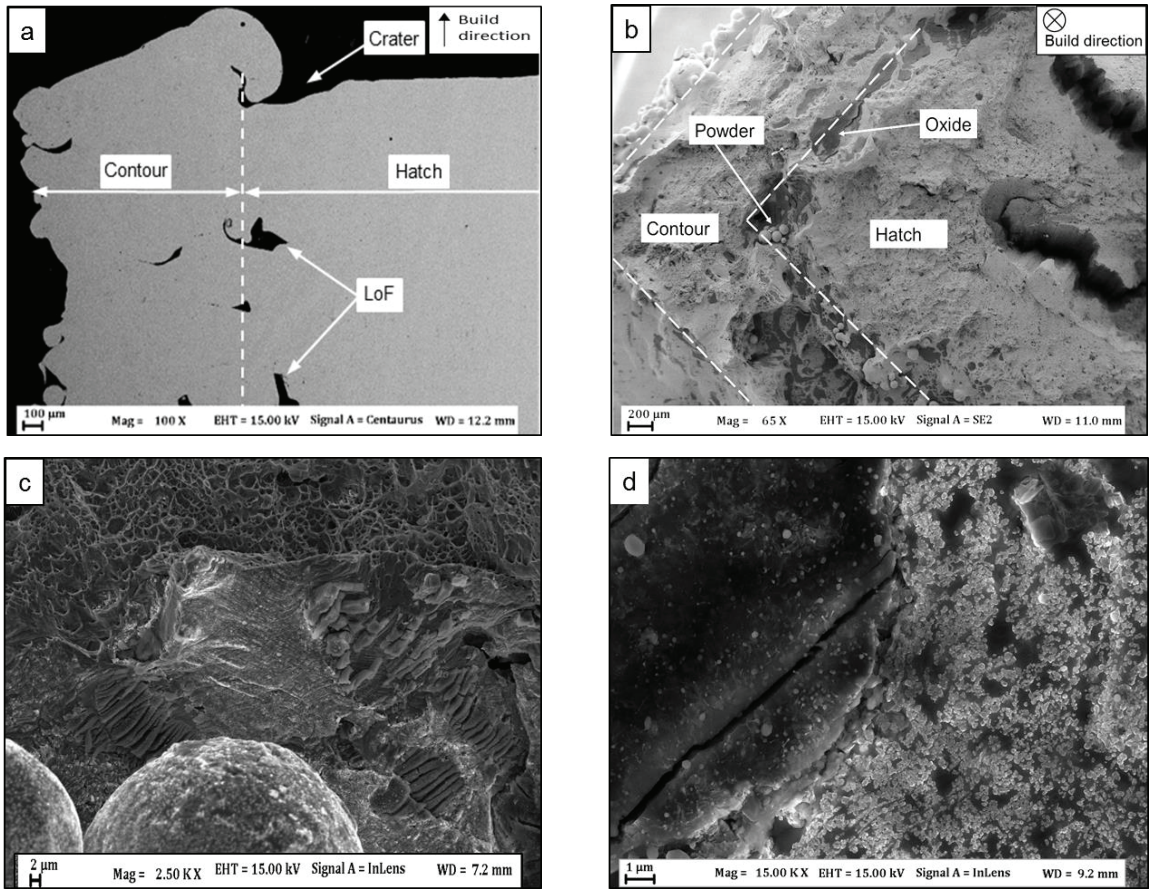

Figure 21. The LOFDs present at the interface between the hatch and contour regions in an EBM processed Alloy 718 sample fabricated from 30 times re-used powder; (a) cross section parallel to the build direction; (b) fracture surface perpendicular to the build direction; (c, d) higher magnification of oxidized powder and oxide films/flakes inside LOFD in (b); (author's experimental result).

Furthermore, oxide containing LOFDs in samples built from re-used powder cannot be eliminated by means of HIP. Instead, after HIP, large networks of oxide remain inside the collapsed LOFDs, as illustrated in Figure 22.

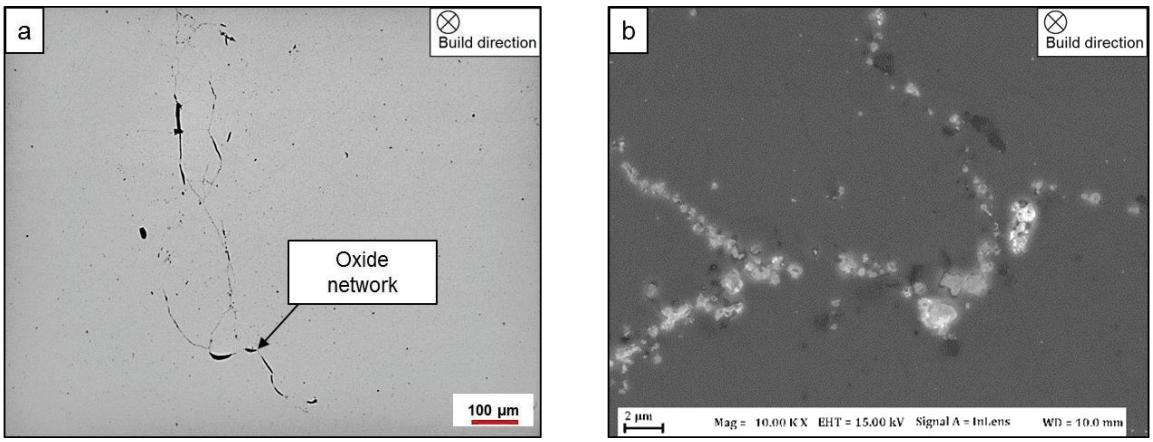

Figure 22. Network of Al-rich oxide inside a collapsed LOFD in an as-HIP EBM processed Alloy 718 sample fabricated from 30 times re-used powder [81].

4.3 Cracking

The cracking of Ni-base alloys in casting and welding is a well-known problem that has been widely studied for over 50 years [20]. Recently, many NBSs have shown susceptibility to cracking also when processed by AM, including PBF [7], [8], [94]. Since PBF is largely analogous to laser/electron beam welding, the weldability concept may function as an indicator for the suitability of an alloy to be processed by PBF [95].

Similar to welding, the mechanical drivers for cracking in AM arise from stresses caused by thermal contraction upon solidification and cooling as well as from strain imposed by the thermal gradient along the build direction [94]. The NBSs have high modulus of elasticity, large thermal expansion coefficient and low thermal conductivity, which makes them inherently difficult to process through welding and AM [94], [96], [97]. Thermally induced strain can be reduced by changing the process e.g. through optimization of the process parameters [98] and the scanning strategy [96], [99] or by using heated build platforms to reduce local strains [6], [100]. The latter is the reason why residual stresses are higher in LPBF than EBM, where the build is held at an elevated temperature (see Section 3.1.4).

Four cracking mechanisms are often mentioned in AM literature. First, solidification cracking and liquation cracking result in hot cracks, as they form at temperatures where the material is partly in liquid state. Next, strain age cracking and ductility dip cracking are classified as solid state cracking mechanisms as they occur at lower temperatures, without presence of a liquid phase.

As a result of the complex thermal history induced by the AM process as well as the complex chemistry of many NBSs, several of the mentioned mechanisms may be active [95]. Thus, the cracking mechanisms that are active in many AM fabricated NBSs are under debate [101].

4.3.1 Hot cracking

Hot cracks occur in the fusion zone or in the partially melted zone (PMZ) of the heat affected zone (HAZ). Although hot cracking frequently occurs in solid solution strengthened and precipitation strengthened Ni-base alloys, the more complex chemistry of the precipitation strengthened alloys may increase their susceptibility [19]. Crack surfaces exhibiting dendritic structures with limited presence of secondary dendrite arms indicates the presence of a liquid film during crack formation [7].

Hot cracking is known to occur at high-angle grain boundaries [97]. [102]. Based on a model established by Rappaz et al. [103], it was concluded that a liquid film at a solid-liquid interface on a dendritic boundary is inherently unstable. However, with increasing grain boundary energy (i.e. increasing grain misorientation) the film becomes more stable. Hence, a liquid film at a high-angle grain boundary can exist at lower temperatures than that of a low-angle grain boundary [102], [103], and therefore, dendrite bridging can occur first at a certain undercooling.

To weaken the grain boundary to the extent that the microstructure is susceptible to cracking, the film must reach a specific thickness. This may be promoted by a coarse grain structure wherein the elemental segregation is higher [104]. The long, straight epitaxially grown columnar grains associated with PBF may also have lower crack resistance than equiaxed grains since they provide channels in which liquid can converge into continuous films more easily, with high tensile stress perpendicular to the grain boundaries [101].

Solidification cracking

Solidification cracks occur inside the solidifying melt pool during terminal solidification, when a liquid film is present at the end of the liquid-solid (mushy) zone, where almost full coalescence between dendrite arms is established. At this stage, strain induced by thermal contraction may not be accommodated by liquid feeding, which is limited in this zone [2], [103]. Thus, cracks form at the solidification grain boundaries when liquid films are maintained to temperatures where the material is unable to accommodate thermally induced strains on solidification and cooling [19], [104], [105].

The solidification cracking susceptibility is largely dependent on the local solidification temperature range, the amount of terminal liquid, the liquid film surface tension and the grain boundary energy. Furthermore, for cracking to occur, the liquid film must be able to penetrate and wet the grain boundaries [20], [104]. This is promoted by a low surface tension liquid whereby extensive wetting of dendrites can occur so that solid-solid bridging is interfered. When a small amount of liquid is present, it tends to exist as isolated pockets instead of a continuous film. On the other hand, back-filling of the cracks can occur when a large amount of liquid is present. Thus, the most detrimental case is a moderate amount of low-melting liquid with a low surface tension [19].

It is proposed that many elements, including Zr, B [6], Si, Mn [106], Ti [104], S, O, N, P, C, and Nb [20], [107] may cause weakening of the grain boundaries in different NBSs due to depression of the local melting temperature when enriched during solidification. Solidification cracking of less alloyed systems is often related to segregation of trace elements such as S and P. Moreover, it is known that sulphur may form low melting eutectics together with Ni [108]. Since these elements provide no beneficial effects on the performance of NBSs, their content should be held as low as possible. Levels of <0.003 wt.% S and <0.01 wt.% P have been recommended when resistance to solidification cracking is important [19].

In more heavily alloyed systems, eutectic reactions at the end of solidification, which expands the local solidification temperature range to below the solidus temperature, may have a stronger effect on the cracking susceptibility. This is believed to be the case in creep resistant alloys, where small levels of C, B and Zr may cause eutectic formation of carbides, borides or intermetallic phases at relatively low temperatures (M_3B_2~1200°C, ZrS and TiS ~1170°C) [19], [108]. Moreover, it has been reported that Zr and Si at the grain boundaries change the interfacial energies and therefore increase the undercooling required for full solidification [102]. In addition, surface active elements such as B, S and Zr are critical as they lower the surface tension, which creates a terminal liquid that wets and spreads well along grain boundaries. The elements B, S and P are also heavily enriched in the liquid due to their low solubility in Ni. Synergic effects of B and Zr have also been reported as well as together with those of S [19]. As a result, contents of Zr below ~0.04 wt.% when B is held to 0.001-0.005 wt.% are recommended. Any Zr additions have been identified as critical for B levels above 0.01 wt.%. The mutual presence of several of these elements as well as possible interactions among them make it difficult to determine their individual effects [19].

Solidification cracking has been proposed as the prevailing mechanism in several AM fabricated NBS systems. In the research of Cloots et al. [6], solidification cracking in IN-738LC processed by LPBF was suggested to be caused by Zr-containing low melting point films at the grain boundaries. The effect of Zr on the reduction of the solidus temperature was confirmed by thermodynamic modelling [6]. In the same study, B was also found to segregate at the grain boundaries but could not be connected to formation of the cracks. In a study by Chauvet et al. [7], low melting point

liquid films induced by grain boundary segregation of B were identified as the cause for solidification and liquation cracking of a precipitation hardening NBS processed by EBM. Tomus et al. [109] suggested that hot cracking during terminal solidification in Hastelloy X processed by LPBF was attributed to C and Si due to an enhanced formation of grain boundary carbides, a wider solidification range as well as an increased amount of eutectic. A similar reasoning was presented by Marchese et al. [110]. Furthermore, a strong correlation between Si content and microcrack density was presented for IN-738LC processed by LPBF [107]. Zhou et al. [111] claimed that solidification cracking in the NBS CSU-B1 fabricated by direct energy deposition (DED) was initiated at inter-dendritic shrinkage cavities and was promoted by Ta- and Hf-rich primary carbides, which hindered liquid back filling during terminal solidification. In a study by Ramakrishnan et al. [2], solidification cracking and liquation cracking in DED fabricated IN-738LC was reported. It was suggested that solidification cracking occurred due to formation of inter-dendritic low melting γ+γ' eutectics during final solidification, while liquation cracking was a consequence of grain boundary liquation of γ+γ' eutectics, carbides and borides during layer re-melting.

HAZ liquation cracking

Heat affected zone (HAZ) liquation cracking in welding typically occurs due to the local melting of grain boundary constituents in the PMZ of the HAZ as the temperature exceeds the effective (non-equilibrium) solidus temperature upon heating. As the ductility of the liquated grain boundaries drops to zero, cracks may easily form due to stress induced by solidification and cooling [20]. The HAZ liquation cracking may also occur during multipass welding when the previous weld passes become the HAZ [19]. Reheating of the previously deposited layers in AM has the same effect [95].

Segregation induced liquation is typically caused by grain boundary segregation of elements, such as S, P, B and C, which locally lower the melting temperature. As in the case of solidification cracking, the content of these elements is therefore kept within strict limits [20], [112].

Constitutional liquation is a non-equilibrium process and occurs below the equilibrium solidus temperature of the alloy. It takes place through eutectic-type reactions between the matrix and secondary phase particles such as intermetallics, carbides, borides, sulfides and silicides, usually located at the grain boundaries with formation of a solute rich liquid film at the matrix-particle interface. Constitutional liquation is largely connected to rapid heating as this limits the time required to dissolve the particle before reaching the eutectic temperature. In such a case, incomplete dissolution of the particle results in a concentration gradient around it, which locally reaches the eutectic composition and liquates when reaching the eutectic temperature [4]. It should also be mentioned that coarse particles are more likely to participate in constitutional liquation due to the higher temperature required for complete dissolution [20], [104], [105],. A similar mechanism occurs during rapid heating of materials which contain residual eutectic constituents that have formed through heavy segregation in inter-dendritic areas [20], [113]. The presence of liquated or re-solidified constituents along the crack opening is indicative of the liquation cracking mechanism [104].

Liquation cracking is generally proposed as the active mechanism in NBSs produced by DED. An example of this is reported in Zhao et al. [114], wherein cracking in Rene 88DT was explained to occur due to liquation of γ+ γ' eutectics along the columnar grain boundaries. Zhang et al. [101] suggested that liquation cracking in IN-738 produced by DED was attributed to eutectic melting of γ + γ' and M_2B + γ as well as constitutional liquation of MC carbides. Zhou et al. [111] reported

that liquation cracking in the NBS CSU-B1 DED fabricated material occurred due to liquation of Al- and Si containing inter-dendritic low melting point compounds in the HAZ.

4.3.2 Solid state cracking

Ductility dip cracking

Ductility dip cracking (DDC) is a solid-state grain boundary cracking mechanism related to a marked dip in ductility at a certain temperature range between the solidus and approximately $0.5*T_m$ [19]. DDC is promoted by the accumulation of strain at the grain boundary triple points or at irregularities, typically at high-angle grain boundaries [9], [42]. The welding literature suggests that DDC is strongly connected to grain boundary sliding and decohesion, which is often associated with excessive formation of intragranular carbide [95], segregation of S [112] and straight, un-pinned grain boundaries. Thus, controlling the grain boundary carbide precipitation to promote effective pinning of the grain boundaries in the vulnerable temperature range is often mentioned as a key factor for avoiding DDC [19], [20]. Moreover, DDC has been reported to occur during post-AM HIP treatment of LPBF fabricated CM247LC [115] as well as in DED fabrication of IN-738LC [101]. In the latter case, it is attributed to stress concentrations at the grain boundaries as a consequence of liquation cracks, precipitation of MC carbide and γ'. As in the case of liquid state cracking, it is suggested that the long, straight columnar grain structure typically associated with PBF makes the material more vulnerable to grain boundary sliding compared to more tortuous or equiaxed grain structures [101]. Furthermore, DDC is rarely reported as an active mechanism in LPBF processing of IN-738LC [101].

Strain age cracking

Strain age cracking (SAC) is a solid-state grain boundary cracking mechanism specific to precipitation strengthened alloys. It is generally believed that SAC in NBSs occurs as a consequence of loss in ductility from precipitation of the strengthening phase γ' in the presence of high strain, either from residual stresses or external restraint [4], [112]. When heating through the temperature range 595–980°C, the rapid formation of γ' precipitates causes the ductility to drop before substantial stress relaxation occurs [4]. Strain induced by the volume contraction from γ- γ' transformation has also been suggested as a contributing factor [19]. As increasing levels of Al and Ti lead to a more extensive and more rapid γ' precipitation, alloys with high Al + Ti content (>~4-6 wt.%) are usually considered prone to strain age cracking [95], [104], [116]. This relationship is indicated in the Prager-Shira diagram in Figure 23. In welding, SAC typically occurs due to local strain accumulation at the grain boundaries in the HAZ, when the strained weld material is reheated during post-weld heat treatments (PWHT) or during multi-pass welding [19], [20]. In the AM processing of NBSs, SAC is generally reported to occur during thermal post-processing and not during the AM process itself. As in welding, SAC is connected to high amounts of residual stresses and the rapid precipitation of γ' [42], [95], [115].

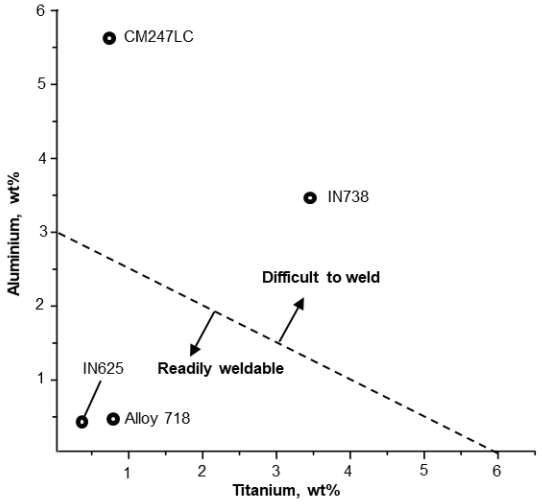

Figure 23. Relationship between Al and Ti content and the susceptibility to SAC of some Ni-base superalloys; alloys below the dashed area are SAC resistant while those above are susceptible to SAC (re-drawn from Ref. [19]*).*

4.3.4 Oxygen induced cracking

Intergranular cracking of NBSs is, as in the case of austenitic stainless steels, a well-known problem and is largely connected to the presence of brittle or liquid films that form due to segregation of impurities or minor elements such as S, P, O and Si. The effect of oxygen on the formation of brittle inter-dendritic films is known from welding [108] and casting [92]. In the latter, the crack-like defects known as bi-films, which arise from entrainment of oxide films due to turbulent pouring of the melt, play a central role in the failure behavior of cast as well as wrought Ni-base superalloys [92]. Moreover, as noted by Zhang et al. [101], grain boundary oxidation can promote propagation of grain boundary cracks according to mechanisms reported in the field of fatigue cracking: stress assisted grain boundary oxidation (SAGBO) and dynamic embrittlement. In the latter, a reduction of the grain boundary cohesion strength is promoted by short range diffusion of oxygen into the crack tip. Oxide in this case is believed to form behind the tip of the advancing crack. According to SAGBO, long range diffusion of oxygen causes the formation of oxide in front of the crack tip, followed by crack propagation by fracturing of the oxide or along the interface between oxide and matrix.

As described in Section 4.1, the oxygen level in PBF fabricated superalloys is often on the level of one order of magnitude higher than in cast and wrought counterparts. It should therefore be considered that microcracking observed in many AM fabricated NBSs may be affected by oxide, e.g. in the form of brittle or low melting films at the grain boundaries. However, at present, this factor remains more or less unexplored. For example, in Zhou et al. [111], Al- and Hf-rich oxide particles were detected inside solidification and liquation cracks in a NBS fabricated by DED. Similarly, in Ramakrishnan et al. [2], a strong segregation of Al-rich oxide was found around the cracked grain boundaries in IN-738LC fabricated by laser powder deposition. In both studies it was suggested that the oxide may have assisted or accelerated cracking. However, its possible role as the main reason for the cracking was not considered.

4.4 Defect removal by hot isostatic pressing

Hot isostatic pressing (HIP) is a densification process that occurs through the simultaneous application of temperature and high isostatic gas pressure. Largely related to the healing of macro-

and micro-porosity, the HIP is mainly used for the consolidation of metal powder and the densification of castings. Also in the field of AM, HIP has gained interest for the elimination of porosity and cracks present in the as-built condition [8], [25], [72], [117].

The driving force for the densification process is a reduction in surface area represented by porosity [118]. The densification mechanisms involve plastic yielding, creep deformation to collapse and close the pores and, finally, diffusion bonding across the interface of the collapsed pores. Thus, high temperature is applied to lower the yield strength and increase diffusivity. The temperature and pressure are chosen so that the pressure is above the reduced yield stress at the elevated temperature. For NBSs, the temperature should also be above the γ' solvus temperature to allow for creep deformation to occur [119]. Cast superalloy turbine blades are typically HIPed in the range of 1100–1280°C, which is between the γ' solvus temperature and the incipient melting point of the alloy [118], [119]. In the case of cast IN-738, HIP is usually conducted at 1200°C and 100 MPa.

Increasing HIP temperature leads to increased diffusion, which often results in grain growth. Increased diffusion may also lead to the coarsening or dissolution of precipitates. If the precipitates have a pinning effect on the grain boundaries, this may further speed up the grain boundary migration [118]. Higher pressure leads to accelerated plasticity and power-law creep and, thus, enhanced densification [118]. Therefore, by increasing the pressure, the HIP temperature may be lowered [118].

Non-metallic inclusions such as oxides and nitrides are largely unaffected by HIP due to their high thermal stability [3]. Furthermore, porosity that contains gases with low solubility in the matrix may not be completely healed. Hence, there is a risk that argon trapped in porosity formed during LPBF remain after HIP. Due to the isostatic pressure, only pores that have no connection to the outer surface can be closed. It has also been noted that accelerated precipitation or growth of carbide, for instance, may occur in NBSs during HIP treatment at certain temperatures, which might have a negative effect on alloy properties [114].

5. Experimental procedure

In this chapter, the studied materials as well as the used analysis techniques and testing methods are presented.

5.1 Powder and processes

5.1.1 EBM fabricated Alloy 718

Commercial Alloy 718 pre-alloyed powder was used as feedstock material in the EBM process. The powder was produced by plasma atomization of a wire precursor material in an argon atmosphere. The virgin powder was provided by Arcam AB, Sweden, and had a particle size distribution of 45-105 μm. Its chemical composition, presented in Table 6, complies with common Alloy 718 material standards such as AMS 5662. The oxygen and nitrogen levels in the virgin powder, as measured by inert gas fusion (see Section 5.4), were both in the order of 150 ppm.

Table 6. Chemical composition of the Alloy 718 powder as provided by the powder producer

Element	**Ni**	**Co**	**Cr**	**Mo**	**Ti**	**Mn**	**Nb**	**B**
wt.%	54.1	0.04	19.0	2.99	1.02	0.12	4.97	0.001
Element	**P**	**Ta**	**Al**	**Fe**	**Si**	**S**	**C**	
wt.%	0.004	<0.01	0.52	17.12	0.06	<0.001	0.03	

An ARCAM A2X EBM system, located at University West, Trollhättan, Sweden, was used for fabricating the solid samples. The samples were built using Arcam standard process parameters and melt strategies, with an acceleration voltage of 60 kV and a layer thickness of 75 μm.

The samples were built in four sequential build cycles. The first cycle began with 100 kg of virgin powder, from which the first sample set was produced. The following two sets were produced in cycles 6 and 14, using the same powder batch. Up to cycle 14, the addition of virgin powder was kept as low as possible and was limited to cycle 6, before which 20% was added. The last set was produced from a mixture of heavily re-used powder that had been exposed to up to 30 instances of powder re-use, corresponding to a total process time of approximately 1,000 hours.

An approximately 1 mm wide area around the sample edges was first built by applying three contour passes with a line offset of 300 μm. This was followed by a bi-directional hatch exposure at the sample core with a line offset of 125 μm. The hatch passes were rotated by approximately 72° between each layer. The samples had a geometry of 11x11x60 mm^3 and were built with the longitudinal direction parallel to the build direction. Standard Charpy V-notch (CVN) test bars with a geometry according to ASTM standard E2316-b were machined from the samples.

As described in Section 5.2.1, hot isostatic pressing (HIP) of the as-built samples was performed to enable quantification of non-metallic inclusions using image analysis. The HIP treatments were conducted in a Quintus QIH21 URC® (Uniform Rapid Cooling) molybdenum furnace, located at Quintus Technology AB in Västerås. The HIP treatments were done at 1200°C, 100 MPa for 4 hours, according to the profile in Figure 24.

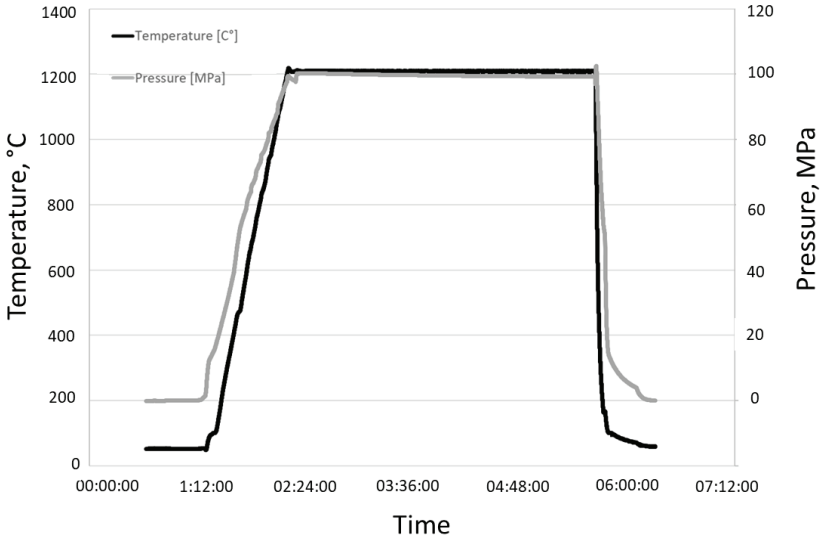

Figure 24. HIP profile applied for the as-built EBM fabricated material.

Samples of the re-used powder were collected before and after the above-mentioned EBM build cycles. Powder sampled from the sintered cake surrounding the built components shows the effect of exposing the powder to the conditions in the EBM process chamber. The samples collected before filling the powder into the powder hoppers after sieving reveal the overall condition of the powder used for sample fabrication. These samples were studied in conjunction with the solid samples built from the powder in question.

5.1.2 LPBF fabricated IN-738LC

Five pre-alloyed powder grades, based on the composition of IN-738LC, were studied, as noted in Table 7. The first four powder grades were used to study the influence of B and Zr on the susceptibility to microcracking during LPBF as well as the healing of microcracks by means of post-LPBF HIP treatment. Hence, four variants with B and Zr levels ranging from low B-low Zr (LB-LZr) to high B-high Zr (HB-HZr) were produced through controlled additions of B and Zr before powder fabrication. These powder grades were manufactured by Höganäs AB, Sweden, and were produced on a small scale (10-20 kg per batch), using a pilot vacuum induction gas atomizer (VIGA) with argon as atomization gas. The B level in the high B variants is above the maximum level according to specifications for IN-738LC (0.012 wt.%) [14]. All other alloying elements were kept within specified range (see Table 7).

Macrocracking during post-AM HIP treatment was studied on a standard IN-738LC grade (STD), a commercial grade provided by EOS Oy, Finland. All powder grades had a powder size distribution of 25-63 μm.

Table 7. Composition of the IN-738LC powder grades in wt. % with Ni as balance

Powder grade	B	Zr	Cr	Co	Al	Ti	W	Ta	Mo
LB-LZr	<0.01	<0.01	15.9	9.2	3.2	3.3	2.8	1.72	1.72
HB-LZr	0.03	<0.01	16.2	9.3	3.3	3.4	2.8	1.70	1.76
LB-HZr	<0.01	0.04	16.0	9.2	3.2	3.4	2.8	1.72	1.75
HB-HZr	0.03	0.07	16.0	9.3	3.2	3.3	2.9	1.73	1.72
STD	0.01	0.03	16.2	8.5	3.5	3.5	2.4	1.7	1.8
Powder grade	**Nb**	**Fe**	**C**	**S**	**P**	**Si**	**Mn**	**O**	
LB-LZr	0.9	<0.05	0.10	0.002	0.002	0.026	0.02	0.016	
HB-LZr	0.9	<0.05	0.11	0.002	0.006	0.040	0.02	0.014	
LB-HZr	0.9	<0.05	0.11	0.002	0.007	0.027	0.01	0.015	
HB-HZr	0.9	<0.05	0.11	0.002	0.007	0.027	0.01	0.015	
STD	1.0	<0.01	0.1	0.023	0.005	<0.001	<0.01	<0.001	

An EOS M100 (EOS GmbH) LPBF machine, equipped with a 200 W Yb-fiber laser, with a laser spot size of 40 μm in diameter, was used for small-scale fabrication of the cuboid samples used to evaluate the microcracking susceptibility, as well as cylinders to evaluate macrocracking during HIP. The M100 was operated using 135 W laser power, 1150 mm/s scanning speed, 60 μm hatch distance and 20 μm powder layer thickness.

An EOS M290 (EOS GmbH) LPBF machine, equipped with a 400 W Yb-fiber laser, with a laser spot size of 80 μm in diameter, was used for larger-scale fabrication of specimens for mechanical testing, which was conducted as part of the evaluation of microcrack healing by means of HIP. The M290 machine was operated using 210 W laser power, 1750 mm/s scanning speed, 50 μm hatch distance and 20 μm powder layer thickness.

Macrocracking during HIP was studied through HIP strategies with different temperature and pressure profiles, as well as heat treatment experiments at atmospheric pressure in a tube furnace. The healing of microcracks present in as-built condition as well as microstructural alterations during HIP was studied for the temperatures 1120°C and 1210°C under a pressure of 200 MPa at a duration of 4 hours. The HIP experiments were conducted in a Quintus QIH21 URC® (Uniform Rapid Cooling) molybdenum furnace, located at Quintus Technology AB in Västerås.

5.2 Microscopy

5.2.1 Light optical microscopy and image analysis

In general, light optical microscopy (LOM) was used for large scale examination of metallographic cross sections of powder and solid samples, before detailed analysis was performed using the scanning electron microscope.

Image analysis of light optical micrographs was used for quantification of non-metallic inclusions and lack of fusion defects in the EBM fabricated Alloy 718 built from progressively re-used powder. Quantification of non-metallic inclusions was performed after HIP treatment, which eliminates porosity and lack of fusion defects enclosed in the material. The distribution of non-

metallic inclusions was examined in the parallel and transverse directions as referred to the build direction.

The presence of cracks and unwanted phases in as-built and as-HIP IN-738LC produced from the powder grades in Table 7 was also studied by means of light optical microscopy.

5.2.2 Scanning electron microscopy

The scanning electron microscope (SEM) is a useful, versatile instrument often employed for morphological and elemental analysis. Secondary electrons (SE) originate from the near-surface region and are therefore used for high resolution imaging of the surface topography. The backscattered electrons (BSE) yield depends on the atomic number and is thus often used to determine the compositional contrast in the sample. Moreover, by detecting differences in phase conductivity (work function), the SE in-lens detector allows for enhanced phase contrast compared to a conventional secondary electron detector. Emission of characteristic X-rays upon interaction with the electron beam is used for micro-chemical analysis by energy dispersive X-ray spectroscopy (EDS). The spatial resolution of EDS is influenced by the interaction volume, which depends on the accelerating voltage and on the density of the sample but is often in the order of a micrometer. Integration of an electron backscatter diffraction (EBSD) detector in the SEM can be used to obtain crystallographic information of crystalline materials, such as texture, grain size and grain orientation.

In the present study, a Leo Gemini SEM (LEO GmbH, Oberkochen, Germany) equipped with a secondary electron in-lens detector as well as a solid-state EDS detector from Oxford Instruments (X-Max, Oxford Instruments Ltd., High Wycombe, UK) was used for morphological and micro-chemical analysis of powder and solid samples.

The surface morphology of the virgin and re-used Alloy 718 EBM powder was studied to map the extent of morphologically visible surface oxidation associated with progressive powder re-use. Powder cross sections were analyzed to detect non-metallic phases present inside the powder. SEM analysis of non-metallic inclusions present on the fracture surfaces as well as cross sections of the EBM fabricated samples was performed to determine the mechanisms behind defect formation associated with progressive powder re-use as well as to determine the effect of non-metallic inclusions on the fracture behavior of the EBM fabricated material.

The surface of the IN-738LC powder was studied by means of SEM to investigate the correlation between non-metallic phases on the powder surface and the microcracking susceptibility during LPBF. Characterization of microcracks, including morphology of the microcrack surfaces on fractured LPBF fabricated specimens, was performed to investigate the cracking mechanism during LPBF. Microstructural alterations as a consequence of HIP were examined by means of SEM/EDS analysis on fracture surfaces as well as metallographic cross sections. Furthermore, EBSD was used to study the grain structure in as-build and as-HIP conditions.

5.3 Surface sensitive analysis techniques

The surface sensitive analysis methods X-ray photoelectron spectroscopy (XPS) and Auger electron spectroscopy (AES) are valuable tools for surface analysis of powder and solid samples and have been used extensively throughout this study.

5.3.1 X-ray photoelectron spectroscopy

X-ray photoelectron spectroscopy is a technique for investigating elements at solid surfaces, their concentration and chemical state. The technique uses a high-resolution electron spectrometer to measure the kinetic energy and the intensity of the photoelectrons emitted from the sample when irradiated with X-rays. The binding energy of the emitted photoelectrons, which is characteristic of a particular electron shell of a specific chemical element in the interaction volume of the analyzed sample, can then be determined according to the theory of the photoelectric effect. The XPS spectrum is represented by peaks corresponding to the intensity of photoelectrons at each specific binding energy. Moreover, chemical bonding effects give rise to a detectable shift in the peak position, corresponding to the chemical state of the elements [120].

Survey spectra are usually recorded for identification of elements present on the surface. Narrow scan energy regions corresponding to the elements of interest are then selected for detailed analysis, followed by peak identification and curve fitting using an evaluation software like PHI Multipak to obtain the chemical composition of the surface and the chemical state of the elements.

The analyzed photoelectrons originate from the top 1-10 nm of the analyzed surface. Hence, XPS is one of the most accurate techniques for measuring the composition and thickness of surface compounds with a thickness of <10 nm [121]. The detection limit usually approximates 0.1 to 1 at.% [120], [121]. XPS spot analysis is typically limited to a lateral resolution of around 10 μm [121].

Surface chemical analysis of virgin and re-used Alloy 718 powder for EBM was performed by means of a PHI 5500 XPS instrument from Physical Electronics (Chanhassen, Minnesota, USA) to depict differences in chemical state and surface composition of powder samples exposed to varying numbers of re-use cycles. Surface compound thickness and changes in chemical composition with depth from the as-received surface down to an etch depth of up to 500 nm were obtained by altering XPS analysis and argon ion etching. The relative fractions of the oxide forming elements in cation state along the depth from the as-received surface were determined from peak curve fitting of the XPS high resolution spectra. The photoelectrons originate from an area of around 0.8 mm in diameter (~100 particles), which means that the signal represents the overall chemistry of the analyzed powder surface.

In the case of IN-738LC, a PHI VersaProbe 3 XPS analyzer from Physical Electronics (Chanhassen, Minnesota, USA) was employed. The powder surface was analyzed to determine the segregation behavior of trace and alloying elements during powder fabrication as well as to detect phases on the powder surface that may influence the cracking susceptibility of the alloy.

In addition, it has been shown that XPS (and AES, see Section 5.3.2) is a valuable tool to characterize microcracks caused by segregation of minor elements [122]. Thus, XPS was used for determining the chemical composition and chemical state of the elements present on the fracture surface of LPBF specimens fabricated from the powder grades in Table 7. To avoid contamination of the analyzed surfaces, the specimens were fractured under high-vacuum condition in a fracture device connected to the XPS analysis chamber via an ultra-high vacuum transfer system. The setup of the XPS system, including the XPS analysis chamber, fracture device and the transfer system, is shown in Figure 25. Fracture surfaces of samples after HIP treatment were also analyzed to investigate the formation of unwanted phases during HIP. As for the powder analysis, altering XPS analysis and argon ion etching of the fractured specimens indicate the thickness of the compounds present on the as-fractured surface.

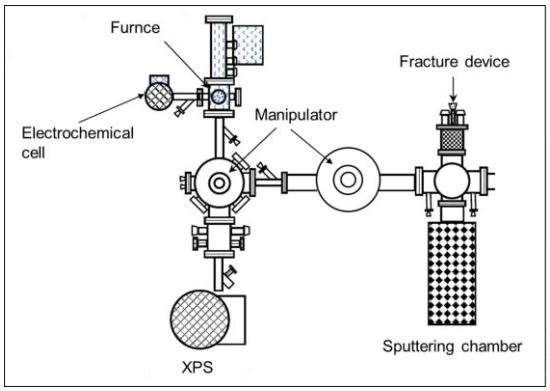

Figure 25. Setup of the VersaProbe 3 XPS analyzer with vacuum system and fracture device (redrawn from [123]*).*

5.3.2 Auger electron spectroscopy

Similar to XPS, Auger electron spectroscopy (AES) is a surface sensitive analysis technique based on the detection of Auger electrons emitted from the analyzed sample when irradiated with a high energy source.

In AES, the sample is irradiated by electrons from an electron gun with an acceleration voltage in the range of 1–20 keV. As in XPS, ionization of the atoms within the sample interaction volume results in the emission of energy. Transmission of the energy to electrons in the outer electron levels results in the emission of the Auger electrons. The characteristic energies of the Auger electrons are used for identifying the elements present in the sample [124].

The penetration depth of the electrons from the primary electron beam is typically 0.1–1 μm. However, as for the photoelectrons in XPS, the attenuation length of the Auger electrons is only a few monolayers from the analyzed surface and hence results in an information depth typically between 0.3 and 3 nm [124].

Compared to XPS, imaging capabilities by means of detecting secondary electrons in AES enable the possibility to perform laterally resolved surface chemical analysis. The nominal analytical lateral resolution is usually in the range of 3–30 nm. Argon ion etching capabilities of the system allow for composition depth profiling [124].

The SEM/EDS analysis of the Alloy 718 powder for EBM was complemented by AES, using a PHI700 instrument from Physical Electronics (Chanhassen, Michigan, USA) for detailed local characterization of oxide particulates on the surface of the virgin and re-used powder.

Moreover, the AES was employed for local chemical analysis of the microcrack surfaces of IN-738LC samples fractured in vacuum.

5.4 Bulk chemical analysis

The concentrations of alloying and trace elements in powder and PBF fabricated samples were measured by means of bulk chemical analysis.

The oxygen and nitrogen levels were measured by means of inert gas fusion (IGF), which is a common method for measuring the oxygen, nitrogen and hydrogen content in inorganic materials. In this process, a sample placed in a high purity graphite crucible is fused at a high temperature (roughly 3000°C) in a flow of inert gas. The oxygen present in the sample reacts with carbon from the graphite crucible to form carbon monoxide (CO) and carbon dioxide (CO_2), whereas nitrogen

and hydrogen are released as gas molecules (N_2 and H_2). The combustion gases are carried with the inert gas flow onto a detector, where it is measured [125]. Repeated measurements from the same powder samples have indicated that the accuracy is within ± 0.003 wt.%.

The carbon and sulphur content was measured by combustion analysis, in which the sample is combusted in a high flow of oxygen in an induction furnace. Carbon and sulfur present in the sample react with the oxygen and form CO_2 and SO_2, respectively, which is detected by infrared absorption [126]. Repeated measurements from the same powder samples have shown that the accuracy is within ± 0.0005 wt.%.

Most alloying elements, including B and Zr, as well as trace elements, such as P, Si and Mn were measured by induction coupled plasma optical emission spectroscopy (ICP-OES). In ICP-OES, the sample is dissolved in acid and is then brought as an aerosol into a plasma. As atoms and ions are excited in the plasma, they emit photons at wavelengths characteristic of the elements in the sample. A spectrometer calculates the proportions of the elements in the sample from the intensity of the emission of the characteristic wavelengths [127]. Repeated measurements from the same powder samples have indicated that the accuracy for measuring B, Zr, P, Si and Mn is within ± 0.0005 wt.%.

Oxidation of the re-used Alloy 718 powder for EBM was mapped by measuring the bulk oxygen level of powder samples collected in the sintered powder cake after build cycle completion. Similarly, the oxygen level of the powder before starting the build cycles was compared to the oxygen level of the corresponding solid samples to determine the correlation between the oxidation of the re-used powder and the amount of oxide inclusions present in the solid samples. Furthermore, the distribution of oxide and nitride inclusions in the EBM fabricated material, evaluated by means of image analysis, as described above, was complemented by oxygen and nitrogen level measurements of material extracted from different positions within the samples.

In the case of IN-738LC, ICP-OES was used to correlate the chemical composition (with special attention on the concentrations of B and Zr) of powder and LPBF fabricated samples to the cracking susceptibility of the investigated material variants. The concentrations of S, P, Si, Mn and O were also carefully controlled since they are known to have a possible negative effect on the cracking susceptibility of Ni-base superalloys.

5.5 Charpy impact testing

Charpy impact testing is a standardized method to measure the absorbed energy during the fracture of a sample that is hit by a swinging pendulum. The test indicates the toughness of the material and, thus, if it fails in a brittle or ductile manner, or somewhere in between [128]. The Charpy impact test is easy to prepare, conduct and evaluate and is therefore widely used in the industry. V-notched Charpy specimens (CVN) are most common, but other notch geometries as well as unnotched samples are also used [129]. The test is particularly useful to identify the ductile-to-brittle transition temperature in carbon steel [129]. However, as the test reflects the material toughness, factors such as yield strength, texture, grain structure, porosity, cracks, grain boundary embrittlement, non-metallic inclusions and other imperfections may be evaluated by means of the Charpy impact test [60], [128], [130], [131], [132].

The impact toughness depends on a number of factors, such as specimen size, notch geometry, test rate, test load and specimen support. Thus, the toughness values does not provide direct material behavior properties but can be used for comparative ranking of different materials if

conditions are held constant [133]. Evaluation of the fracture surface characteristics also provides information about the material ductility [128].

In this work, fractography of CVN specimens fabricated from progressively re-used powder was conducted to determine the effect of powder re-use on the presence of non-metallic inclusion of EBM fabricated Alloy 718 and to determine the formation mechanism.

Charpy impact testing of IN-738LC in as-built and as-HIP conditions was conducted to evaluate healing of microcracks by means of HIP.

6. Summary of results in appended papers

Part 1: Powder re-use and its effect on defect formation in EBM fabricated Alloy 718

Surface chemistry of virgin and re-used powder

In **paper I**, virgin and re-used powder was studied to determine the influence of multi-cycle EBM processing on the surface morphology and chemistry of Alloy 718 powder. A significant change in the powder surface chemistry, as a consequence of exposing the powder to the conditions in the EBM process chamber, is observed, as illustrated in Figure 26. The virgin powder surface, as in Figure 26 (a), has a smooth and clean appearance that is visually free from non-metallic phases or other contamination species. The powder collected after build cycle 14, on the other hand, has a different character in the sense that it contains a significant amount of oxide particulates that have formed on its surface, as evidenced in Figure 26 (b).

Based on the XPS and AES analyses of the two powder conditions presented in **paper I**, the transformation of the powder surface during multi-cycle EBM processing is illustrated in Figure 26 (c). The virgin powder surface is covered by a relatively thin and homogeneous Ni- and Al-rich oxide/hydroxide layer. The prolonged exposure at high temperature (around 1000°C) in the EBM build chamber enables selective oxidation of aluminum, which results in the formation of Al-rich oxide particulates. Significant growth occurs through aluminum diffusion from the powder interior in conjunction with the pick-up of oxygen from the process environment. In addition, aluminum and oxygen are re-distributed from the less stable products, such as Ni-oxide or hydroxide, in the initial oxide layer to form the more stable Al-rich oxide. This transformation already begins during the first build cycle and tends to increase with progressive powder re-use. The transformation results in a heterogeneous distribution of thermodynamically stable Al-rich oxide particulates, co-existing with a thin layer of transition metal oxide/hydroxide, which is formed in the regions between the oxide particles, most likely during subsequent exposure to air at lower temperatures, including powder handling.

The observed oxidation of the powder surface, as a result of powder re-use, is confirmed by a continuously increasing powder oxygen level, as shown in Figure 27. Furthermore, there is a clear correlation between the oxygen level in the solid samples and the powder from which they were built, which both increase with respect to progressive powder re-use.

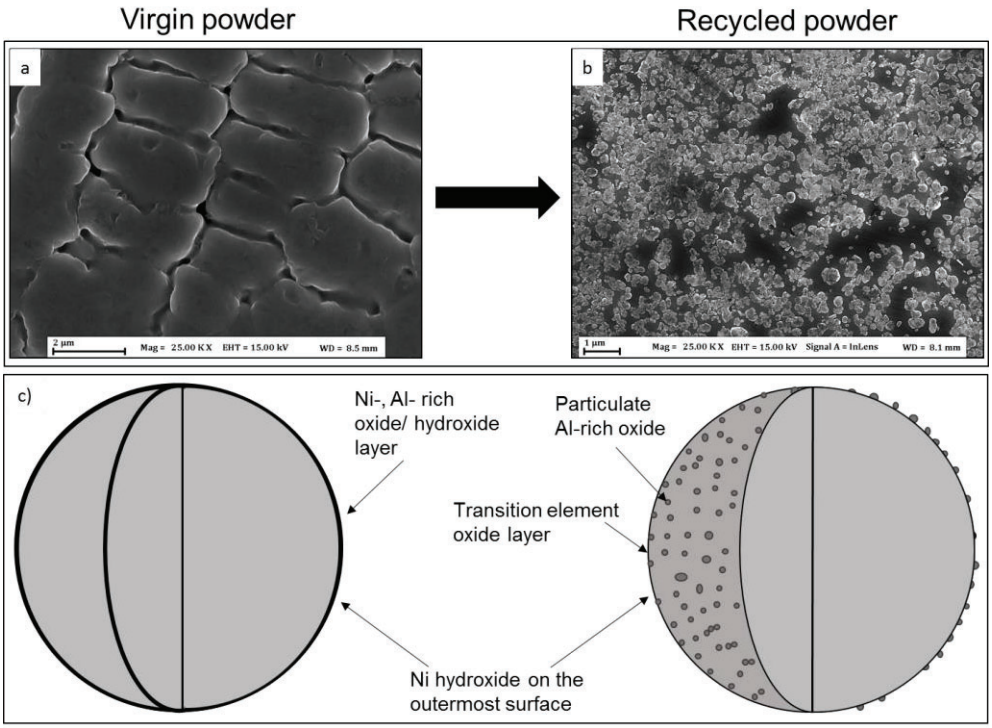

Figure 26. Transformation of the powder surface oxide layer during multi-cycle EBM processing; (a) virgin powder; (b) re-used powder collected after build cycle 14; (c) illustration of the powder before and after re-use [70].

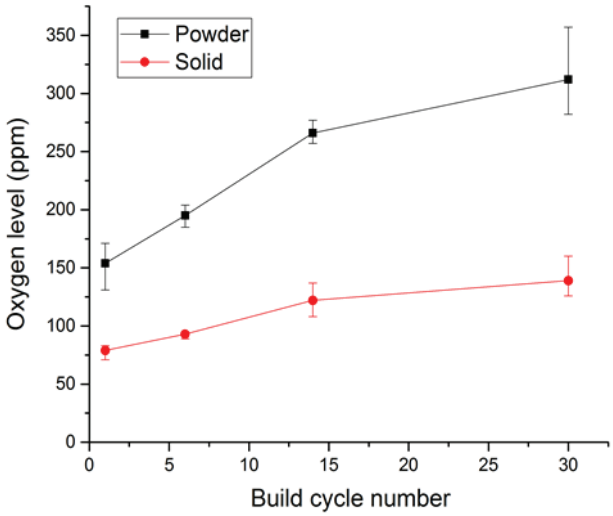

Figure 27. Oxygen level in powder (before build) and solid sample bulk material with respect to powder re-use [81].

Fracture behavior of EBM Alloy 718 fabricated from virgin and re-used powder

Fractography of samples built from virgin and 14 times re-used powder was performed in **paper II**. Oxide inclusions were found to be present on the fracture surfaces of samples built from virgin and re-used powder. As illustrated in Figure 28, the fracture surfaces of samples produced from re-used powder typically exhibit larger areas covered by oxide inclusions compared to those produced from virgin powder. In both cases, the largest oxide inclusions are found in the area between the hatch and the contour regions. The macroscopically rough surface topography in these

regions is a result of such defects that constitute weak interfaces along which the crack front propagates through an intergranular type of fracture. Large decohesion areas on the fracture surfaces indicate that fracture occurs along the weak interfaces between oxide and metal.

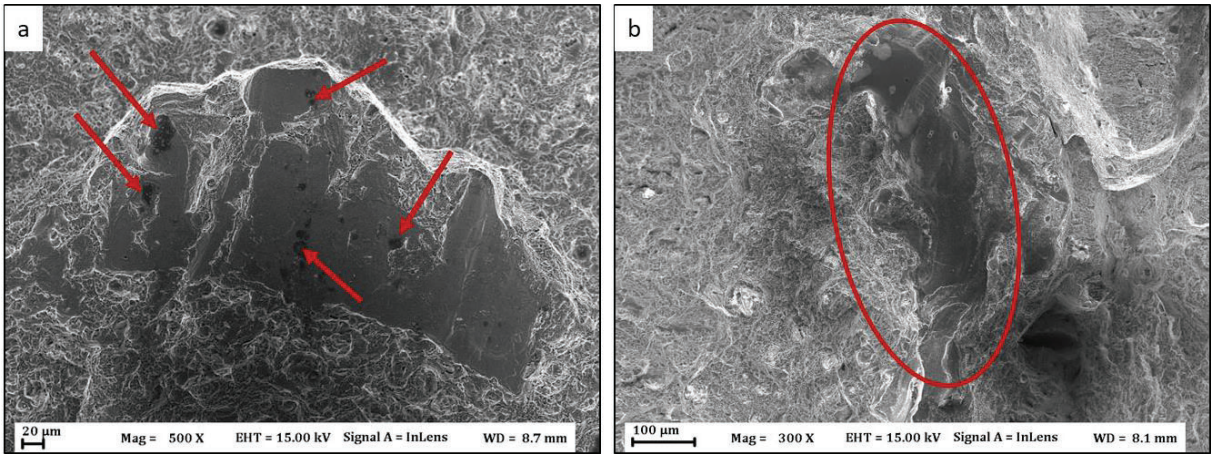

Figure 28. Oxide inclusions present on the fracture surface of samples fabricated from (a) virgin powder; (b) 14 times re-used powder [86].

Defect formation in EBM fabricated Alloy 718

As demonstrated in **paper III**, four oxide morphologies were observed in the samples produced from re-used powder, as shown in Figure 29. Similar for all cases is the presence of oxide particulates with the same size and shape as on the re-used metal powder, as illustrated in Figure 26 (b). The formation mechanism is largely connected to the melting process and depends on the ability of the electron beam to melt the oxide and the surrounding metal, which further depends on the volumetric energy density and the residence time of the electron beam as well as on the local wetting conditions. The latter is in this case reduced by the presence of oxide beneath the powder layer. In the case of a low degree of melting, the absence of a continuous melt pool results in oxide particulates dispersed inside LOFDs, as shown in Figure 29 (a, b). With an increasing degree of melting, the oxide particulates are present as clusters in the metal matrix, as in Figure 29 (c, d). This is followed by a range of partially to fully melted, continuous oxide flakes when the degree of melting is further increased, as shown in Figure 29 (e, f).

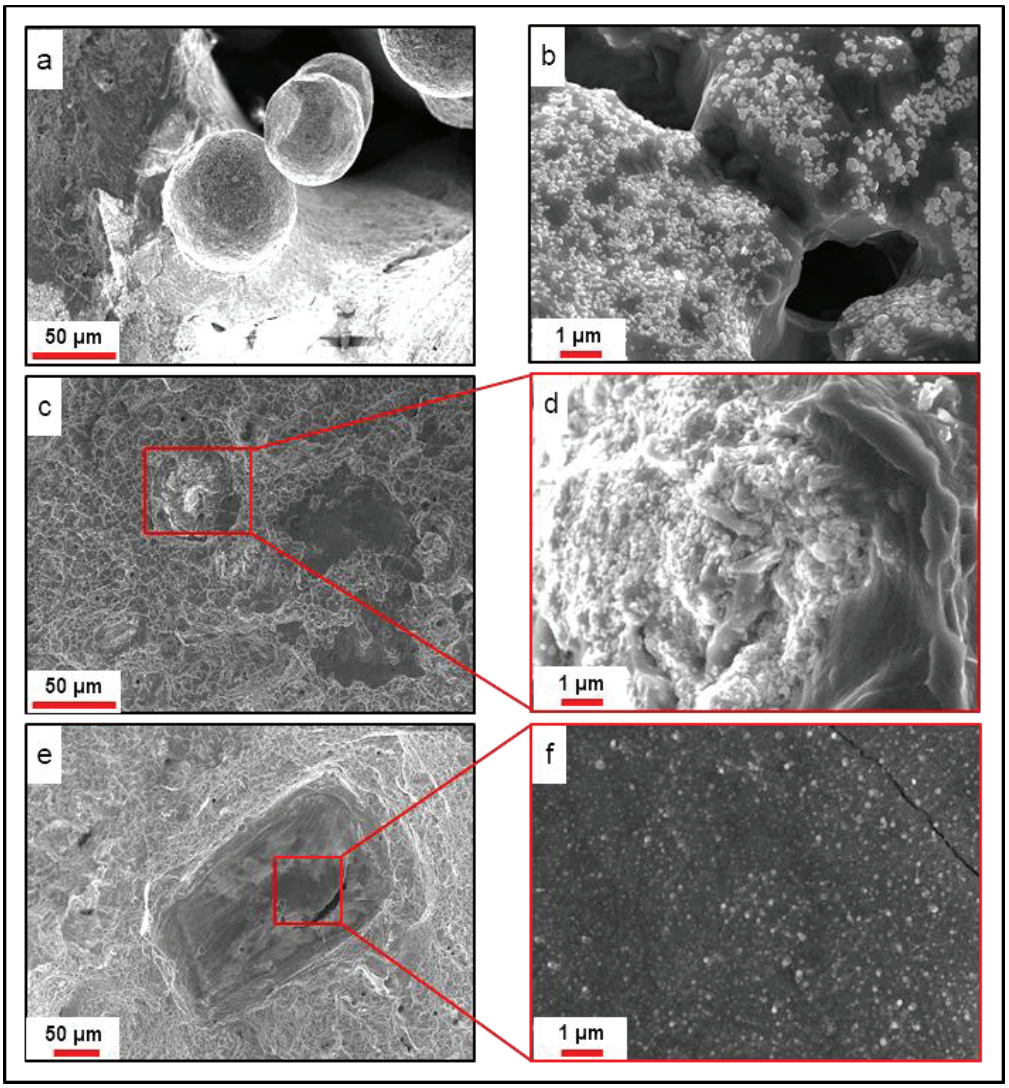

Figure 29. Different oxide defect morphologies in EBM processed Alloy 718 built from re-used powder ranging from (a, b) dispersed particulates, (c, d) clustered particulates and (e, f) fully melted Al-rich oxide [81].

Based on the above observations, it can be concluded that a major part of the observed oxide inclusions originates from the Al-rich oxide particulates on the surface of the re-used powder. As illustrated in Figure 30, due to its low solubility in the metal, this oxide persists through the melting process and is transferred to the component without being dissolved. Agglomeration of the oxide in the molten metal may result in large aggregates, which are sometimes entrapped as large inclusions in the metal during solidification. The TiN particles present in the powder also participate in the clustering and are commonly present at the metal-oxide interface.

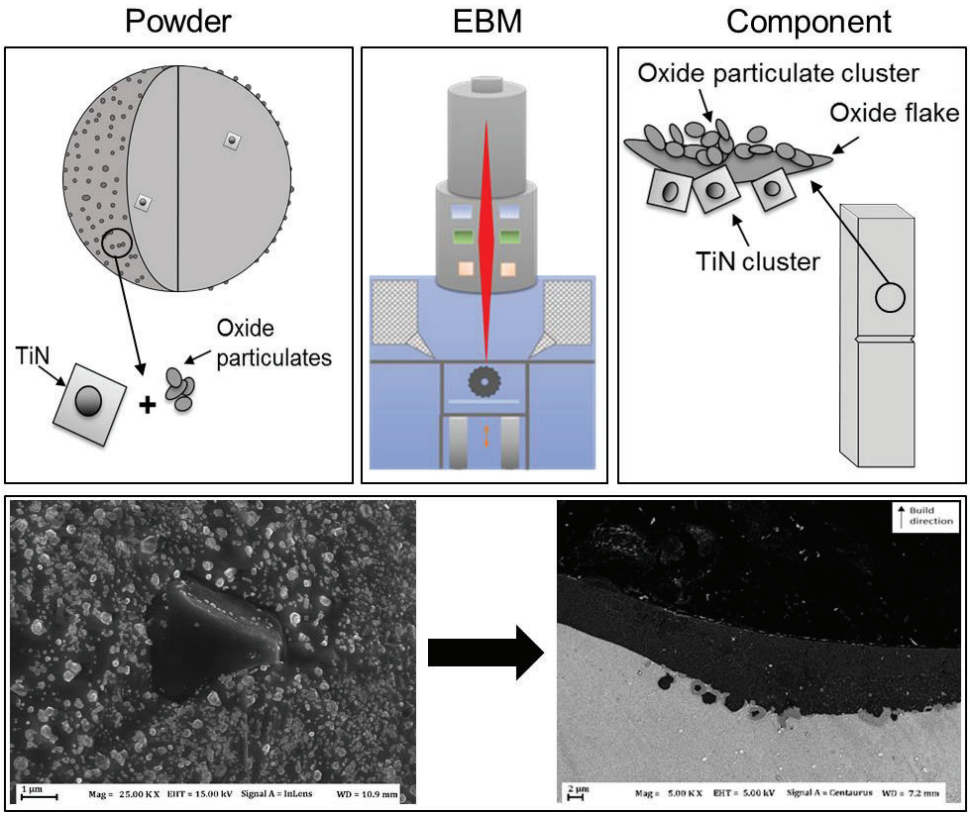

Figure 30. Transfer of non-metallic inclusions from the powder to the component during EBM processing [81].

The quantification of defects and their distribution in the samples produced from virgin and re-used powder was also studied in **paper III.** As indicated in Figure 31, a steady increase in the amount of defects as a consequence of progressive powder re-use is indicated from metallographic image analysis. The trend is especially clear in the contour region due to an increased amount of large oxide inclusions and LOFDs in samples produced from the re-used powder, as noted in Figure 31 (a). For improved visualization, the defect density after HIP treatment is presented separately in Fig. 31 (b). As can be seen here, HIP can be successfully used to reach a near fully dense material in case of the samples produced from virgin powder. However, for samples fabricated from re-used powder, a considerable amount of oxide inclusions remain after HIP treatment, especially in the contour region, as depicted in Figure 31 (b).

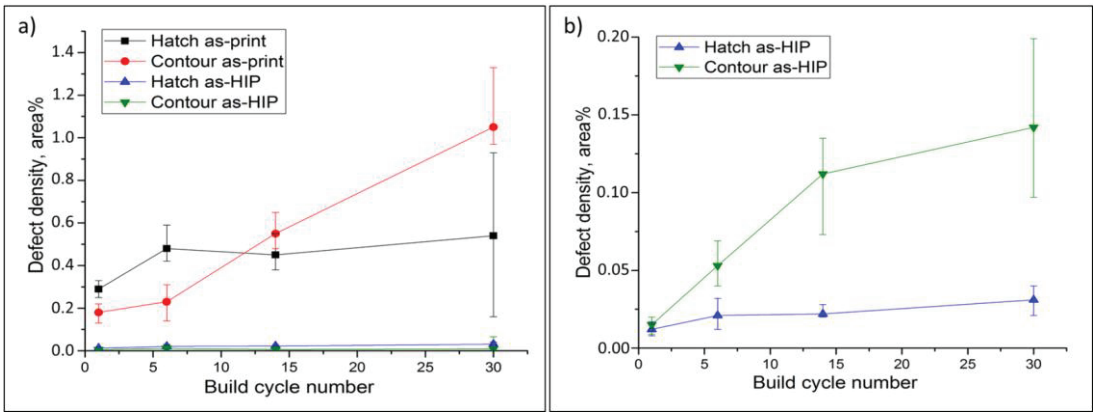

Figure 31. Defect density in samples built from progressively re-used powder; (a) as-printed and as-HIP condition; (b) as-HIP condition [81].

Accumulation of oxide in the contour region is confirmed by a higher oxygen level than the hatch region, as shown in Figure 32. Similarly, the top surface shows a higher oxygen level than the bulk material value. Both of these trends can be explained by studying the sample top surface, as presented in Figure 19 (a). In general, the top surface contains a large amount of oxide, which is particularly concentrated in the area of the interface between the hatch and the contour regions. This distribution of oxide in the solid samples is a function of transfer mechanisms parallel and transverse to the build direction, as illustrated in Figure 33.

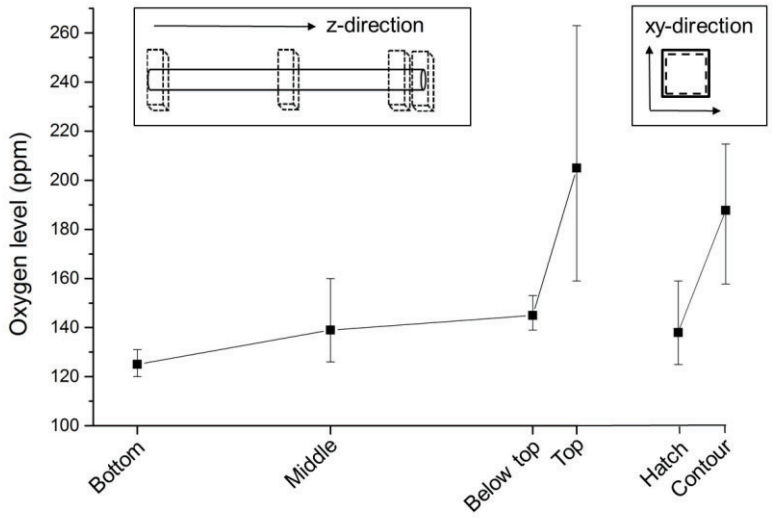

Figure 32. Distribution of oxygen concentration parallel (z-direction) as well as transverse (xy-direction) with respect to the build direction in samples built from re-used powder [81].

First, in the plane transverse to the build direction, oxide from the re-used powder may cluster in the molten metal as it moves with the electron beam, followed by accumulation at the electron beam turning points, i.e. at the interface between the hatch and the contour regions, as illustrated in Figure 33 (a).

Furthermore, clusters of non-metallic inclusions (oxide and nitride) in the liquid metal float toward the melt pool surface. During layer re-melting, these inclusions may be transported further upward, layer by layer along the build direction, as illustrated in Figure 33 (b). Eventually they may be entrapped as inclusions inside the metal matrix, as depicted in Figure 30. A certain amount, however, reaches the top surface, as shown in Figure 19 (a).

Transportation of oxide (and nitride) upward and toward the sample edges, as illustrated in Figure 33 (c), results in the bulk or core part of the EBM fabricated material having a lower oxygen level than the powder from which it was built, as shown in Figure 27. Dissociation of less stable oxides during powder melting may also contribute to this effect.

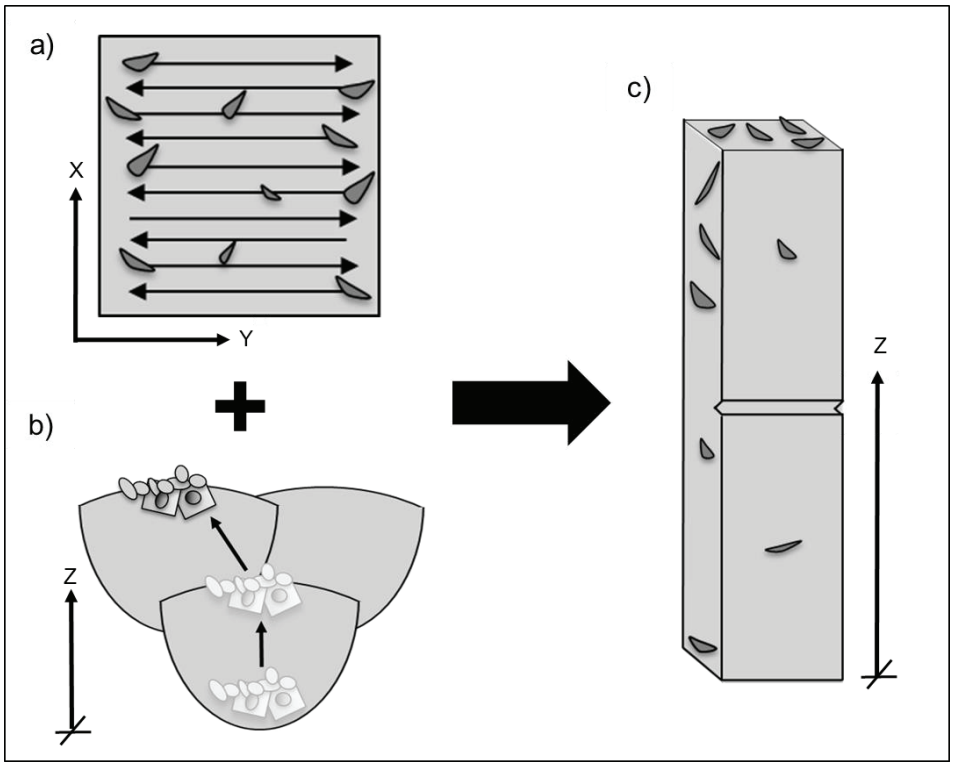

Figure 33. Inclusion transfer mechanisms in the directions (a) transverse and (b) parallel to the build direction resulting in accumulation of oxide at the contour region as well as on the sample top surface (c) [81].

Part 2: Cracking of LPBF fabricated IN-738LC

The effect of B and Zr on the microcrack susceptibility

The influence of B and Zr on the microcracking susceptibility of IN-738LC during LPBF processing was investigated in **paper IV.** Figure 34 presents the optical micrographs for the four studied alloy variants together with their levels of B and Zr measured by ICP-OES in the LPBF fabricated material. As the figure indicates, the variant with the lowest amount (<0.01 wt.%) of both elements is almost crack-free. Furthermore, separate additions of small amounts of Zr (up to 0.04 wt.%) have a negligible effect on the cracking susceptibility, while similar amounts of B have a stronger effect. The high crack density in the variant with 0.03 wt.% B and 0.06 wt.% Zr in the top right corner indicates that combined alloying significantly increases the cracking susceptibility.

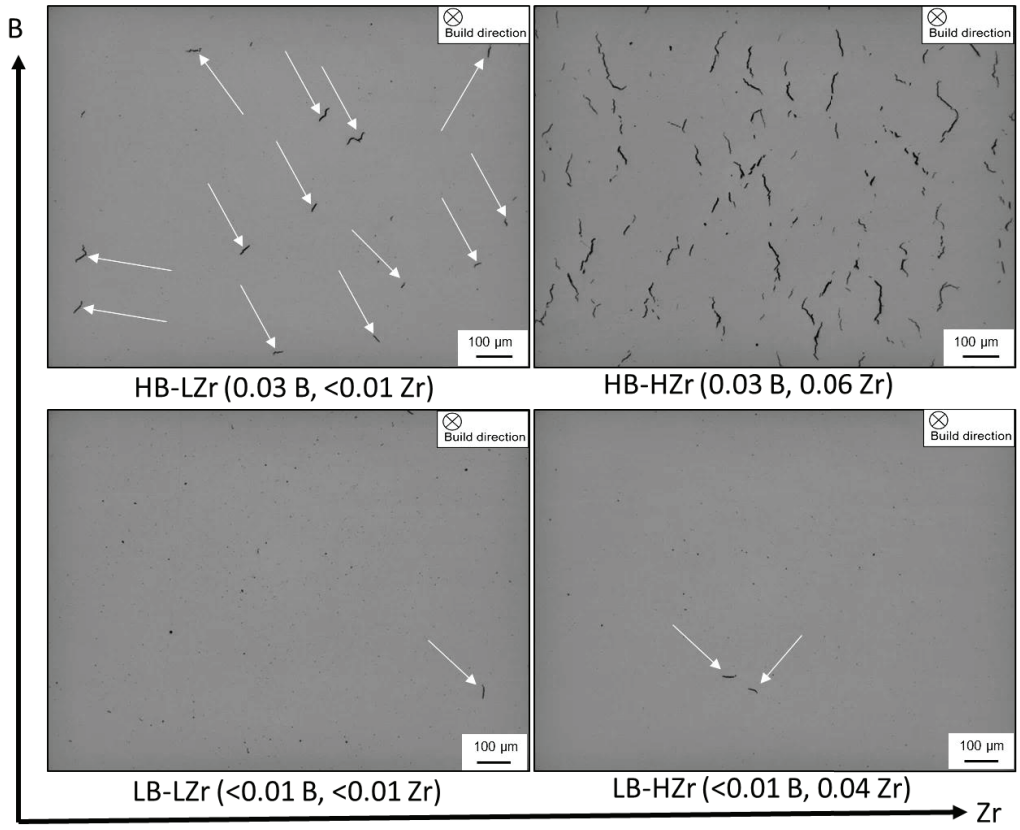

Figure 34. Schematic figure showing the influence of B and Zr on the microcracking susceptibility of IN-738LC during LPBF; the B and Zr levels are in wt.%; the cracks in LB-LZr, LB-HZr and HB-LZr are indicated with arrows [134].

The powder surface analysis using XPS reveals that B and Zr are enriched on the as-received surface of the HB-HZr powder. Hence, it is assumed that the elements, which are both strong oxide formers, segregate to the powder surface at a high temperature during powder fabrication and form oxide with the residual oxygen in the processing atmosphere.

Furthermore, enrichment in both elements is registered on the fracture surfaces of the heavily cracked HB-HZr LPBF specimen, fractured and analyzed under high vacuum, while being absent in the case of the other material variants. In addition, XPS confirms that a significant amount of both elements on powder and fracture surfaces are present as oxide, especially in the case of Zr.

The EBSD analysis of the HB-HZr variant demonstrates that the microcracks are located at high-angle grain boundaries. The SEM analysis reveals that the fracture surface of the HB-HZr variant exhibits a large portion of intergranular decohesion facets, exposing the interior of the microcracks, in contrast to a transgranular ductile feature in the other variants. The facets exhibit a dendritic morphology with limited presence of secondary dendrite arms, which is a well-known characteristic of solidification cracking.

Local chemical analysis by means of AES suggests that enrichment in B, Zr and O is connected to the decohesion facets, while being absent in the areas of transgranular, dimple fracture. Moreover, B- and Zr-containing oxide layers on the decohesion facets are detected by means of APT as well.

Based on these findings, it is suggested that the microcracking susceptibility of the studied alloy, when processed by LPBF, is increased by the accumulation of B_2O_3 and ZrO_2 on high-angle grain

boundaries, which leads to grain boundary embrittlement due to the poor cohesion strength between oxide and metal. The increased cracking susceptibility, together with high residual stresses induced by the LPBF process, promote grain boundary cracking.

Crack susceptibility during post-AM heat treatment

Macrocracking induced by hot isostatic pressing (HIP) was studied in paper **V**. It was found that significant macrocracking of the as-built LPBF fabricated IN-738LC occurs when applying a HIP strategy with uniform temperature and pressure profiles, as depicted in Figure 35. Heat treatment experiments conducted at atmospheric pressure demonstrate that the cracks form when heating the material in the temperature range 700°C–1200°C, which partly overlaps with the temperature interval in which rapid precipitation of the strengthening phase γ' occurs (~600°C-1000°C), as noted in Figure 36. Thus, it is suggested that the cracks form as a consequence of strain age cracking (SAC) due to the rapid formation of γ' together with high residual stresses induced by the LPBF process.

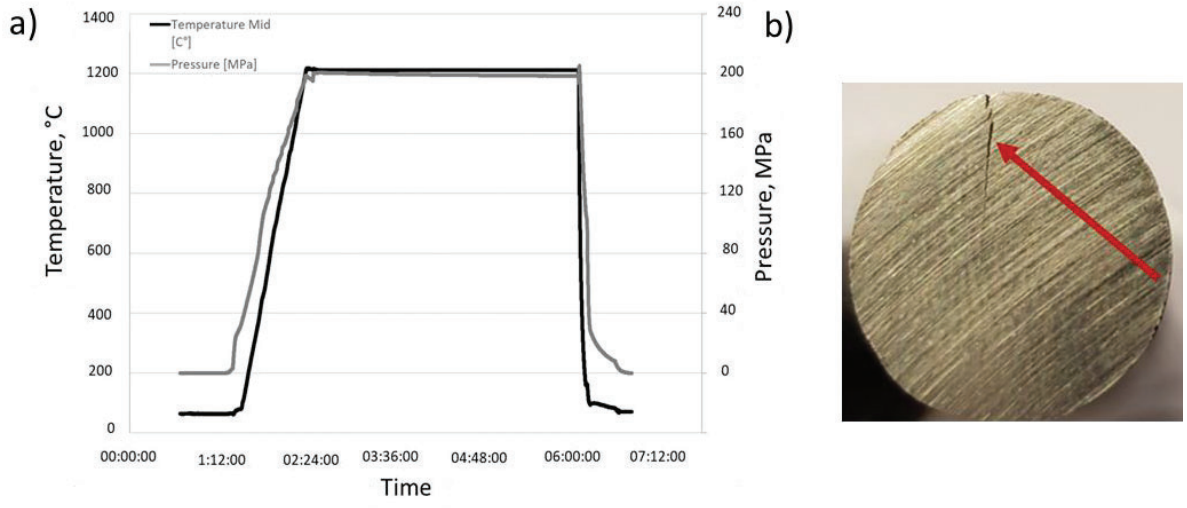

Figure 35. (a) HIP strategy with uniform heating and pressure profiles; (b) macroscopic cracks present after the HIP treatment in (a) [135].

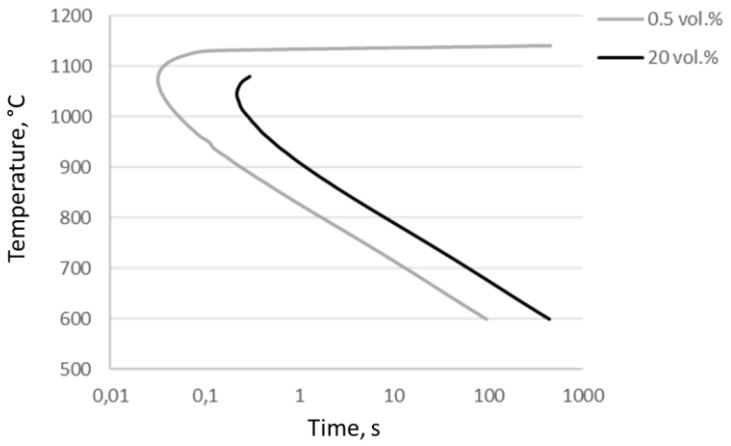

Figure 36. γ' TTT diagram with 0.5 and 20 vol.% transformation curves; plotted using data from JMatPro version 11.2; starting temperature 1200°C [135].

A modified HIP strategy, as presented in Figure 37, that efficiently suppresses macrocracking was developed based on the following modifications of the original HIP strategy:

- Slow heating in the temperature range 400–650°C was applied to relieve residual stresses before entering the critical temperature interval (T_{crit});
- The HIP pressure when entering the critical temperature region (P_{crit}) was increased to 200 MPa to suppress crack formation by means of inducing high compressive stresses at the sample surface;
- Rapid heating was applied in the critical temperature region to reduce the time available for formation of γ'.

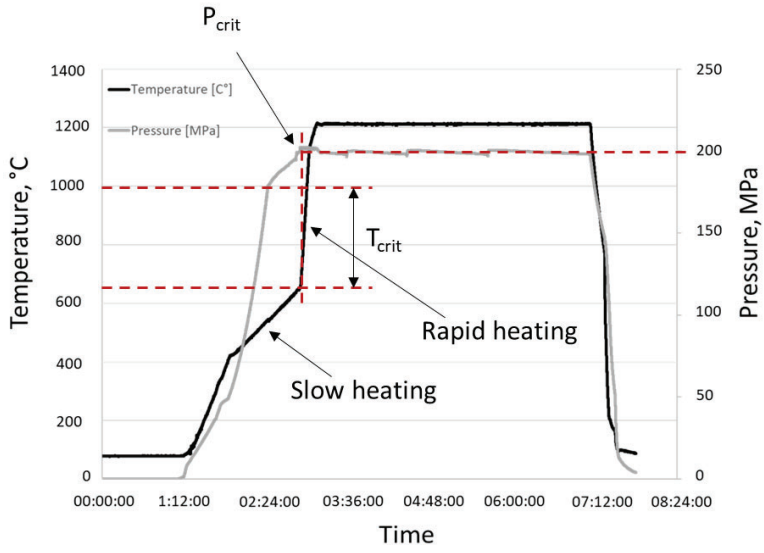

Figure 37. Developed HIP strategy [135].

An additional experiment with P_{crit} reduced to 100 MPa, which is equal to P_{crit} in the original HIP strategy (see Figure 35 (a)), resulted in the formation of small surface connected cracks, as shown in Figure 38 (b), which identifies the beneficial effect of applying a high pressure in the critical temperature region. Furthermore, compared to the original HIP strategy, the significantly reduced crack length after applying the strategy in Figure 38 (a) identifies the beneficial effect of the two other modifications in the developed HIP strategy as well.

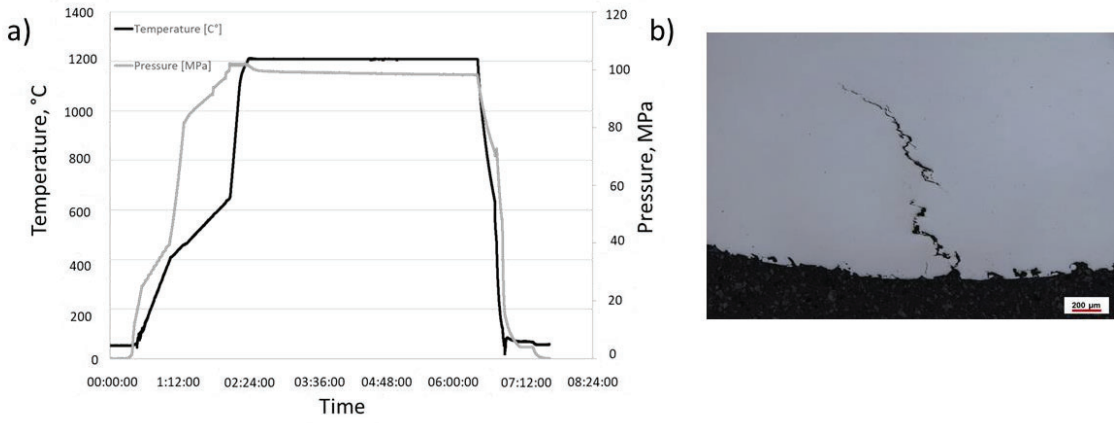

Figure 38. (a) Developed HIP strategy with 100 MPa maximum pressure; (b) crack present after the HIP treatment in (a) [135].

Healing of microcracks

In paper **V,** the developed strategy in Figure 37 was applied to determine if microcracks present in the as-built condition of the heavily cracked HB-HZr material grade can be healed. Microstructural alterations during the HIP treatment were studied as well**.** The close to crack-free material grade LB-LZr served as reference material.

Metallographic examination of polished cross sections of grade HB-HZr after HIP treatment at 1120°C and 1210°C are shown in Figures 39 (a) and (b), respectively. The healing of microcracks present in as-built condition (see Figure 34) seems to occur at both temperatures. However, significant formation of secondary phase particles (indicated by arrows) has occurred during the treatment at 1210°C, as evidenced in Figure 39 (b).

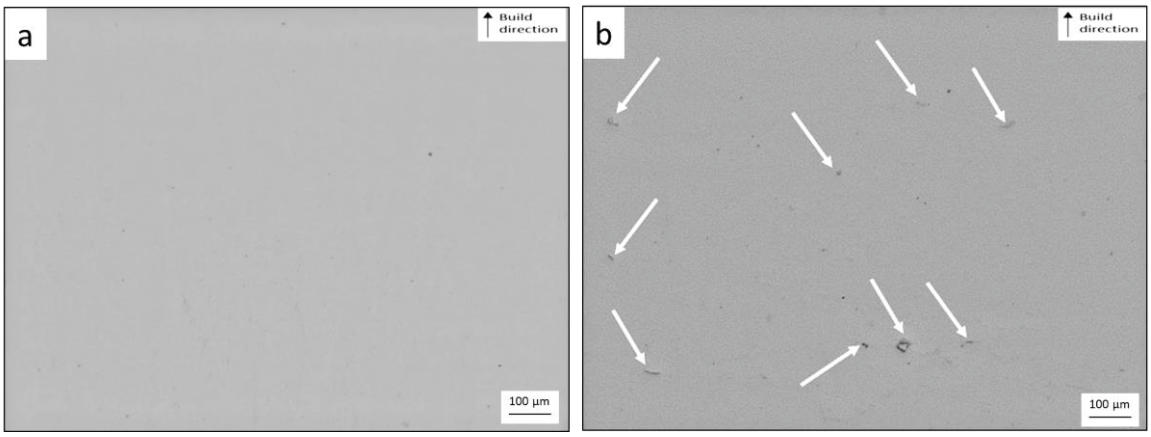

Figure 39. Material grade HB-HZr after HIP treatment at (a) 1120°C and (b) 1210°C [135].

Healing of microcracks at the HIP temperature of 1120°C is confirmed by a similar impact toughness of the two grades after HIP treatment at 1120°C, as demonstrated in Figure 40. Furthermore, impact testing for the two material grades after HIP treatment at 1210°C reveals that grade HB-HZr has a significantly lower impact toughness than the reference material LB-LZr.

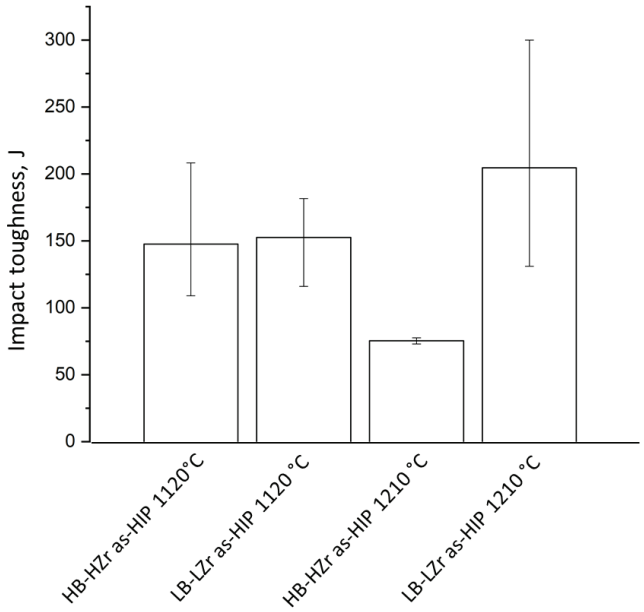

Figure 40. Charpy impact toughness of grade LB-LZr and HB-HZr HIP treated at 1120°C and 1210°C, respectively; the error bars indicate the actual measurement range [135].

Fractography of the HB-HZr test specimens after HIP treatment at 1210°C suggests that the reduced impact toughness is caused by the brittle secondary phase particles, as shown in Figure 41 (a), which are absent in the reference material, as in Figure 41 (b). Furthermore, Figure 41 (c) indicates that suppression of the brittle phase in grade HB-HZr is accomplished by lowering the HIP temperature to 1120°C.

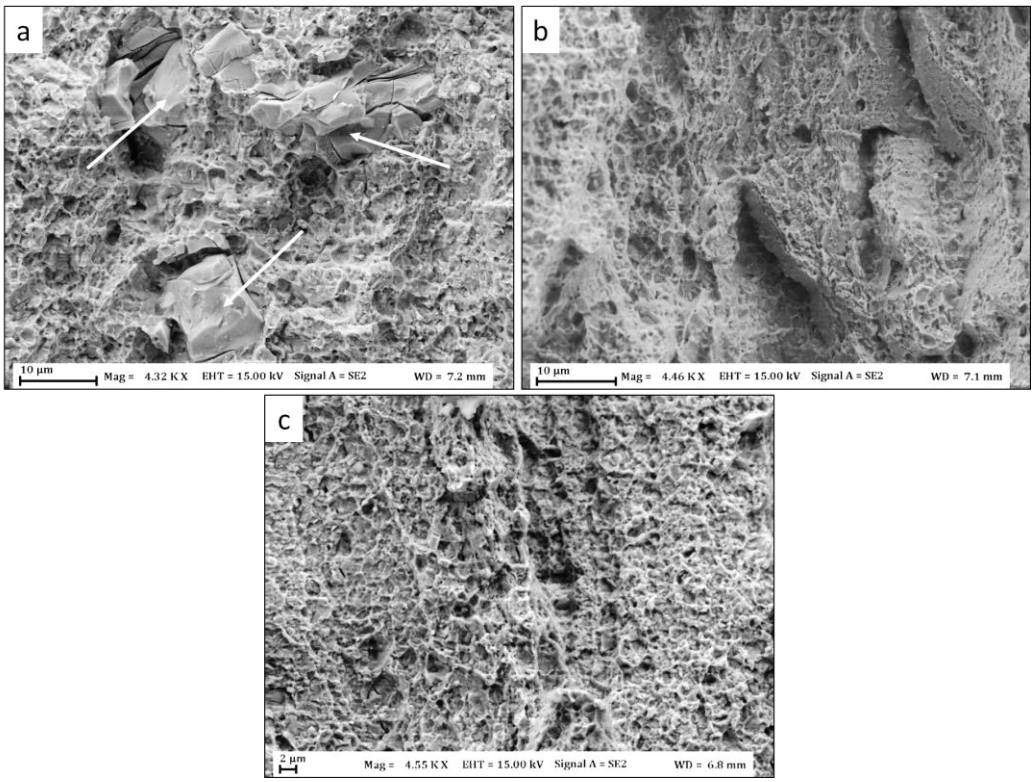

Figure 41. Fractographs of (a) HB-HZr after HIP at 1210°C; (b) LB-LZr after HIP at 1210°C; (c) HB-HZr after HIP at 1120°C [135].

EDS analysis of the brittle phase in HB-HZr after HIP at 1210°C reveals significant enrichment in Mo, W, Zr and B. In addition, the XPS analysis of the fracture surface shows the presence of metal boride and metal carbide. Hence, it is suggested that the brittle phase corresponds to complex Mo-W-rich metal boron carbide that forms due to the increased level of B in grade HB-HZr. Being absent after the HIP treatment at 1120°C suggests that formation of the brittle secondary phase particles is promoted by an increased particle coarsening rate or grain growth attributed to the higher diffusion rate at 1210°C. Nevertheless, the developed HIP strategy results in a material free from macrocracks, microcracks and brittle phases when applying the conditions 1120°C and 200 MPa.

7. Conclusions

The following conclusions can be drawn from this thesis study:

Part 1: Powder re-use and its effect on defect formation in EBM fabricated Alloy 718

RQ 1: What is the effect of EBM processing on re-use of Alloy 718 powder?

- The Alloy 718 powder undergoes significant oxidation while exposing the powder to the EBM process and the environment in the build chamber;
- Selective oxidation of Al under these conditions results in a transformation from the thin layer covering the virgin powder to a coarse, heterogeneous layer consisting of thermodynamically stable Al-rich oxide particulates together with a thin nickel oxide/hydroxide layer between the particulates;
- This transformation starts already during the first build cycle and progresses with an increasing number of re-use cycles. The increasing amount of oxide is confirmed by an increase in oxygen level with progressive re-use.

RQ 2: What is the effect of powder re-use on the amount and distribution of defects in EBM processed Alloy 718?

- Progressive powder re-use leads to an increased amount of oxide inclusions and lack of fusion defects (LOFDs) in the EBM fabricated material;
- Oxide inclusions occur as finely dispersed oxide inclusions inside LOFDs, oxide inclusion clusters and homogeneous oxide flakes;
- Transportation of oxide toward the sample edges during the melting process results in a higher amount of oxide inclusions and LOFDs in the contour region;
- The oxide inclusions are largely connected to the transfer of oxide particulates on the surface of the re-used powder to the EBM fabricated material;
- Due to the presence of oxide inside many LOFDs in samples built from re-used powder, they remain after hot isostatic pressing;
- The segregation of oxide in the contour region and on the samples' top surface results in a continuously lower oxygen level in the core parts of EBM fabricated material compared to the feedstock powder.

Part 2: Cracking of LPBF fabricated IN-738LC

RQ 3: What is the effect of B and Zr on the microcracking susceptibility of LPBF processed IN-738LC?

- Additions of B and Zr in the feedstock powder have a negative influence on the microcracking susceptibility of IN-738LC during the LPBF process. Separate additions of B (up to 0.03 wt.%) have a larger influence than Zr (up to 0.04 wt.%). Combined additions of both elements (0.03 wt.% B and 0.07 wt.% Zr) have the largest effect on crack density;
- Segregation of both elements occurs during both powder production and LPBF. In the latter case, a clear enrichment in both elements is present on the microcrack surfaces;
- A significant portion of B and Zr present on powder and fracture surfaces is connected to oxide;

- The microcrack surfaces exhibit a dendritic morphology with limited presence of secondary dendrite arms, which indicates a solidification cracking type of mechanism.

RQ 4: What is the cause of macrocracking during HIP treatment of LPBF processed IN-738LC, and how can it be mitigated?

- Macrocracking in HIP occurs during rapid heating of the as-built material from room temperature through the temperature interval 700–1200°C;
- Macrocracking can be mitigated by modifying the temperature-pressure profiles in the heating stage: 1) Application of a low heating rate in the range 400–650°C, 2) Application of a fast heating rate through the temperature interval connected to rapid formation of γ', and 3) Application of a high pressure (200 MPa) before entering the temperature interval connected to rapid formation of γ'.

RQ 5: What is the effect of HIP treatment on microcrack healing of LPBF processed IN-738LC?

- HIP treatment of the heavily cracked B- and Zr-containing grade at 1210°C results in extensive formation of a brittle phase, which is likely connected to Mo-W-rich metal boron carbide at the grain boundaries, with a dramatic loss in impact toughness as a consequence;
- Suppression of the brittle phase is accomplished by lowering the HIP temperature to 1120°C;
- Metallography and Charpy impact testing indicate that microcracks in the heavily cracked B- and Zr-containing grade can be extensively healed at the HIP temperature 1120°C by applying a pressure of 2000 bars for 4 hours.

8. Future work

The below recommendations are suggested as future work.

Part 1: Powder re-use and its effect on defect formation in EBM fabricated Alloy 718

A more thorough analysis of the surface chemical composition as well as the microstructure of the as-received and re-used powder conditions would provide a deeper understanding of the changes that occur during powder re-use. Similarly, in-depth analysis of oxide inclusions in the fabricated samples would provide further understanding regarding their origin and formation mechanisms.

Controlled laboratory experiments complemented by thermodynamic and kinetic simulations would be helpful to simulate powder oxidation at different conditions, such as various temperatures and oxygen levels, in order to assess the possibility of minimizing powder degradation during EBM processing.

Non-metallic inclusions have a negative influence on the mechanical properties of Ni- and Ni-Fe-base superalloys, and hence, the relevance of the findings in this work should be confirmed through mechanical testing, including fatigue testing.

Part 2: Cracking of LPBF fabricated IN-738LC

The segregation behavior of B and Zr in IN-738LC during LPBF should be further studied by means of high resolution analysis techniques – including atom probe tomography, transmission electron microscopy and nano secondary ion mass spectrometry – to fully determine the microcracking mechanism.

The individual influence of applying different temperature and pressure profiles in the suppression of macrocracks during hot isostatic pressing (HIP) should be further evaluated.

The mechanism behind macrocracking during HIP should be confirmed through detailed microstructural characterization. The formation of unwanted phases during HIP treatment should also be thoroughly investigated.

Microcrack healing by means of HIP should be evaluated through extensive mechanical testing, including fatigue testing.

9. Acknowledgements

First, I would like to thank my supervisor Prof. Eduard Hryha and my co-supervisor Prof. Lars Nyborg for giving me the opportunity to work with this exciting topic. I would also like to thank them both for their guidance, input and help throughout this work.

Recognition is owed to the Centre for Additive Manufacturing – Metal (CAM^2), supported by Vinnova, for enabling the framework within which this work has been performed. The author would like to acknowledge SIP LIGHTer and AoA Production at Chalmers for financial support.

Mikael Henriksson is greatly acknowledged, especially for being a good friend but also for all the help provided with XPS and AES analyses, on which we have spent many days together. Furthermore, I would like to thank my master's thesis students Emil Hallberg and Cosmina Luchian for their work in the lab.

Special appreciation is expressed to Jonas Olsson at Production Technology Centre, Trollhättan, Sweden for his help with EBM processing and powder sampling. Höganäs AB is greatly acknowledged for providing the experimental powder grades within the LPBF study as well as for Charpy impact testing and bulk chemical analysis. The same goes to Johannes Gårdstam at Quintus technologies for helpful discussions and for conducting the HIP treatments. Thanks to Niklas Israelsson and Simon Eichler at Arcam AB for input about the EBM project results.

I also would like to acknowledge the research engineers Dr. Ruslan Shvab, Dr. Eric Tam, Dr. Yiming Yao, Dr. Yu Cao, Lic. Eng. Lars Hammar, Håkan Millqvist and Roger Sagdahl for their help regarding all practical work.

Thanks to all my colleagues at the Department of Industrial and Materials Science for making this time enjoyable. Special thanks to my roommates Kristina Karlsson and Marcus Johansen and to all the members of the AM/PM group for the discussions, ideas, and memorable stories created during our conferences.

I would also like to thank my family and friends for reminding me of the world outside the office.

10. References

[1] J. C. Najmon, S. Raeisi, and A. Tovar, "Review of additive manufacturing technologies and applications in the aerospace industry,"*Additive Manufacturing for the Aerospace Industry*, 2019, DOI: https://doi.org/10.1016/B978-0-12-814062-8.00002-9.

[2] A. Ramakrishnan and G. P. Dinda, "Direct laser metal deposition of Inconel 738", *Mater. Sci. Eng. A*, vol. 740–741, no. May 2018, pp. 1–13, 2019.

[3] J. E. Matz and T. W. Eagar, "Carbide formation in alloy 718 during electron-beam solid freeform fabrication", *Metall. Mater. Trans. A*, vol. 33, no. 8, pp. 2559–2567, 2002.

[4] C. T. Sims, N. S. Stoloff, and W. C. Hagel, Superalloys 2, 2nd ed. Wiley, 1987.

[5] ASM International, Weld integrity and performance, 1997, ISBN 0-87170-600-8.

[6] M. Cloots, P. J. Uggowitzer, and K. Wegener, "Investigations on the microstructure and crack formation of IN738LC samples processed by selective laser melting using Gaussian and doughnut profiles", *Mater. Des.*, vol. 89, pp. 770–784, 2016.

[7] E. Chauvet *et al.*, "Hot cracking mechanism affecting a non-weldable Ni-based superalloy produced by Selective Electron Beam Melting," *Acta Mater.*, vol. 142, no. 17, pp. 82–94, 2017.

[8] L. Rickenbacher, T. Etter, S. Hövel, and K. Wegener, "High temperature material properties of IN738LC processed by selective laser melting (SLM) technology", *Rapid Prototyp. J.*, vol. 19, no. 4, pp. 282–290, 2013.

[9] L. N. Carter, C. Martin, P. J. Withers, and M. M. Attallah, "The influence of the laser scan strategy on grain structure and cracking behaviour in SLM powder-bed fabricated nickel superalloy", *J. Alloys Compd.*, vol. 615, pp. 338–347, 2014.

[10] D. Deng, *Additively Manufactured Inconel 718: Microstructures and Mechanical Properties*, no. 1798, Linköpings universitet, 2018.

[11] R. Sprague, "GAS TURBINE", *Advanced Materials and Processes*, May 2004, pp. 29–33, 2004.

[12] AMS F Corrosion Heat Resistant Alloys Committee, AMS 5662, SAE International, 2016.

[13] A. Thakur, "Microstructural Responses of a Nickel- Base Cast in-738 Superalloy To a Variety of Pre-Weld Heat-Treatments", Univ. Manitoba Microstruct., 1997.

[14] B. George and J. J. Galka, "Alloy IN-738 Technical Data," Int. nickel company, *INC.*, 1969.

[15] O. A. Ojo, N. L. Richards, and M. C. Chaturvedi, "On incipient melting during high temperature heat treatment of cast Inconel 738 superalloy", *Journal of Materials Science*, vol. 39, pp. 7401–7404, 2004.

[16] K. Kunze, T. Etter, J. Grässlin, and V. Shklover, "Texture, anisotropy in microstructure and mechanical properties of IN738LC alloy processed by selective laser melting (SLM)", *Mater. Sci. Eng. A*, vol. 620, pp. 213–222, 2014.

[17] M. Durand-Charre, *The microstructure of superalloys*, Gordon and Breach Science Publishers, Amsterdam, 1998.

[18] C. Hays, "Effects of {VIM+EBCHR} refining for IN-738 alloy", *J. Mater. Eng. Perform.*, vol. 16, no. 6, pp. 730–735, 2007.

[19] J. N. DuPont, J. C. Lippold, and S. D. Kiser, *Welding metallurgy and weldability of nickel-base alloys*, 1st ed. 2009.

[20] J. Andersson, "Weldability of precipitation hardening superalloys - influence of microstructure", Chalmers University of Technology, 2011.

[21] A. T. Egbewande, H. R. Zhang, R. K. Sidhu, and O. A. Ojo, "Improvement in laser weldability of INCONEL 738 superalloy through microstructural modification", *Metall. Mater. Trans. A Phys. Metall. Mater. Sci.*, vol. 40, no. 11, pp. 2694–2704, 2009.

[22] B. Du *et al.*, "M5B3 Boride at the Grain Boundary of a Nickel-based Superalloy," *J. Mater. Sci. Technol.*, vol. 32, no. 3, pp. 265–270, 2016.

[23] I. Gibson, D. Rosen, and B. Stucker, *Additive Manufacturing Technologies*, 2nd ed. 2015.

[24] A. Leicht, "Aspects of building geometry and powder characteristics in powder bed fusion", Chalmers University of Technology, Department of Industrial and Materials Science, 2018.

[25] A. T. Polonsky, M. P. Echlin, W. C. Lenthe, R. R. Dehoff, M. M. Kirka, and T. M. Pollock, "Defects and 3D structural inhomogeneity in electron beam additively manufactured Inconel 718", *Mater. Charact.*, vol. 143, 2018.

[26] M. Esperon-miguez, "The present and future of additive manufacturing in the aerospace sector : A review of important aspects", *J. Aerospace Engineering*, vol. 227, no. 11, pp. 2132-2147, 2015.

[27] H. E. Helmer, C. Körner, and R. F. Singer, "Additive manufacturing of nickel-based superalloy Inconel 718 by selective electron beam melting: Processing window and microstructure", *J. Mater. Res.*, vol. 29, no. 17, pp. 1987–1996, 2014.

[28] K. Wegener, F. Kuster, S. Weikert, L. Weiss, and J. Stirnimann, "Success Story Cutting", *Procedia CIRP*, vol. 46, pp. 512–524, 2016.

[29] S. Olovsjö, "Influence of microstructure in machining of nickel and nickel-iron based superalloys", Chalmers university of technology, 2011.

[30] Maher, "Alloy 718 Data Sheet Quick Facts Alloy 718 Data Sheet Industry Specifications Melting Practices Machinability", available at: https://www.maher.com/media/pdfs/718-datasheet.pdf, accessed 20200818.

[31] D. Zhu, X. Zhang, and H. Ding, "Tool wear characteristics in machining of nickel-based superalloys", *Int. J. Mach. Tools Manuf.*, vol. 64, pp. 60–77, 2013.

[32] V. Sames, William James, "Additive manufacturing of Inconel 718 using electron beam melting: Processing, post-processing, & mechanical properties", Texas A&M University, 2015.

[33] Svensk standard SS-EN ISO 17296-2:2016

[34] H. E. Helmer, "Additive Fertigung durch Selektives Elektronenstrahlschmelzen der Nickelbasis Superlegierung IN718 : Prozessfenster , Mikrostruktur und mechanische Eigenschaften", Der Technischen Fakultät der Friedrich-Alexander-Universität Erlangen-Nürnberg, 2016.

[35] J. A. Pakkanen, "Designing for Additive Manufacturing-Product and Process Driven Design for Metals and Polymers", Politecnico di Torino, 2018.

[36] European powder metallurgy association, *Introduction to additive manufacturing technology - a guide for designers and engineers*, 2nd ed. 2017.

[37] Höganäs AB, available at: https://www.hoganas.com/en/powder-technologies/additive-manufacturing/products/nickel-based/, accessed 20200818.

[38] M. I. Moulding, J. Kroeger, and R. Ap, "Raymor AP & C : Leading the way with plasma

atomised Ti spherical powders for MIM,"*Powder Injection Moulding International*, vol. 5, no. 4, pp. 55–57, 2011.

[39] K. Dietrich, P. Forêt, D. Bauer, and G. Witt, "How Porosity Is Affected By Different Residual Oxygen Concentrations In The Building Chamber During Laser Powder Bed Fusion (L-PBF)", *EuroPM2018*, 2018.

[40] C. Pauzon, E. Hryha, P. Forêt, and L. Nyborg, "Effect of argon and nitrogen atmospheres on the properties of stainless steel 316 L parts produced by laser-powder bed fusion", *Mater. Des.*, vol. 179, 2019.

[41] S. Biamino *et al.*, "Electron beam melting of Ti-48Al-2Cr-2Nb alloy: Microstructure and mechanical properties investigation", *Intermetallics*, vol. 19, no. 6, pp. 776–781, 2011.

[42] J. Risse, "Additive manufacturing of Nickel-base superalloy IN738LC by laser powder bed fusion", Rheinisch-Westfälischen Technischen Hochschule Aachen, 2019.

[43] P. Nandwana *et al.*, "Recyclability Study on Inconel 718 and Ti-6Al-4V Powders for Use in Electron Beam Melting", *Metall. Mater. Trans. B Process Metall. Mater. Process. Sci.*, vol. 47 B, no. 1, pp. 754–762, 2016.

[44] X. Wang, X. Gong, and K. Chou, "Review on powder-bed laser additive manufacturing of Inconel 718 parts", *Proc. Inst. Mech. Eng. Part B J. Eng. Manuf.*, vol. 231, no. 11, pp. 1890–1903, 2017.

[45] A. Leicht, R. Shvab, E. Hryha, and L. Nyborg, "Characterization of virgin and recycled 316L powder used in additive manufacturing", paper in proceedings, SPS16, Lund, 2016.

[46] M. Renderos, A. Torregaray, M. E. Gutierrez-Orrantia, A. Lamikiz, N. Saintier, and F. Girot, "Microstructure characterization of recycled IN718 powder and resulting laser clad material", *Mater. Charact.*, vol. 134, pp. 103–113, 2017.

[47] A. Strondl, O. Lyckfeldt, H. Brodin, and U. Ackelid, "Characterization and Control of Powder Properties for Additive Manufacturing", *Journal of the minerals, metals and materials society*, vol. 67, no. 3, pp. 549–554, 2015.

[48] V. Petrovic and R. Niñerola, "Powder recyclability in electron beam melting for aeronautical use", *Aircr. Eng. Aerosp. Technol.*, vol. 87, no. 2, pp. 147–155, 2015.

[49] S. B. Park, B. Road, and U. Kingdom, "Investigating the effects of multiple re-use of Ti6Al4V powder in additive manufacturing", white paper, *Renishaw*, 2016.

[50] R. Samant, A. Engineer, B. Lewis, and P. Technician, "Metal Powder Recycling and Reconditioning in Additive Manufacturing", EWI, 2017, availabe at: marketing.ewi.org/acton/attachment/12956/f-03b9/1/-/-/-/-/, accessed 20200818

[51] H. P. Tang, M. Qian, N. Liu, X. Z. Zhang, G. Y. Yang, and J. Wang, "Effect of Powder Reuse Times on Additive Manufacturing of Ti-6Al-4V by Selective Electron Beam Melting", *Journal of the minerals, metals and materials society*, vol. 67, no. 3, pp. 555–563, 2015.

[52] E. Hryha, E. Dudrova, and L. Nyborg, "On-line control of processing atmospheres for proper sintering of oxidation-sensitive PM steels", *J. Mater. Process. Technol.*, vol. 212, no. 4, pp. 977–987, 2012.

[53] S. Das, "Physical Aspects of Process Control in Selective Laser Sintering of Metals", *Adv. Eng. Mater.*, vol. 5, no. 10, pp. 701–711, 2003.

[54] C. Gierl-Mayer, R. de Oro Calderon, and H. Danninger, "The Role of Oxygen Transfer in Sintering of Low Alloy Steel Powder Compacts: A Review of the 'Internal Getter' Effect", *Journal of the minerals, metals and materials society*, vol. 68, no. 3, pp. 920–927, 2016.

[55] Q. Jia and D. Gu, "Selective laser melting additive manufacturing of Inconel 718 superalloy parts: Densification, microstructure and properties", *J. Alloys Compd.*, vol. 585, pp. 713–721, 2014.

[56] K. Sung Hwan, K. Chaewon, and O. S. Gokul, "Corrosion and Carburization Behaviour of Ni-Cr-Mo-Nb Superalloys in a High Temperature Supercritical-CO2 Environment", in *Proceedings of the 9th International Symposium on Superalloy 718 and derivatives*, 2018, pp. 179–192.

[57] R. Molins and E. Andrieu. "Analytical TEM study of the oxidation of nickel based superalloys. *Journal de Physique IV Colloque*, 1993, 03 (C9), pp.C9-469-C9-475.

[58] V. N. Shukla, R. Jayaganthan, and V. K. Tewari, "Oxidation and Hot Corrosion Behaviour of Ni-based Superalloy Inconel 718 in Na 2 So 4 -75 % V 2 O 5 Environment at Elevated Temperature", *International Journal of Surface Engineering & Materials Technology*, vol. 3, no. 1, pp. 20–24, 2013.

[59] E. Sadeghi *et al.*, "Isothermal Oxidation Behavior of EBM-Additive Manufactured Alloy 718", in *Proceedings of the 9th International Symposium on Superalloy 718 and derivatives*, 2018, pp. 219–239.

[60] X. Lou, P. L. Andresen, and R. B. Rebak, "Oxide inclusions in laser additive manufactured stainless steel and their effects on impact toughness and stress corrosion cracking behavior", *J. Nucl. Mater.*, vol. 499, pp. 182–190, 2018.

[61] E. Hryha, R. Shvab, H. Gruber, A. Leicht, and L. Nyborg, "Surface oxide state on metal powder and its changes during additive manufacturing: An overview", *Proc. Euro PM 2017 Int. Powder Metall. Congr. Exhib.*, 2018.

[62] I. Olefjord and L. Nyborg, "Surface Analysis of Gas Atomized Ferritic Steel Powder", *Powder Metall.*, vol. 28, no. 4, pp. 237–243, 1985.

[63] L. Nyborg and I. Olefjord, "Surface Analysis of REP-Atomized Martensitic Steel Powder" *Powder Metall. Int.*, vol. 20, no. 2, pp. 11–16, 1988.

[64] A. J. Cooper, N. I. Cooper, J. Dhers, and A. H. Sherry, "Effect of Oxygen Content Upon the Microstructural and Mechanical Properties of Type 316L Austenitic Stainless Steel Manufactured by Hot Isostatic Pressing", *Metall. Mater. Trans. A*, vol. 47, no. 9, pp. 4467–4475, 2016.

[65] M. Saunders, "Oxygen algebra - does yours add up?, available at https://www.linkedin.com/pulse/oxygen-algebra-does-yours-add-up-marc-saunders, accessed 20200818.

[66] M. Saunders, "Oxygen algebra - when it stops adding up", available at https://www.linkedin.com/pulse/oxygen-algebra-when-stops-adding-up-marc-saunders, accessed 20200818.

[67] L. C. Ardila *et al.*, "Effect of IN718 recycled powder reuse on properties of parts manufactured by means of Selective Laser Melting", *Phys. Procedia*, vol. 56, no. C, pp. 99–107, 2014.

[68] M. Galati and L. Iuliano, "A literature review of powder-based electron beam melting focusing on numerical simulations", *Addit. Manuf.*, vol. 19, pp. 1–20, 2018.

[69] Y. N. Zhang, X. Cao, P. Wanjara, and M. Medraj, "Oxide films in laser additive manufactured Inconel 718", *Acta Mater.*, vol. 61, no. 17, pp. 6562–6576, 2013.

[70] H. Gruber, M. Henriksson, E. Hryha, and L. Nyborg, "Effect of Powder Recycling in Electron Beam Melting on the Surface Chemistry of Alloy 718 Powder", *Metall. Mater. Trans. A Phys. Metall. Mater. Sci.*, vol. 50, no. 9, pp. 4410–4422, 2019.

[71] M. M. Attallah, R. Jennings, X. Wang, and L. N. Carter, "Additive manufacturing of Ni-based superalloys: The outstanding issues", *MRS Bull.*, vol. 41, no. 10, pp. 758–764, 2016.

[72] S. Tammas-Williams, P. J. Withers, I. Todd, and P. B. Prangnell, "Porosity regrowth during heat treatment of hot isostatically pressed additively manufactured titanium components", *Scr. Mater.*, vol. 122, pp. 72–76, 2016.

[73] S. Shrestha, T. Starr, and K. Chou, "A Study of Keyhole Porosity in Selective Laser Melting: Single-Track Scanning with Micro-CT Analysis", *J. Manuf. Sci. Eng. Trans. ASME*, vol. 141, no. 7, 2019.

[74] M. H. Manjili and M. Halali, "Removal of Non-metallic Inclusions from Nickel Base Superalloys by Electromagnetic Levitation Melting in a Slag", *Metall. Mater. Trans. B Process Metall. Mater. Process. Sci.*, vol. 49, no. 1, pp. 61–68, 2018.

[75] Y. Haruna, "Removal of inclusions from cast superalloy revert", University of British Columbia, 1994.

[76] A. Mitchell, "Recent Developments in Superalloy Melting Technology", *Key Eng. Mater.*, vol. 77–78, pp. 177–186, 1992.

[77] S. L. Cockcroft, T. Degawa, A. Mitchell, D. W. Tripp, and A.J. Schmalz, "Inclusion Precipitation in Superalloys", *Superalloys 1992*, pp. 577–586, 1992.

[78] A. Mitchell, A. J. Schmalz, C. Schvezov, and S. L. Cockcroft, "The Precipitation of Primary Carbides in Alloy 718", *Superalloys 718, 625, 706 Var. Deriv.*, pp. 65–78, 1994.

[79] A. R. Balachandramurthi, "*Fatigue Properties of Additively Manufactured Alloy 718"*, University West, 2018.

[80] A. Mitchell, "The Present Status of Melting Technology for Alloy 718", *Superalloys 718 Metall. Appl.*, pp. 1–15, 1989.

[81] H. Gruber, C. Luchian, E. Hryha, and L. Nyborg, "Effect of powder recycling on defect formation in electron beam melted Alloy 718", *Metall. Mater. Trans. A*, 2020.

[82] A. Mitchell, "Progress in Understanding Clean Metal Production for IN718", *Superalloys 718, 625 Var. Deriv.*, pp. 109–124, 1994.

[83] D. Krewerth, T. Lippmann, A. Weidner, and H. Biermann, "Influence of non-metallic inclusions on fatigue life in the very high cycle fatigue regime", *Int. J. Fatigue*, vol. 84, pp. 40–52, 2016.

[84] M. L. Harris, "A study on non-metallic inclusions in foundry steel process", Missouri University of Science and Technology, 2016.

[85] M.-A. Van Ende, "Formation and Morphology of non-Metallic Inclusions in Aluminium Killed Steels", Catholic University of Leuven, 2010.

[86] H. Gruber, P. Karimi, E. Hryha, and L. Nyborg, "Effect of Powder Recycling on the Fracture Behavior of Electron Beam Melted Alloy 718", *Powder Metall. Prog.*, vol. 18, no. 1, pp. 40–48, 2018.

[87] A. Balachandramurthi, J. Moverare, N. Dixit, and R. Pederson, "Influence of defects and as-built surface roughness on fatigue properties of additively manufactured Alloy 718", *Mater. Sci. Eng. A*, vol. 735, pp. 463–474, 2018.

[88] Y. Sun, R. Hebert, and M. Aindow, "Non-Metallic Inclusions in 17-4PH Stainless Steel Parts Produced by Selective Laser Melting", *Mater. Des.*, vol. 140, pp. 153–162, 2018.

[89] X. Xu, J. Ding, S. Ganguly, C. Diao, and S. Williams, "Oxide accumulation effects on wire

+ arc layer-by-layer additive manufacture process", *J. Mater. Process. Technol.*, vol. 252, no. July 2017, pp. 739–750, 2018.

[90] L. Thijs, J. Van Humbeeck, K. Kempen, E. Yasa, J. Kruth, and M. Rombouts, "Investigation on the inclusions in maraging steel produced by Selective Laser Melting", *Innov. Dev. Virtual Phys. Prototyp.*, pp. 297–304, 2011.

[91] P. N. Quested, D. M. Hayes, and K. C. Mills, "Factors affecting raft formation in electron beam buttons", *Mater. Sci. Eng. A*, vol. 173, no. 1–2, pp. 369–375, 1993.

[92] J. Campbell and M. Tiryakiog, "Bifilm Defects in Ni-Based Alloy Castings", *Met. Mater. Trans. B*, vol. 43 B, pp. 902–914, 2012.

[93] T. Mukherjee, V. Manvatkar, A. De, and T. DebRoy, "Mitigation of thermal distortion during additive manufacturing", *Scr. Mater.*, vol. 127, pp. 79–83, 2017.

[94] N. J. Harrison, I. Todd, and K. Mumtaz, "Reduction of micro-cracking in nickel superalloys processed by Selective Laser Melting: A fundamental alloy design approach", *Acta Mater.*, vol. 94, pp. 59–68, 2015.

[95] L. N. Carter, M. M. Attallah, and R. C. Reed, "Laser Powder Bed Fabrication of Nickel-Base Superalloys: Influence of Parameters; Characterisation, Quantification and Mitigation of Cracking", *Superalloys 2012*, no. October 2012, pp. 577–586, 2012.

[96] E. Chlebus, K. Gruber, B. Kunicka, J. Kurzac, and T. Kurzynowski, "Effect of heat treatment on the microstructure and mechanical properties of Inconel 718 processed by selective laser melting", *Mater. Sci. Eng. A*, vol. 639, pp. 647–655, 2015.

[97] Y. Chen *et al.*, "Dendritic microstructure and hot cracking of laser additive manufactured Inconel 718 under improved base cooling", *J. Alloys Compd.*, vol. 670, pp. 312–321, 2016.

[98] H. Ali, H. Ghadbeigi, and K. Mumtaz, "Processing Parameter Effects on Residual Stress and Mechanical Properties of Selective Laser Melted Ti6Al4V", *J. Mater. Eng. Perform.*, vol. 27, no. 8, pp. 4059–4068, 2018.

[99] F. Wang, X. H. Wu, and D. Clark, "On direct laser deposited Hastelloy X: dimension, surface finish, microstructure and mechanical properties", *Mater. Sci. Technol.*, vol. 27, no. 1, pp. 344–356, 2011.

[100] Y. Hagedorn, J. Risse, W. Meiners, N. Pirch, K. Wissenbach, and R. Poprawe, "Processing of nickel based superalloy MAR M-247 by means of High Temperature - Selective Laser Melting (HT - SLM)", *Proceedings of the 6th International Conference on Advanced Research and Rapid Prototyping*, 2013, pp. 291–295.

[101] X. Zhang, H. Chen, L. Xu, J. Xu, X. Ren, and X. Chen, "Cracking mechanism and susceptibility of laser melting deposited Inconel 738 superalloy", *Mater. Des.*, vol. 183, pp. 108105-1-14, 2019.

[102] A. Hariharan *et al.*, "Misorientation-dependent solute enrichment at interfaces and its contribution to defect formation mechanisms during laser additive manufacturing of superalloys," *Phys. Rev. Mater.*, vol. 3, no. 12, pp. 123602-1-17, 2019.

[103] N. Wang, S. Mokadem, M. Rappaz, and W. Kurz, "Solidification cracking of superalloy single- and bi-crystals", *Acta Mater.*, vol. 52, no. 11, pp. 3173–3182, 2004.

[104] O. A. Ojo, N. L. Richards, and M. C. Chaturvedi, "Contribution of constitutional liquation of gamma prime precipitate to weld HAZ cracking of cast Inconel 738 superalloy", *Scr. Mater.*, vol. 50, no. 5, pp. 641–646, 2004.

[105] S. C. Ernst, W. A. Baeslack III, and J. C. Lippold, "Weldability of High-Strength, Low-

Expansion Superalloys", *Weld J.*, no. October, pp. 418–430, 1989.

[106] D. Tomus *et al.*, "Controlling the microstructure of Hastelloy-X components manufactured by Selective Laser Melting", *Phys. Procedia*, vol. 41, pp. 823–827, 2013.

[107] R. Engeli, T. Etter, S. Hövel, and K. Wegener, "Processability of different IN738LC powder batches by selective laser melting", *J. Mater. Process. Technol.*, vol. 229, pp. 484–491, 2016.

[108] R. Castro and J. . de Cadenet, Welding metallurgy of stainless and heat-resisting steels. Cambridge university press, 1975.

[109] D. Tomus, P. A. Rometsch, M. Heilmaier, and X. Wu, "Effect of minor alloying elements on crack-formation characteristics of Hastelloy-X manufactured by selective laser melting", *Addit. Manuf.*, vol. 16, pp. 65–72, 2017.

[110] G. Marchese *et al.*, "Study of the microstructure and cracking mechanisms of hastelloy X produced by laser powder bed fusion", *Materials (Basel).*, vol. 11, no. 1, 2018.

[111] Z. Zhou, L. Huang, Y. Shang, Y. Li, L. Jiang, and Q. Lei, "Causes analysis on cracks in nickel-based single crystal superalloy fabricated by laser powder deposition additive manufacturing", *Mater. Des.*, vol. 160, pp. 1238–1249, 2018.

[112] F. Hanning, "Weld cracking in precipitation hardening Ni-based superalloys," Chalmers University of Technology, 2018.

[113] N. Perevoshchikova *et al.*, "Optimisation of selective laser melting parameters for the Ni-based superalloy IN-738 LC using Doehlert's design", *Rapid Prototyp. J.*, vol. 23, no. 5, pp. 881–892, 2017.

[114] X. Zhao, X. Lin, J. Chen, L. Xue, and W. Huang, "The effect of hot isostatic pressing on crack healing, microstructure, mechanical properties of Rene88DT superalloy prepared by laser solid forming", *Mater. Sci. Eng. A*, vol. 504, no. 1–2, pp. 129–134, 2009.

[115] J. H. Boswell, D. Clark, W. Li, and M. M. Attallah, "Cracking during thermal post-processing of laser powder bed fabricated CM247LC Ni-superalloy", *Mater. Des.*, vol. 174, p. 107793-1-12, 2019.

[116] G. Bi and A. Gasser, "Restoration of nickel-base turbine blade knife-edges with controlled laser aided additive manufacturing," *Phys. Procedia*, vol. 12, no. PART 1, pp. 402–409, 2011.

[117] C. Qiu, H. Chen, Q. Liu, S. Yue, and H. Wang, "On the solidification behaviour and cracking origin of a nickel-based superalloy during selective laser melting", *Materials Characterization,* vol. 148, 2018.

[118] H. Atkinson and S. Davies, "Fundamental aspects of hot isostatic pressing: an overview", *Metall. Mater. Trans. A*, vol. 31A, December, pp. 2981–3000, 2000.

[119] M. Lamberigts, E. Diderrich, and D. Coutsouradis, "Hip'ing various precision cast engine components in nickel-base superalloys," *Superalloys 1980*.

[120] R. Paynter, "XPS Theory," 2000.

[121] A. G. Shard, "Detection limits in XPS for more than 6000 binary systems using Al and Mg Kα X-rays", *Surf. Interface Anal.*, vol. 46, no. 3, pp. 175–185, 2014.

[122] A. . Ilyin and V. . Golovanov, "Auger spectroscopy study of the stress enhanced impurity segregation in a Cr-Mo-V steel", *J. Nucl. Mater.*, vol. 233–237, pp. 233–235, 1996.

[123] E. Hryha, E. Rutqvist, and L. Nyborg, "Stoichiometric vanadium oxides studied by XPS", *Surf. Interface Anal.*, vol. 44, no. 8, pp. 1022–1025, 2012.

[124] S. Hofmann, Auger- and X-ray photoelectron spectroscopy in materials science. 2013.

[125] A. Cooke and J. Slotwinski, "Properties of Metal Powders for Additive Manufacturing: A Review of the State of the Art of Metal Powder Property Testing", 2012.

[126] Eltra GmbH, "Eltra elemental analysers," 2020. available at: https://www.eltra.com/products/carbon-sulfur-determination/. accessed 20200512.

[127] Spectro analytical instruments GmbH, "Spectro analytical instruments," 2020. available at: https://www.spectro.com/icp-oes-principle. accessed 20200512.

[128] P. Moore and G. Booth, The Welding Engineers Guide to Fracture and Fatigue, Woodhead Publishing, edition 1, 2015.

[129] R. Smallman and A. H. Ngan, Modern Physical Metallurgy, 8th ed. 2014.

[130] A. J. Cooper, W. J. Brayshaw, and A. H. Sherry, "Ductile Fracture Behaviour of Hot Isostatically Pressed Inconel 690 Superalloy", *Metall. Mater. Trans. A Phys. Metall. Mater. Sci.*, vol. 49, no. 4, pp. 1079–1089, 2018.

[131] J. Hicks, Welded joint design, 3rd ed. 1999.

[132] S. . Banerji and C. . Briant, Encyclopedia of Physical Science and Technology, 3rd ed. 2003.

[133] M. C. Sobieraj and C. M. Rimnac, PEEK Biomaterials Handbook, 2nd ed. 2019.

[134] H. Gruber, K. Lindgren, Y. Cao, M. Rashidi, E. Hryha, and L. Nyborg, "The effect of Boron and Zirconium on the Microcracking Susceptibility of IN-738LC Derivatives in Laser Powder Bed Fusion", In manuscript, 2020.

[135] H. Gruber, J. Xu, E. Hallberg, H. Eduard, and N. Lars, "Hot Isostatic Pressing of IN-738LC produced by means of Laser Powder Bed Fusion", In manuscript, 2020.